Fluorinated and Fluorine-Free Coordination Polymers Based on Alkaline Earth Metals via Mechanochemistry

Dissertation

Zur Erlangung des akademischen Grades

Doctor rerum naturalium

(Dr. rer. nat.)

Im Fach Chemie

Eingereicht an der

Mathematisch-Naturwissenschaftlichen Fakultät

Humboldt-Universität zu Berlin

von

Abdal-Azim Al-Terkawi

Präsidentin der Humboldt-Universität zu Berlin

Prof. Dr.-Ing. Dr. Sabine Kunst

Dekan der Mathematisch-Naturwissenschaftlichen Fakultät

Prof. Dr. Elmar Kulke

Gutachter/innen: 1. Prof. Dr. Erhard Kemnitz

2. PD Dr. Gudrun Scholz

3. Prof. Dr. Wolfgang Tremel

Tag der mündlichen Prüfung: 18.06.2018

Abstract

A series of fluorinated coordination polymers (FCPs) were mechanochemically synthesized using alkaline earth metal hydroxides (M = Ca, Sr, Ba) that vary in their water content as inorganic sources. The perfluorinated benzene-dicarboxylic acids and their fluorine-free analogs were used as organic linkers. The obtained FCPs are compared to their synthesized fluorine-free counterparts (CPs) under the same conditions.

The presence of fluorine influences both thermal and structural properties of the resulting FCPs. The latter are also strongly affected by the difference in geometries and nature of organic linkers. Water introduced to grinding acts as a mediator for the milling process and as a reactant for stabilizing the resulting structures. The difference in cation size between Ca^{2+}- and Sr^{2+}-ions has a minor effect on their coordination with perfluorinated or fluorine-free benzene-dicarboxylate anions. Here, Ca- and Sr-compounds crystallize isomorphously (an exception was recorded for *ortho*-phthalate systems). In contrast, the relatively larger size of Ba^{2+}-cation strongly influences the coordination environment.

The obtained compounds by milling are hydrated and exhibit small surface areas that can increase after thermal post-treatment. The FCPs are stable up to 300 ˚C. On the other hand, the nonfluorinated CPs begin to decompose above 400 ˚C. The hydrated samples transform into new dehydrated phases upon thermal annealing. The hydrated-dehydrated phase transformation can be reversible.

Moreover, the effect of replacement of one carboxylic group by an amino group in an organic ligand was explored. In the CPs based on anthranilic acid, the variations in cation size between Ca^{2+}-, Sr^{2+}-, and Ba^{2+}-ions affect both coordination environment and dimensionality of the resulting CPs.

The physicochemical properties of the new materials were systematically investigated applying different analytical techniques such as elemental analysis, powder X-ray diffraction, thermal analysis, MAS NMR, Infrared-spectroscopy, SEM imaging, gas sorption, and dynamic vapor sorption measurements. The crystal structures of the new fluorinated and fluorine-free CPs were determined from the powder X-ray diffraction data and subsequently refined using the Rietveld method. The local coordination environments around metals were investigated by X-ray absorption spectroscopy.

Kurzfassung

Fluorhaltige-Koordinationspolymere (FCPs) wurden durch mechanochemische Reaktionen synthetisiert. Die Erdalkalimetallhydroxide (M = Ca, Sr, Ba), die in ihrem Wassergehalt variieren, wurden als anorganische Quellen verwendet. Die perfluorierten Benzol-Dicarboxylsäuren und ihre fluorfreien Analoga wurden als organische Linker verwendet. Die erhaltenen FCPs werden mit den fluorfreien Verbindungen (CPs) verglichen, die unter den gleichen Mahlbedingungen synthetisiert wurden.

Der Austausch von Wasserstoff- durch Fluoratome beeinflusst sowohl die thermischen als auch die strukturellen Eigenschaften der FCPs. Letztere werden auch von den Unterschieden der Geometrien und von der Natur der organischen Linker beeinflusst. Während des Mahlprozesses dient Wasser dabei hauptsächlich als Vermittlermedium und zur Stabilisierung der neuen Strukturen. Die Unterschiede in den Kationengrößen zwischen Ca^{2+}- und Sr^{2+}-Ionen wirken sich geringfügig auf ihre Koordination durch die Dicarboxylatanionen aus. Hier kristallisieren Ca- und Sr-Verbindungen zumeist isomorph. Im Gegensatz dazu beeinflusst der große Ionenradius der Ba^{2+}-Kationen die lokalen Koordinationsumgebungen.

Die durch Mahlen erhaltenen Verbindungen sind hydratisiert und weisen eine kleine spezifische Oberfläche auf, die nach der thermischen Behandlung zunehmen kann. Die FCPs sind bis zu 300 °C stabil, während die CPs sich erst oberhalb von 400 °C zersetzen. Die hydratisierten Proben wandeln sich beim Tempern in neue dehydratisierte Phasen um. Die Phasenumwandlung kann reversible ablaufen.

Zusätzlich wurde der Effekt des Austausches einer Carboxylgruppe durch eine Aminogruppe in einem organischen Liganden untersucht. In den CPs auf der Basis von Anthranilsäure beeinflussen die unterschiedlichen Kationengrößen der Ca^{2+}-, Sr^{2+}-, und Ba^{2+}-Ionen sowohl die Koordinationsumgebung als auch die Dimensionalität der CPs.

Die physikalisch-chemischen Eigenschaften der neuen Materialien wurden systematisch durch verschiedene analytische Techniken wie Elementaranalyse, Röntgenpulverbeugung, thermische Analyse, MAS-NMR- und Infrarot-Spektroskopie, REM-Bildgebung, Gassorption und dynamischer Dampfsorptionsmessung untersucht. Die Kristallstrukturen der neuen fluorierten und fluorfreien CPs wurden aus den Daten der Röntgenpulverbeugung bestimmt und anschließend mit der Rietveld Methode verfeinert. Die lokalen Koordinationsumgebungen der Metalle wurden mittels Röntgenabsorptionsspektroskopie untersucht.

Glossary of Abbreviations

Abbreviation	Meaning
CP	**C**oordination **P**olymer (Exception: In ^{13}C CP MAS NMR, CP is an abbreviation for Cross Polarization)
FCP	**F**luorinated **C**oordination **P**olymer
HBN	**H**ydrogen-**B**onding **N**etwork
AE	**A**lkaline **E**arth Metals
I^nO^m	Connectivity in CPs: **n** is the degree of **i**norganic connectivity between metal centers, and **m** is the degree of **o**rganic connectivity between metal centers. n + m = 0, 1, 2, or 3 (according to the I^nO^m terminology by Cheetham *et al.*).[1]
1D, 2D, or 3D	One, two, or three dimensions (for describing the structures of CPs).
C.N.	**C**oordination **N**umber
H_2BDC-F_4	Tetra**f**luoro**b**enzene-**d**i**c**arboxylic acid
H_2*p*BDC-F_4	Tetrafluoroterephthalic acid (Tetrafluorobenzene-*para*-dicarboxylic acid)
H_2*m*BDC-F_4	Tetrafluoroisophthalic acid (Tetrafluorobenzene-*meta*-dicarboxylic acid)
H_2*o*BDC-F_4	Tetrafluorophthalic acid (Tetrafluorobenzene-*ortho*-dicarboxylic acid)
H_2BDC	**B**enzene-**d**i**c**arboxylic acid
H_2*p*BDC	Terephthalic acid (Benzene-*para*-dicarboxylic acid)
H_2*m*BDC	Isophthalic acid (Benzene-*meta*-dicarboxylic acid)
H_2*o*BDC	Phthalic acid (Benzene-*ortho*-dicarboxylic acid)
ABAH-F_4	**A**mino-tetra**f**luoro**b**enzoic **a**cid
***p*ABAH-F_4**	*para*-amino-tetrafluorobenzoic acid
***o*ABAH-F_4**	Tetrafluoroanthranilic acid (*ortho*-amino-tetrafluorobenzoic acid)
ABAH	**A**mino-**b**enzoic **a**cid
***p*ABAH**	*para*-amino-benzoic acid
***m*ABAH**	*meta*-amino-benzoic acid
***o*ABAH**	Anthranilic acid (*ortho*-amino-benzoic acid)
LAG	**L**iquid-**A**ssisted **G**rinding
DTA-TG	**D**ifferential **T**hermal **A**nalysis-and-Simultaneous **T**hermo**g**ravimetric.
XAS	**X**-ray **A**bsorption **S**pectroscopy
EXAFS	**E**xtended **X**-Ray **A**bsorption **F**ine **S**tructure
ATR-IR	**A**ttenuated **T**otal **R**eflection-**I**nfrared **S**pectroscopy
FT-IR	**F**ourier-**t**ransform-**I**nfrared **S**pectroscopy
BET	**B**runauer–**E**mmett–**T**eller measurement.
MAS NMR	**M**agic **A**ngle **S**pinning - **N**uclear **M**agnetic **R**esonance Spectroscopy
DVS	**D**ynamic **V**apor **S**orption

* The synthesized compounds along with their identification numbers (IDs) are listed in **Table 4.2** (page 19).

Table of Contents

1. Introduction and Aim

Increasing concern towards environmental issues motivates researchers to develop alternative synthesis methods that are eco-friendly. Among different green methods, mechanochemistry is established as green and rapid synthesis route for preparing materials that range from small organic molecules to supramolecular entities.[2–20] In this approach, typically only small amounts of solvent or no solvent at all are needed avoiding environmental issues. The small, sub-stoichiometric amounts of solvent used in liquid-assisted grinding typically enhance the molecular mobility of reactants, accelerate the milling process, and subsequently improve the crystallinity of resulting polycrystalline products.[21–29] The latter aspect is essential since products are mainly powders and their crystal structures are determined *ab initio* from powder diffraction data. Moreover, mechanochemical reactions provide an opportunity for fabricating new materials with varying particle size, size distribution, and even morphologies that can influence final physiochemical properties of the resulting products.[30]

Coordination polymers (CPs) are functional materials consisting of metal nodes bridged by functionalized organic linkers to form one-, two-, or three-dimensional networks.[31,32] These materials offer interesting architectures and topologies with the ability of post-synthetic modifications for altering physicochemical properties of the resulting CPs.[33–37] Physiochemical properties such as porosity, crystallinity, thermal stability, and luminescence properties make CPs promising candidates for various applications in electronics, optics, catalysis, gas storage, purification, catalysis, and biomedicine.[38–47] The structural and physicochemical diversities of CPs are determined by the identity of metal cation, the nature of organic linkers, and reaction conditions.[30,48] Functionalizing organic linkers with uncoordinated functional groups, such as fluorine, amino-, hydroxyl-, and carboxyl-groups can alter the properties of CPs.[49–51] The replacement of hydrogen by fluorine in perfluorinated CPs is of interest due to the small size and hydrophobicity of fluorine that subsequently affects the physiochemical properties of resulting materials.[52–54] Moreover, hydrophobicity introduced by fluorination is used to improve the water stability of resulting compounds.[55]

CPs based on transition metals as metal nodes are intensively studied.[34,39,56,57] Recently, alkaline earth (AE) metals have attracted considerable attention as metal nodes for building

CPs for their varieties in coordination geometries depending on their cation radii.[45,58–61] AE metals possess high charge densities leading to strong interactions of functional materials like carboxylate anions.[45] In the coordination with polycarboxylate systems, AE metals have a larger radius and a higher affinity to oxygen atoms compared to transition metals.[45] Here, carboxylate linkers can have various reaction modes like monodentate-terminal, chelating, and bidentate-bridging that lead to the formation of 1D, 2D, or 3D architectures with the possibility of having an extensive connection driven by noncovalent interactions, such as hydrogen-bonding networks and π-π aromatic stacking.[57,59,62–64] AE metals are handy for aqueous preparations, which open doors for further applications.[59,65–67] In addition, the abundant and biocompatibility of AE ions make them promising for constructing economical and non-toxic CPs with interesting properties in gas separation,[65,68] molecule/ion recognition.[69,70] photochromic,[40,67] as well as photoluminescence-sensing.[71,72] These materials are typically synthesized under solvothermal conditions.[39,73–75] In 2006, James *et al.* reported the first synthesized metal-complex by grinding.[76] Since then, mechanochemistry is introduced as a rapid and green synthesis route for such materials.[77–92]

Motivation and Aim

CPs are usually synthesized under solvothermal conditions. Alkaline earth metals are rarely used as metal sources for constructing CPs. In this work, the mechanochemical syntheses are employed as a rapid and green method for synthesizing a series of Ca-, Sr-, and Ba-FCPs by milling metal hydroxides that vary in their water content and the perfluorinated benzene-dicarboxylic acids. The FCPs obtained by milling are compared to their fluorine-free counterparts (CPs) that are synthesized under the same conditions. Moreover, Ca-, Sr-, and Ba-CPs based on perfluorinated and fluorine-free nitrogen-containing ligands are explored via the easy access by ball milling. The crystal structures of the newly obtained compounds are determined *ab initio* from powder X-ray diffraction data. The local coordination around the respective metal is validated by X-ray absorption spectroscopy. The resulting compounds after milling are systematically investigated by analytical methods such as elemental analysis, MAS NMR, ATR-IR, gas sorption, dynamic vapor sorption, and scanning electron microscopy. Thermal stabilities are investigated by thermal analysis. BET surface areas are studied for the samples as-synthesized and after thermal treatment.

2. Literature Review

This chapter gives a review of the theoretical background and state of the art in mechanochemistry (**Section 2.1**), coordination polymers and compounds based on alkaline earth metals (**Section 2.2**), as well as the crystal structures determination of polycrystalline materials from powder X-ray diffraction data (**Section 2.3**).

2.1. Mechanochemistry

2.1.1. Historical Background

M. Faraday (1791-1867), M Carey Lea (1823-1897), and W. Spring (1848-1911) are known as the fathers of mechanochemistry.[93,94] Faraday's work had included accelerating the dehydration of the crystalline hydrates via mechanical treatments (scratching with a pin).[95,96] Carey Lea is well-known for his pioneer work on the decomposition of silver halides.[97,98] Carey Lea has proven that chemical changes induced by mechanical effect could be different from those known from thermochemical reactions. Spring is premiered in metathesis reactions.[94] In 1919, the term "mechano-chemistry" had been introduced by W. Ostwald describing chemical reactions in solid-state either initiated by a mechanical means or by involving reagents pre-activated via a mechanochemical treatment.[99] The first systematic study of a mechanochemical reaction has been reported by Taschakarov *et al.* in 1982.[100] The fundamental reactions by grinding have been reported by Rehbinder and Flavitsky.[94] Recently, mechanochemistry is used for synthesizing and developing dry processes by reducing the use of solvents which make it eco-friendly and cost-efficient than the adopted synthesis routes. With increasing concern towards environmental issues and global warming, the term "Green Chemistry" and its synonyms (e.g., clean-, environmental-, benign-, and sustainable chemistry) were introduced in the chemistry community.[101] Anastas and Warner published twelve principles of green chemistry that focus on using non-toxic, non-hazard, and eco-friendly materials. The green method should also benefit from sustainable energy and with no use of solvents or use minimal amounts of green solvents. Products should contain no waste or undesirable products, *etc*.[102,103] IUPAC provided a clear definition of green chemistry meaning "the invention, design, and application of chemical products and processes to reduce or to eliminate the use and generation of hazardous

substances".[104] Different matrices were proposed to evaluate reaction efficiency and green chemistry.[105]

2.1.2. Theoretical Background

The mechanically-induced chemical reactions are typically described as a combination of pressure and shear deformation considering the temperature effect. These factors strongly influence altering of physical and chemical properties of the subjected materials to mechanochemical treatments and subsequently the resulting products.[106] Here, understanding the role of each factor is of importance for studying the mechanical effect on chemical reactions. Tammann and Bridgman first investigated the influence of isostatic pressure (i.e., powders under equal load from all directions) on intermolecular distances of molecules.[93,107] The acceleration of reactions under a high 'controlled' pressure can be explained as an increase in the contact area between the solid particles of reactants. The combination of elevated pressure and shear deformation affect the reaction rate and thus increase the conversion level.

The hot-spot model assumes that mechanical impact creates hot spots.[108] In their work on the oxidation of metals, Fink and Hofmann argued that the increase in temperature is a result of oxidation rather than caused by friction.[109] Smekal stated that the increase in reactivity of solids is a consequence of mechanical deformation (mechanical activation).[94] Thiessen's magma-plasma deformation model is one of the first attempts at describing mechanochemical reactions.[94] Thiessen hypothesized that an energetic impact causes local heating and creates a highly excited plasma-like state around the impact point leading to an activation state with a high defect density of two particles in the contact area which results in instant chemical reaction and possibly the formation of unusual products.[96] Currently, monitoring mechanochemical reactions direct *in situ* allow revealing additional reliable data that might help in understanding mechanisms of mechanically induced reactions.[3,110–112]

2.1.3. Synthesis by Milling (Grinding)

Milling is one of the most common techniques in mechanochemistry due to the simplicity of experiments, and the continued development in the technology of mill equipment. The use of grinding goes back to the stone age (mortar and pestle).[113] Humans had used such tools for grinding food and stiff materials, therapists had profited mortar and pestle for mixing herbs,

and later scientists have used these mechanical approaches for inducing chemical changes. Obtaining elemental mercury by grinding cinnabar could be the first documented mechanochemical reaction in history (in the 4th century BC).[114] Retsch has developed the first motorized mill. Later on, balls have been used in tumbler mills to grind large quantities of solids to fine particle size. In 1922, Szegvari devised a stirred-ball attritor mill. The vibrational mill has been used for the first time in Germany around 1930.[113] To increase the impact of ball milling in a small tumbling mill; the milling drum has been introduced to a centrifuge for simulating a larger acceleration of gravity. Here lies the idea of the planetary mill that has been first produced by Fritsch Co. in 1961.[94] The planetary mill provides parameters for impact and friction that can be adjusted for a chosen reaction (**Figure 3.1**).[115]

2.1.4. Research in Mechanochemistry

Mechanically-induced solid-state reactions in the form of solvent-free or solvent-catalyzed approaches were recently established as easy and rapid synthesis method for preparing various materials in chemistry.[2,3,85,116] Mechanochemistry is gaining great interests not only as an alternative to conventional solution-based treatments but also for its promising environmental and economic benefits.[103,105] Chemical and physical properties of the mechanochemically obtained powder materials are investigated using analytical methods like powder X-ray diffraction, solid-state nuclear magnetic resonance spectroscopy, Infrared spectroscopy, and thermal analysis.[117–119] One of the recent application of mechanochemistry is the synthesis of coordination polymers by milling.

2.2. Coordination Polymers

2.2.1. Terminology

Metal-organic complexes are prepared from the combination of metal cations, and organic ligands capable of bridging metal centers to create polymeric structures. These structures can be one, two or three dimensions. Different terminologies have been used for describing solid-state structures of these hybrid materials. The term “Coordination Polymer” has been first used in the 1950s while the term “Metal-Organic Frameworks” was used from 1990s.[120] following IUPAC recommendations in 2013, the term “Coordination polymer’’ (CP) is recommended for describing coordination compounds with one, two, or three

dimensionalities. The term “metal-organic framework’’ (MOF) is a subset of CPs and is recommended for describing the coordination networks containing potential voids.[32]

2.2.2. Synthesis and Characterization

The synthesis of CPs and MOFs has been a highly dynamic research field in the last two decades.[30,39,121–123] Variations in synthesis methods have a substantial impact on yields as well as particle size and morphology, in addition to the possible implementation in large-scale production of desired materials.[30] The synthesis of CPs is usually carried out under solvothermal conditions. Alternative methods like electrochemical and sonochemical methods as well as microwave-assisted synthesis are used for producing CPs.[30,124] Only recently mechanochemical synthesis, typically milling, was introduced as an alternative synthesis route which open doors for obtaining CPs using a rapid and green method.[78,80]
Various analytical methods are used for the investigation of CPs obtained by milling. For example, elemental analysis is used for measuring elemental compositions. Powder XRD is crucial for qualitative analysis and *ab initio* structures determination. Thermal stabilities are investigated by thermal analysis. Purity and structural properties can be validated using MAS NMR, and IR-spectroscopy. X-ray absorption spectroscopy measurements provide information about the local coordination of metals. Scanning electron microscopy images give an overview of morphologies and size distribution. Sorption properties and surface areas can be studied via nitrogen isotherms and dynamic vapor sorption measurements. However, these methods, among others, can diverse depending on properties and desired applications of the investigated materials.

2.2.3. Properties and Applications

The primary goal of synthesis methods is to obtain CPs that exhibit topological nature and physicochemical properties like porosity, shape, host-guest interactions, thermal-, and mechanical stabilities. Such distinguished properties make CPs promising candidates for a wide range of applications such as separation, storage, and catalysis.[30,39] Furthermore, the uses of CPs in biomedicine and electronics are currently investigated.[125–127]

2.2.4. Fluorine-Containing CPs

Omary and co-workers and Cheetham and co-workers reported on fluorinated metal-organic compounds that demonstrate high gas adsorption properties.[128–130] In contrast, Kim *et al.*, and Banerjee *et al.* found that fluorination does not necessarily enhance the adsorption properties due to the decrease in pore size of the resulting compounds.[50,131] Our results on benzene-dicarboxylates and tetrafluorobenzene-dicarboxylates based coordination polymers comprising the alkaline earth metals Ca, Sr, and Ba,[83,84,87] support the latter findings. Obviously, such characteristic properties are specific to a given system and can vary among different systems.[50] On the other hand, CPs with small pore sizes are proposed to be suitable for hydrogen storage applications.[132–134] Yang *et al.* explored for the first time the synthesis of fluorinated CPs (FCPs) using perfluorinated polycarboxylate ligands that maintain enhanced H_2 adsorption.[128,129,135] Theoretical calculations indicate that the presence of fluorine atoms leads to strong interactions between the hybrid surface and H_2 molecules.[135,136]

2.2.5. Alkaline Earth Metals-based CPs

The abundance and biocompatibility of alkaline earth (AE) ions (Mg^{2+}, Ca^{2+}, and Sr^{2+}) make them promising for constructing economical and non-toxic CPs with interesting properties in gas sorption and separation,[65,68] photochromic,[40,67] as well as photoluminescence-sensing.[71,72] Due to their non-toxicities and the relative lightweights, magnesium and calcium are promising elements for synthesizing CPs with the possibility of implementations in biological and gas storage applications.[59,65–67] The AE ions can be incorporated to tune structural variations in transition metal-organic compounds and for obtaining new heterometallic CPs with promising properties.[137,138] Studies on the influence of AE metal cation sizes by Côté and Shimizu, Duan *et al.*, Falcão *et al.*, and Huang *et al.* indicate that increasing metal sizes lead to the formation of CPs with higher dimensionalities.[64,70,75,139] In CPs based on polycarboxylate systems, AE metals have a larger radius and a higher affinity to oxygen atoms compared to transition metals.[45]

In a recent study, Coles and co-workers reported that the alkaline earth metal-benzene dicarboxylate and their fluorinated counterparts could be used for designing efficient pyrotechnic materials.[140] Usman *et al.* lately reported a dehydrated Sr-Isophthalate that has

a very low dielectric constant making it a potential interlayer dielectric in integrated circuits.[141] Zhang *et al.* explored Ca-benzene-tetracarboxylate as an anode material for sodium-ion batteries due to stabilities and low solubility of Ca-frameworks in electrolytes.[142] FCPs and CPs comprising AE metals are usually synthesized under hydro- and solvothermal conditions. Only recently, mechanochemistry was introduced as rapid and green synthesis route.[76,80]

Different AE-CPs based on the *ortho*-, *meta*-, and *para*-isomers of benzene-dicarboxylates and their fluorinated analogs are listed in the Cambridge Structural Database (CSD).[143] For instance, Ca-phthalate monohydrate was reported by Gupta *et al.*, Schuckmann *et al.*, and Zhang *et al*.[144–146] Hydrated Ca-isophthalates were reported by Dale *et al.,* and Yu *et al*.[147,148] Ca-terephthalate trihydrate was reported by Matsuzaki *et al.*, Groeneman *et al.*, Dale *et al.*, and Zhang *et al*.[146,149–151] All these compounds were prepared via autoclave, hydro-, or solvothermal treatments. The latter compound was also successfully prepared in our research group via a mechanochemical synthesis route.[83] A dehydrated Ca-terephthalate was obtained after a thermal post-treatment of the hydrated Ca-terephthalate in a reversible phase transition process.[83,152]

Blair *et al.* reported on a series of Sr-CPs that contain nitrate, DMF, or pyridine molecules and based on fluorinated and fluorine benzene-dicarboxylic systems such as Sr-tetrafluoroterephthalate, Sr-tetrafluoroisophthalate, Sr-tetrafluorophthalate.[153] In the crystal structures of Sr-terephthalate, the coordination numbers (C.N.) of Sr-cations vary between eight,[154] and ten[150]. A Sr-terephthalate trihydrate was also obtained via a mechanochemical reaction.[84]

Examples for Ba-CPs based on fluorinated and fluorine-free benzene-dicarboxylic systems were described.[143] For instance, Coles and co-workers described Ba-tetrafluorophthalate and Ba-tetrafluoroterephthalate.[140] Another ethanol- and DMF-containing Ba-tetrafluoroterephthalate was reported by Ruschewitz and co-workers.[155] A Ba-phthalate that contains nitrate anions was prepared by Zhang *et al*.[146] Ba-terephthalate was reported by Lo *et al.* and Groeneman *et al*.[150,156] In the reported crystal structures, the C.N. of the Ba^{2+}-ion varies between eight (as in Ba-tetrafluoroterephthalate), nine (as in Ba-tetrafluorophthalate), and ten (as in Ba-terephthalate). No crystal structures were reported for Ba-tetrafluoroisophthalate and Ba-isophthalate. These reported compounds

were prepared via hydro- and solvothermal treatments excluding our reported Ba-terephthalate and Ba-tetrafluoroterephthalate that were prepared via mechanochemical reactions.[83,87] Few examples of AE metals-CPs based on aminobenzoic acids are found. For instance, Murugavel *et al.* prepared AE metals-CPs based on anthranilic acid using metal chlorides as metal sources and water/methanol as solvents.[157] Arlin *et al.* published AE metals-CPs based on *ortho*- and *para*-aminobenzoic acids.[60] We found no examples of the perfluorinated aminobenzoate systems.

2.3. Structure Determination from Powder X-ray Diffraction Data

Mechanochemical reactions open new pathways that could lead to the formation of different products from those obtained by solution-based reactions. Chemical reactions by milling yield typically microcrystalline powders that are usually not suitable for structures determination by single crystal X-ray diffraction (SCXRD). However, attempts to recrystallize the mechanochemically obtained powders often yield products with different structures.[110,158] Here, structures determination from powder XRD (PXRD) data is a pathway for elucidating the crystal structures of powder materials.[159] Though, the structures solution from powder data is challenging and is not routinely applied in the area of CPs.[160,161]

PXRD patterns are typically used to determine crystallinity and purity of CPs samples. Phase purity is usually confirmed by comparing PXRD data of the newly formed samples with reactants and expected byproducts of the synthesis. Once the crystallinity and the phase purity of a sample are established, other information like unit cell size, cell parameters, and crystal systems can be derived from the recorded PXRD pattern. Determination of a crystal structure from PXRD data contains three main stages including (1) Indexing which incorporates the determinations of lattice parameters, unit cell symmetry, and then the assignment of space group. (2) Structure solution is based on global optimization methods yielding a model close to the true structure. (3) Refinement of the structural model via local optimization methods. The composition and structural properties of a refined crystal structure are validated via different analytical methods like elemental analysis, thermal analysis, MAS NMR, and Infrared spectra. In a metal-containing sample, the local coordination around a metal cation can be investigated via X-ray absorption spectroscopy, and then the validation of the determined structure by simulating the measured spectra along with the structural model.

3. Methodologies and Apparatus

3.1. Planetary Mill

All mechanochemical reactions were performed in a commercial planetary mill "Pulverisette 7 premium line" (Fritsch, Germany) under access to air. Silicon nitride grinding bowl (volume: 45 ml) were filled with 1 g of a powder mixture and assembled with five silicon nitride balls (12 mm in diameter, 2.8 g each). A ball to powder mass ratio of 14 was ensured. All samples were milled with a rotational speed of 600 rpm. Typical reaction time range from one to four hours. Short syntheses (1 h milling) were not interrupted. In the case of the reactions run over 4 hours, the reaction was interrupted for 30 min every 60 min to cool down the equipment.

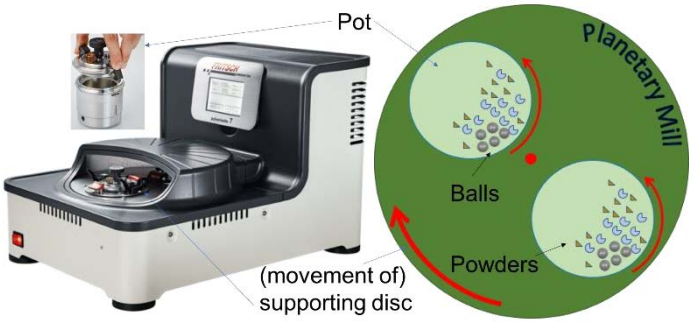

Figure 3.1: (a) The model of planetary mill used for the synthesis of CPs (retrieved from Fritsch.de on 01.01.2018). (b) Schematic representation of a planetary mill. Supporting disc (green), pots (light green), balls (grey), and powders (yellow and blue). The movement of supporting disc and the counter direction of pots are represented as red arrows.

3.2. Powder X-ray Diffraction

Three different lab instruments and one synchrotron X-ray source were used for recording the powder X-ray diffraction (PXRD) data. For synthesis control, X-ray diffractograms were recorded with a XRD-3003-TT diffractometer (Seiffert & Co., Freiberg, Germany) with Cu-K_α radiation (λ = 1.542 Å; step scan: 0.05°, step time: 5 s). The samples were measured in a 2θ range of 5° - 65°. Reflections were compared with diffractograms of the JCPDS-PDF database.[162] For structure solution, PXRD measurements were performed with a D8 Discover diffractometer (Bruker AXS, Karlsruhe, Germany) operated in transmission geometry with Cu-$K_{\alpha1}$ radiation (λ = 1.54056 Å, step scan: 0.009°, step time: 5 s), equipped with a Lynxeye detector. Samples were prepared in glass capillaries (diameter 0.5 mm) and were measured in a 2θ range of 5° - 65°. Typical data acquisition before collection range from 17 to 36 h.

PXRD measurements were also performed with a Stoe Stadi MP diffractometer (STOE & Cie. GmbH, Darmstadt, Germany) operated in transmission geometry with Mo-$K_{\alpha 1}$ radiation (λ = 0.709300 Å, step scan: 0.015°), equipped with a Mythen 1K detector. Synchrotron radiation PXRD patterns were measured in Rapid Access Beamline (I11, Diamond, UK). Samples were prepared in glass capillaries (diameter 0.5 mm). Calibrations were performed using Si standard powder (NIST SRM640c). Wavelength, λ = 0.825862(10) Å. 2θ zero-point = 0.008835(3)° and with a beam current of 300 mA.

3.3. Structure Determination

The crystal structures were determined *ab initio* starting from the PXRD data. PXRD patterns were indexed for the first 20 lines with the program DICVOL implemented in the DASH software package and with TOPAS.[163–165] Adequacies of the unit cells and space groups assignments were validated by the profile refinements of whole patterns without structural parameters using the *LeBail* method.[166,167] Structures were solved using DASH software and based on conventional simulated annealing (SA) routine.[163] EXPO14 software was also used for structures determination and based on a combination of the *Big Bang-Big Crunch* (HBB-BC) and traditional simulated annealing (SA) for reducing the computational cost.[168,169] For every run 50 trial structures were generated. The structural models were ranked based on their goodness of fit to the experimental powder pattern. The best fitting structural models were refined along with the experimental PXRD data by the Rietveld method using the fundamental parameter approach as reflection profiles (emission profiles with axial instrument contributions and crystallite microstructure effects).[164] In the first step of the refinement the background and reflection shape functions were fitted then unit cell parameters were refined. All atomic coordinates were refined except for atoms with special positions and aromatic rings. In the latter, a combination of rigid bodies, bond length, bond angle, and ring planarity restraints were used. Atomic vibrations were modeled by a single thermal parameter. Hydrogen atoms were located geometrically. The cell parameters and refinement factors are given in the Tables correspond to crystal data. Wherein, R_p and R_{wp} values refer to the Rietveld criteria of fit for profile and weighted profile defined by Langford and Louër.[170]

3.4. Elemental Analysis

An EURO EA equipment (HEKAtech GmbH) was used for carbon and hydrogen content determinations. The fluorine content was determined with a fluoride sensitive electrode after conversion of the solids with Na_2CO_3/K_2CO_3 into a soluble form. The typical amount of a sample for measurements is 1 mg.

3.5. Thermal Analysis

Thermogravimetry (TG) and differential thermal analysis (DTA) measurements were performed simultaneously on a thermobalance TAG 24 (SETARAM, Caluire, France). For this purpose, the samples (initial mass ≈ 12 mg) were filled into 100 µl corundum-crucibles with corundum cover and heated under a flow of argon and synthetic air at a rate of 10 K/min up to 600 or 1000 ˚C. For simultaneous analysis of evolved gasses, a mass spectrometer (Balzers Quad-star 421) was coupled by a heated (180 ˚C) quartz glass capillary. Measurements were performed in MID (multiple ion detections) modes.

3.6. Magic Angle Spinning NMR

^{1}H, ^{19}F, and $^{1}H \rightarrow {}^{13}C$ CP MAS NMR spectra were recorded on a Bruker AVANCE 400 spectrometer (Larmor frequencies: ν_{1H} = 400.1 MHz, ν_{13C} =100.6 MHz and ν_{19F} =376.4 MHz) using both a 2.5 mm and a 4-mm double-bearing magic angle spinning (MAS) probe (Bruker Biospin). ^{1}H MAS studies were recorded with a $\pi/2$ pulse length of 3.6 µs and a recycle delay of 5 s. Values of the isotropic chemical shifts of ^{1}H and ^{13}C are given with respect to TMS. Contact times of 1 ms and 10 ms were used for the $^{1}H \rightarrow {}^{13}C$ CP MAS NMR experiments. ^{19}F MAS NMR spectra were performed with a $\pi/2$ pulse duration of 3.6 µs, a spectrum width of 400 kHz, a recycle delay of 5 s and accumulation number of 64. The isotropic chemical shifts δ_{iso} of ^{19}F resonances are given concerning the $CFCl_3$ standard. Existent background signals of ^{19}F were suppressed with the application of a phase-cycled depth pulse sequence according to Cory and Ritchey.[171] The simulation of MAS NMR spectrum was performed using the DMFIT software.[172]

3.7. Infrared Spectroscopy

Fourier transform Infrared spectra (FT-IR) were recorded with an Equinox 55 IR microscope (Bruker), using the potassium bromide (KBr) pellet technique in the range of 4000 - 400 cm^{-1}. The sample weight was 1 mg in a pellet of 500 mg KBr. Attenuated Total Reflection-Infrared

(ATR-IR) spectra were measured using an Equinox 55 FT-IR spectrometer (Bruker, Ettlingen, Germany). The ATR-IR spectra were recorded by averaging 100 scans at a 2 cm^{-1} resolution.

3.8. Gas Sorption

Nitrogen sorption experiments were carried out on an ASAP 2010 and ASAP 2020 (Micromeritics, Norcross, USA) at a temperature of 77 Kelvin. Before the measurements, the samples were degassed at room temperature, 200 ˚C, 240 ˚C, 260 ˚C, 290 ˚C, or 390 ˚C for 24 h in vacuum. Specific surface areas were calculated by the Brunauer-Emmett-Teller (BET) method[173,174] with a molecular sectional area of 0.162 nm² according to ISO 9277 (2010).[175]

3.9. Dynamic Vapor Sorption

Water and n-octane dynamic vapor sorption (DVS) experiments were performed on the DVS-1 instrument (Surface Measurements Systems, London, UK). The DVS System is a gravimetric sorption apparatus consists of a thermostated sample chamber for setting a constant temperature of the sample and a flow controller for producing a controllably variable vapor pressure. The adsorbed mass is determined by continuous weighing as a function of the relative pressure. The isotherms were measured over a range of 0 – 98% relative humidity (RH) at a temperature of 25˚C.

3.10. Extended X-ray Absorption Spectroscopy

EXAFS spectra were recorded for the Ca and Sr elements with absorption edges at 4.038 keV and 16.107 keV, respectively. For this purpose, EXAFS measurements were performed at two different beamlines. The beam was monochromatized using a double-crystal monochromator (DCM).

Ca-containing samples were measured at the B18 beamline (Diamond, Oxford UK) in Rapid Access mode. The measurements were performed at the K edge for Ca (at 4.038 keV). The measurements were acquired in a quick-EXAFS mode in the range of 3.838-5.000 keV, and a nominal step size of 0.3 eV was used. Ca-samples were used as-synthesized, and the fine powders were fixed between two strips.

Sr-containing samples were measured at the BAM*line* (BESSY-II, Berlin, Germany). In this case, the measurements were performed conventionally, in which the size of the beam spot was 8x1 mm. The measurements were performed at the K edge for Sr (16.107 keV). The energy was scanned in the following manner; from -100 eV to -20 eV below the edge in

10 eV steps, from -19 eV below the edge to 20 eV above the edge in 0.5 eV steps, from 21 eV to 100 eV above the edge in 1.5 eV steps and the EXAFS range was scanned in equidistant k steps of 0.04 Å until k=14 Å. Sr-samples were diluted by boron nitride. The diluted samples were fixed in plastic sample holders between two Kapton foils. Every sample was repeatedly measured. As detectors, two ionization chambers were used for the primary beam (I_0) and the absorption of the sample, respectively.

The data treatments were carried out using the Demeter software package (Artemis & Athena). These GUIs programs belong to the software package IFEFFIT (v. 1.2.11).[176] For better assignation of the coordination number and interatomic distances, EXAFS simulations of the determined crystal structures were carried out in FEFF and compared with the measured spectra.[177]

3.11. Scanning Electron Microscopy

The scanning electron microscopy (SEM) imaging of the powder samples was performed on a Zeiss Gemini Supra-40 instrument operated with an acceleration voltage of 10 kV at a working distance of 8.5 mm.

3.12. Graphical Representation

Figure 3.2 shows the graphical representation used for the visualization of crystal structures along this thesis.

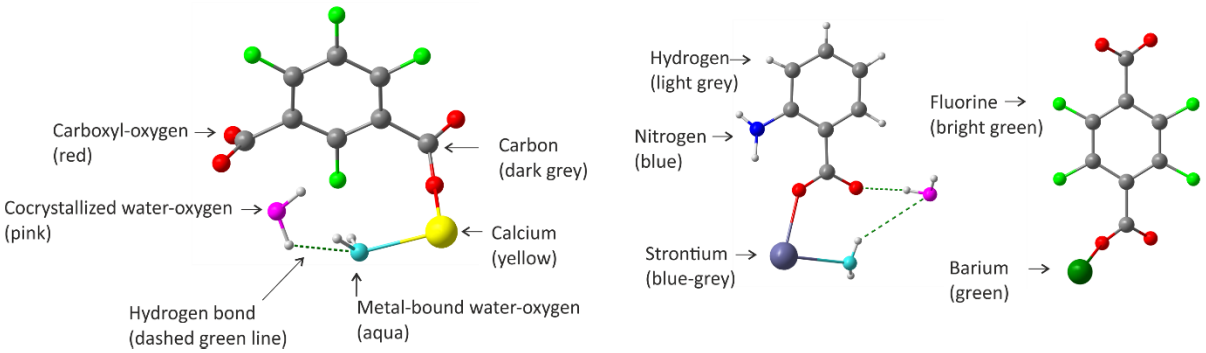

Figure 3.2: Graphical representation (Ball-and-stick model) and color code of atoms used in the depicted crystal structures. For the isomorphic structures of Ca- and Sr-compounds, calcium (yellow) is used for the representation of metals.

4. Materials and Synthesis

The used chemicals for the syntheses are listed in **Section 4.1**. In **Section 4.2**, the mechanochemical syntheses of the coordination polymers are described.

4.1. Chemicals

All chemicals were ordered from Sigma-Aldrich and used without further purification. The chemicals are listed in **Table 4.1** including the corresponding JCPDS-PDF database,[178] and references of crystal structures.[143]

Table 4.1: List of used chemicals, purity, ICDD PDF-cards for inorganic samples and CCDC Refcodes for organic ligands.

Chemical	**Formula**	**Abbrev.**	**Purity**	
Metal hydroxides		-		**PDF-Card.**[162]
Calcium hydroxide	$Ca(OH)_2$	-	≥96%	44 - 1481
Strontium hydroxide	$Sr(OH)_2$	-	94%	27 - 847
Strontium hydroxide octahydrate	$Sr(OH)_2{\cdot}8H_2O$	-	≥97%	27 - 1438
Barium hydroxide	$Ba(OH)_2$	-	95%	22 - 1054
Barium hydroxide monohydrate	$Ba(OH)_2{\cdot}H_2O$	-	≥99%	24 - 104
Barium hydroxide octahydrate	$Ba(OH)_2{\cdot}8H_2O$	-	≥98%	26 - 155
Organic Linkers				**Refcode.**[143]
Tetrafluoroterephthalic acid	(C_6F_4)-1,4-$(COOH)_2$	H_2*p*BDC-F_4	97%	BITCEM13.[179]
Tetrafluoroisophthalic acid	(C_6F_4)-1,3-$(COOH)_2$	H_2*m*BDC-F_4	96%	ODUSEM.[180]
Tetrafluorophthalic acid	(C_6F_4)-1,2-$(COOH)_2$	H_2*o*BDC-F_4	98%	BOLNAR.[181]
Terephthalic acid	(C_6H_4)-1,4-$(COOH)_2$	H_2*p*BDC	98%	TEPHTH.[182]
Isophthalic acid	(C_6H_4)-1,4-$(COOH)_2$	H_2*m*BDC	99%	BENZDC01.[183]
Phthalic acid	(C_6H_4)-1,4-$(COOH)_2$	H_2*o*BDC	≥99.5%	PHTHAC02.[184]
p-aminotetrafluorobenzoic acid	4-(NH_2)-(C_6F_4)-(COOH)	*p*ABAH-F_4	99%	-
Tetrafluoroanthranilic acid	2-(NH_2)-(C_6F_4)-(COOH)	*o*ABAH-F_4	98%	UTOHAN.[185]
p-amino-benzoic acid	4-(NH_2)-(C_6H_4)-(COOH)	*p*ABAH	≥99%	AMBNAC01.[194]
m-amino-benzoic acid	3-(NH_2)-(C_6H_4)-(COOH)	*m*ABAH	98%	AMBNZA.[186]
Anthranilic acid	2-(NH_2)-(C_6H_4)-(COOH)	*o*ABAH	≥98%	AMBAZACO07.[206]

4.1.1. Metal Hydroxides

Alkaline earth (AE) metals are typically introduced to milling in their oxide, hydroxide, carbonate, acetates, hydrides, halides, or nitride forms.[81,83,84,187–194] Ca-, Sr-, and Ba-hydroxides have been successfully used as inorganic precursors for synthesizing coordination polymers based on terephthalic acid.[83] Therefore we employed metal hydroxides as green sources for our synthesis. Moreover, water (which is formed as

a byproduct) assists for stabilizing the resulting coordination polymers (CPs). The ICDD-PDF cards correspond to metal hydroxides are given in **Table 4.1**.

4.1.2. Organic Linkers

The used organic linkers include the isomers of tetrafluorobenzene-dicarboxylic acid ($H_2BDC\text{-}F_4$) and their nonfluorinated analogs (H_2BDC). Amino-tetrafluorobenzoic acids ($ABAH\text{-}F_4$) and their fluorine-free analogs (ABAH) are also explored as organic linkers in their coordination with AE ions. The substitution of hydrogens by fluorine atoms in the perfluorinated ligands affects both of acidity and planarity of the carboxylic groups.

Torsion Angles: The two carboxylic groups in *para*- and *meta*-isomers of Benzene-dicarboxylic systems (H_2BDC) and aminobenzoic acids (ABAH) lie in the plane with the benzene ring to maximize the stabilization caused by the resonance effect.[195] In *ortho*-phthalic acid (H_2oBDC), one of the two adjacent carboxylic groups is planar (with a torsion angle of 10°), the second has an off-planar orientation with a dihedral angle = 84° concerning benzene ring to reduce steric repulsion caused by the neighboring carboxylic group. The steric hindrance is with little effect in both of *para*- and *meta*-positions.[196] Carboxylic groups are twisted out the plane of the F-containing benzene ring due to the electrostatic repulsion between the highly electronegative fluorine and the lone-pair of carboxylate oxygen atoms. The acidity is enhanced by the decrease in the aromaticity of carboxylic groups conjugated with the aromatic systems which caused by the electron-withdrawing nature of fluorine atoms on the ring.[180,197] Such higher degree of torsional diversities in perfluorinated ligands are assumed to build up supramolecular CPs with more flexibilities.[180]

Crystal Structures and PXRD data: The measured PXRD patterns of organic linkers match the simulated data from their corresponding crystal structures (**Table 4.1**). For $H_2mBDC\text{-}F_4$, the reflections in the measured PXRD pattern are slightly shifted compared to the simulated data from the reported crystal structure.[180] However, the Rietveld refinement of the measured data along with the known structure confirms the crystal structure (**Figure A.2a**). The crystal structure of 4-amino-tetrafluorobenzoic acid ($pABAH\text{-}F_4$) is not reported. Here, the crystal structure was determined from PXRD data and subsequently refined via the Rietveld method (**Figure A.1b**, **Figure A.2c,** and **Table A.1**). Crystal structures of the organic linkers are associated in the solid state by intermolecular hydrogen bonding between carboxylic groups and amino groups.[198,199]

4.2. Mechanochemical Synthesis

The newly formed coordination polymers (CPs) were synthesized by milling the metal hydroxides (with varying water content) and the organic linkers. The obtained compounds along with their identification numbers are listed in **Table 4.2**.

4.2.1. Ca-, Sr-, and Ba-FCPs based on Tetrafluorobenzene-Dicarboxylic Acids

The mechanochemical synthesis routes of $[Ca(BDC\text{-}F_4)(H_2O)_n]$ (IDs: **1**,**3**,**5**), $[Sr(BDC\text{-}F_4)(H_2O)_n]$ (IDs: **2**,**4**,**6**), and $[Ba(BDC\text{-}F_4)(H_2O)_n]$ (IDs: **12**-**14**) are described in **Scheme 4.1**. The applied molar ratio between the metal hydroxide and the organic linker is 1:1. The time for milling was varied between 1 and 4 h.

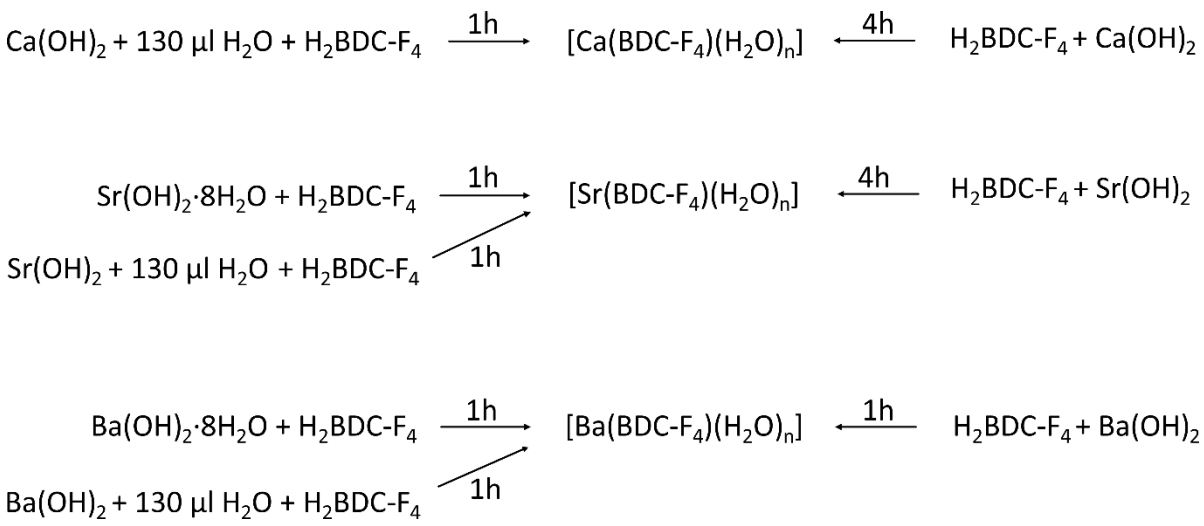

Scheme 4.1: Reaction paths for the formation of Ca-, Sr-, and Ba-FCPs $[M^{II}(BDC\text{-}F_4)(H_2O)_n]$ by the milling of tetrafluorobenzene-dicarboxylic acids ($H_2BDC\text{-}F_4$) and metal hydroxides that vary in their water content. The molar ratio between inorganic and organic samples is 1:1. Milling time is written above the arrows.

4.2.2. Ca-, Sr-, and Ba-CPs based on Benzene-Dicarboxylic Acids

The mechanochemical synthesis routes of $[Ca(BDC)(H_2O)_n]$ (IDs: **7**,**8**,**10**), $[Sr(BDC)(H_2O)_n]$ (IDs: **9**,**11**), and $[Ba(BDC)(H_2O)_n]$ (IDs: **15**,**16**) are described in **Scheme 4.2**. The applied molar ratio between the metal hydroxide and the organic linker is 1:1. The time for milling was 1 h.

$$Ca(OH)_2 + 130\ \mu l\ H_2O + H_2BDC \xrightarrow{1h} [Ca(BDC)(H_2O)_n]$$

$$Sr(OH)_2{\cdot}8H_2O + H_2BDC \xrightarrow{1h} [Sr(BDC)(H_2O)_n]$$

$$Ba(OH)_2{\cdot}8H_2O + H_2BDC \xrightarrow{1h} [Ba(BDC)(H_2O)_n]$$

Scheme 4.2: Reaction paths for the formation of Ca-, Sr-, and Ba-coordination polymers $[M^{II}(BDC)(H_2O)_n]$ by the milling of benzene-dicarboxylic acids (H_2BDC) and metal hydroxides. The molar ratio between inorganic and organic samples is 1:1. Milling time is written above the arrows.

4.2.3. Ca-, Sr-, and Ba-CPs based on Amino-Benzoic Acids

The mechanochemical synthesis routes of $[Ca(oABA)_2(H_2O)_3]$ (ID: **17**), $[Sr(oABA)_2(H_2O)_3]$ (ID: **18**), and $[Ba(oABA)_2(H_2O)]$ (ID: **18**) are described in **Scheme 4.3**. The applied molar ratio between the metal hydroxide and the organic linker is 1:2, respectively. The time for milling was 1 h.

$$Ca(OH)_2 + 130\ \mu l\ H_2O + 2(ABAH) \xrightarrow{1h} [Ca(ABA)_2(H_2O)_n]$$

$$Sr(OH)_2{\cdot}8H_2O + 2(ABAH) \xrightarrow{1h} [Sr(ABA)_2(H_2O)_n]$$

$$Ba(OH)_2{\cdot}8H_2O + 2(ABAH) \xrightarrow{1h} [Ba(ABA)_2(H_2O)_n]$$

Scheme 4.3: Reaction paths for the formation of $[M^{II}(ABA)_2(H_2O)_n]$ starting from metal hydroxides (M = Ca, Sr, or Ba). The molar ratio between inorganic and organic samples is 1:2, respectively. Milling time is written above the arrows. The milling reactions were performed in a planetary mill.

Table 4.2: List of the fluorinated and fluorine-free coordination polymers obtained by milling Ca-, Sr-, and Ba-hydroxides with the perfluorinated and fluorine-free benzene-dicarboxylic acids, along with their identification numbers used in this thesis. The abbreviations of organic ligands: Tetrafluoroterephthalic acid (H_2*p*BDC-F_4), tetrafluoroisophthalic acid (H_2*m*BDC-F_4), tetrafluorophthalic acid (H_2*o*BDC-F_4), terephthalic acid (H_2*p*BDC), isophthalic acid (H_2*m*BDC), phthalic acid (H_2*o*BDC). Also, Ca-, Sr-, and Ba-CPs based on anthranilic acid (*o*ABAH) are listed

	Formula	Identification number (ID).
Ca- and Sr-FCPs	[Ca(*p*BDC-F_4)$(H_2O)_4$]	**1**
	[Sr(*p*BDC-F_4)$(H_2O)_4$]	**2**
	[{Ca(*m*BDC-F_4)$(H_2O)_2$}·H_2O]	**3**
	[{Sr(*m*BDC-F_4)$(H_2O)_2$}·H_2O]	**4**
	[Ca(*o*BDC-F_4)$(H_2O)_2$]	**5**
	[Sr(*o*BDC-F_4)$(H_2O)_2$]	**6**
Ca- and Sr-CPs	[Ca(*p*BDC)$(H_2O)_3$]	**7**
	[Ca(*m*BDC)$(H_2O)_{3.4}$]	**8**
	[{Sr(*m*BDC)$(H_2O)_{3.4}$]	**9**
	[Ca(*o*BDC)(H_2O)]	**10**
	[Ca(*o*BDC)], 290 °C	**10-H_2O**
	[{Sr(*o*BDC)$(H_2O)_2$}·H_2O]	**11**
Ba-FCPs and Ba-CPs	[Ba(*p*BDC-F_4)$(H_2O)_{0.5}$]	**12**
	[Ba(*m*BDC-F_4)$(H_2O)_{0.5}$]	**13**
	[Ba(*o*BDC-F_4)$(H_2O)_{1.5}$]	**14**
	[Ba(*m*BDC)$(H_2O)_{2.5}$]	**15**
	[Ba(*o*BDC)$(H_2O)_1$]	**16**
M^{II}-Anthranilates	[Ca(*o*ABA)$_2(H_2O)_3$]	**17**
	[{Sr(*o*ABA) $_2(H_2O)_2$}·H_2O]	**18**
	[Ba(*o*ABA)$_2(H_2O)$]	**19**

5. Results and Discussions

This chapter discusses the results of milling, crystal structures, and characterization of the coordination polymers that are based on the alkaline earth metals and the perfluorinated and fluorine-free benzene-dicarboxylate systems. The fluorinated coordination polymers (FCPs) are based on tetrafluoroterephthalic acid (H_2*p*BDC-F_4), tetrafluoroisophthalic acid (H_2*m*BDC-F_4), and tetrafluorophthalic acid (H_2*o*BDC-F_4). The obtained FCPs are compared to their fluorine-free counterparts (CPs) that were synthesized under the same conditions. The fluorine-free CPs are based on terephthalic acid (H_2*p*BDC), isophthalic acid (H_2*m*BDC), and phthalic acids (H_2*o*BDC). Moreover, the influence of metal cation size on the coordination system of Ca-, Sr-, and Ba-Anthranilates are discussed.

In **Section 5.1**, the Ca- and Sr-FCPs based on the isomers of H_2BDC-F_4 are discussed, bearing in mind that Ca- and Sr-FCPs crystallize isomorphously in their coordination to a respective perfluorinated ligand. The Ca- and Sr-CPs based on the isomers of H_2BDC are studied in **Section 5.2**. The FCPs and CPs comprising Ba^{2+}-ions are discussed in **Section 5.3**. In **Section 5.4**, the fluorinated and fluorine-free systems are compared. The comparison focuses on the mechanochemical synthesis including the influence of water contents on milling process and the resulting products as well as the influence of fluorine atoms and geometries of organic linkers on the physicochemical properties of the resulting FCPs and CPs. **Section 5.5** focuses on the effect of the metal cation sizes of Ca^{2+}-, Sr^{2+}-, and Ba^{2+}-ions in their coordination with anthranilic acid (*o*ABAH). The FCPs and CPs discussed in this thesis are listed in **Table 4.2** (page 19).

5.1. Ca- and Sr-(Tetrafluorobenzene-Dicarboxylates): $[M^{II}(BDC\text{-}F_4)(H_2O)_n]$

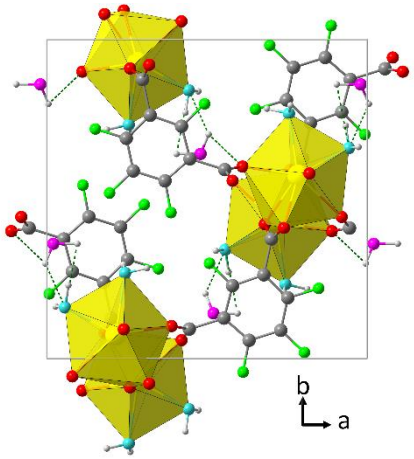

i. A. Al-Terkawi, G. Scholz, F. Emmerling, E. Kemnitz. *Cryst. Growth Des.* **2016**, *16*, 1923–1933.

ii. A. Al-Terkawi, G. Scholz, A. G. Buzanich, S. Reinsch, F. Emmerling, E. Kemnitz. *Dalton Trans.* **2017**, *46*, 6003-6012.

iii. A. Al-Terkawi, G. Scholz, Emmerling, E. Kemnitz. *Dalton Trans.* **2017**, *46*, 12574–12587.

iv. A. Al-Terkawi, G. Scholz, F. Emmerling, E. Kemnitz. (*Dalton Trans., accepted*).

Scientific Aspects:

- Ca- and Sr-FCPs based on the isomers of tetrafluorobenzene-dicarboxylic acid were mechanochemically synthesized.
- Variations in the water content of the inorganic sources do not influence the coordination systems. The presence of water during milling affects the crystallinity of final products and reduces the milling time for complete conversion.
- Crystal structures of the FCPs were determined from powder XRD data.
- Fluorine atoms and geometries of organic linkers play a crucial role in the structural diversity of the FCPs.
- The cation radii of Ca^{2+}- and Sr^{2+}-ions have minor effect on the final FCPs.
- $[Ca(p\text{BDC-}F_4)(H_2O)_4]$ (**1**) and $[Sr(p\text{BDC-}F_4)(H_2O)_4]$ (**2**) crystallize isomorphously as 2D-FCPs with hybrid inorganic-organic I^1O^1 connectivity.
- $[\{Ca(m\text{BDC-}F_4)(H_2O)_2\}\cdot H_2O]$ (**3**) and $[\{Sr(m\text{BDC-}F_4)(H_2O)_2\}\cdot H_2O]$ (**4**) crystallize isomorphously as 3D-FCPs with I^2O^1 connectivity.
- $[Ca(o\text{BDC-}F_4)(H_2O)_2]$ (**5**) and $[Sr(o\text{BDC-}F_4)(H_2O)_2]$ (**6**) crystallize isomorphously. The latter is a 2D-CP with I^1O^1 connectivity.
- The new materials are thermally stable up to 300 ˚C. The hydrated samples exhibit small surface areas which increase after thermal treatment.

5.1.1. Mechanochemical Synthesis

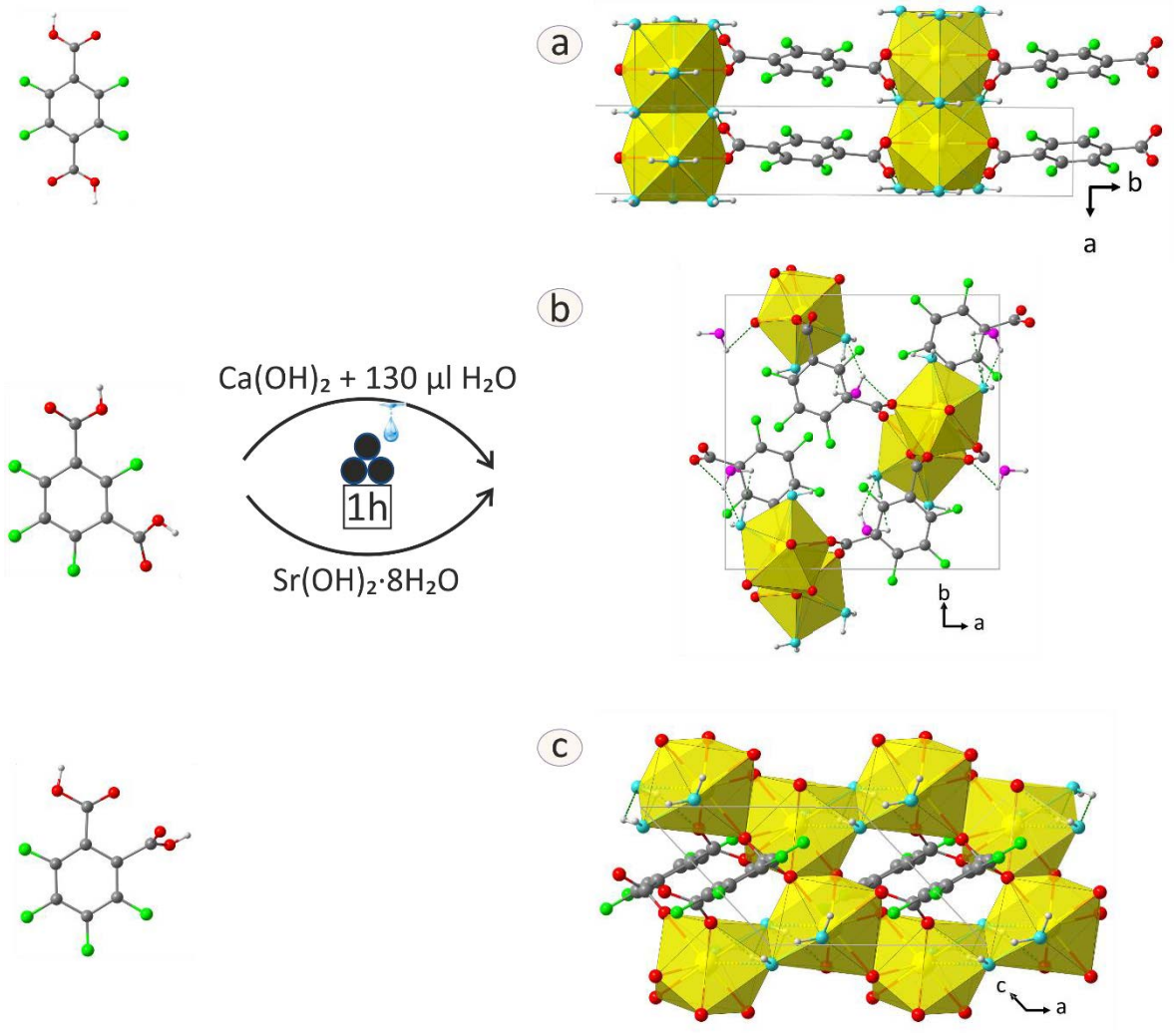

Figure 5.1: The mechanochemical synthesis and isomorphic structures of Ca- and Sr-FCPs (M^{II} = Ca, Sr) based on H_2*p*BDC-F_4, H_2*m*BDC-F_4, and H_2*o*BDC-F_4 respectively. The best results were achieved by milling an organic linker and $Ca(OH)_2$ after adding 130 µl H_2O or milling an organic linker and $Sr(OH)_2{\cdot}8H_2O$. The molar ratio between organic and inorganic precursors was maintained as 1:1. The milling time was 1h for all reactions. (a) [M^{II}(*p*BDC-F_4)$(H_2O)_4$] (**1,2**). (b) [{M^{II}(*m*BDC-F_4)$(H_2O)_2$}·H_2O] (**3,4**). (c) [Sr(*o*BDC-F_4)$(H_2O)_2$] (**6**). **Color code*: Metal (yellow), carbon (grey), carboxyl-oxygen (red), Metal-bound water-oxygen (aqua), cocrystallized water-oxygen (pink), fluorine (bright green), and hydrogen (light grey). Hydrogen bonds are represented as green dashed lines.

For a given metal cation, the mechanochemical reactions led to the formation of the same powder product regardless of the variation of the water content of the inorganic precursors (metal hydroxides with different water content in the crystal structure or by adding a small amount of water) as shown in **Scheme 4.1**. For example, **Figure A.3**a shows the recorded

PXRD patterns of the same compound [Ca(*o*BDC-F_4)(H_2O)$_2$] (**5**) obtained by grinding $Ca(OH)_2$ and H_2*o*BDC-F_4 after adding a small amount of water for 30 min, 1h, and 4h. In the absence of water, compound **5** was formed by milling a powder mixture of $Ca(OH)_2$ and H_2*o*BDC-F_4 for 4h. [Sr(*o*BDC-F_4)(H_2O)$_2$] (**6**) was obtained by milling H_2*o*BDC-F_4 and $Sr(OH)_2{\cdot}8H_2O$, $Sr(OH)_2$ + 130 µl H_2O, or $Sr(OH)_2$. In the latter reaction, the milling time was extended to 4h to compensate for the absence of water necessary for the formation of the final crystalline product (**Figure A.3b**).

Due to the implementations of water into the crystal structures, increasing the water content of the inorganic precursors reduces the milling time and also improves the crystallinity of the final product. For Ca-FCPs, the best crystalline products were obtained by adding a small amount of water to $Ca(OH)_2$ (**Figure 5.1**). For Sr-based FCPs, Sr-hydroxide octahydrate is the preferred reactant (internal water from the crystal structure of the inorganic precursor) rather than adding water to the reactants (external water).[87,88,90] These results are different from work on benzene-dicarboxylate systems.[83,84] For instance, the milling of H_2*p*BDC with $Sr(OH)_2$ led to the formation of strontium terephthalate monohydrate, while $Sr(OH)_2{\cdot}8H_2O$ as inorganic precursor formed strontium terephthalate trihydrate.[83]

5.1.2. Crystal Structures

Starting from the PXRD patterns, the determinations of the new structures followed by the Rietveld refinements were performed. The PXRD pattern of compound **5** was successfully refined using the *LeBail* method. The results of the refinements are shown in **Figure 5.2** indicating a good agreement between the simulated and measured powder XRD patterns. The indexing of the PXRD patterns was possible with the lattice constants and unit cell parameters given in **Table 5.1**. The only differences between every two isomorphic compounds in the unit cell parameters resulted from the small difference in the average size between Ca^{2+}- and Sr^{2+}-cations in their coordination to a respective ligand.

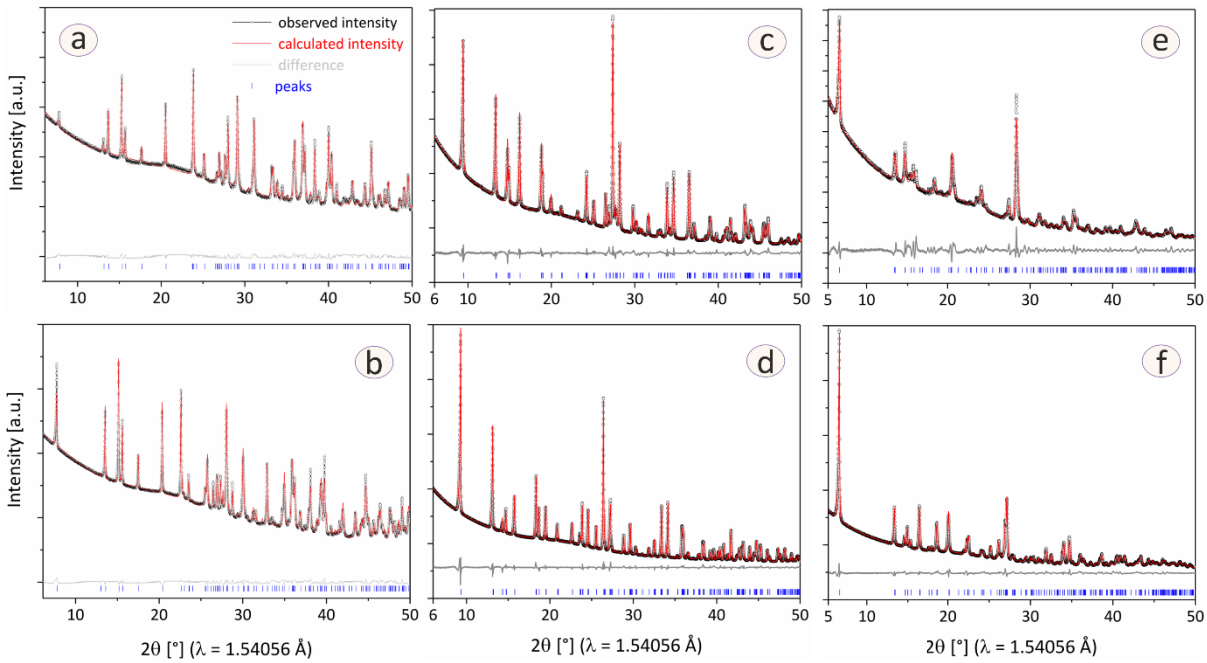

Figure 5.2: Rietveld refinements for the crystal structures of (a) [Ca(*p*BDC-F_4)$(H_2O)_4$] (**1**), (b) [Sr(*p*BDC-F_4)$(H_2O)_4$ (**2**), (c) [{Ca(*m*BDC-F_4)$(H_2O)_2$}·H_2O] (**3**), (d) [{Sr(*m*BDC-F_4)$(H_2O)_2$}·H_2O] (**4**), and (f) [Sr(*o*BDC-F_4)$(H_2O)_2$] (**6**). The *LeBail* refinement was performed for the PXRD data of (e) [Ca(*o*BDC-F_4)$(H_2O)_2$] (**5**). The R-values are given in **Table 5.1**. Scattered X-ray intensity for [M^{II}(BDC-F_4)$(H_2O)_n$] at ambient conditions as a function of diffraction angle 2θ. The observed pattern (black circles), the best fit profile (red line), the reflection- positions (blue tick marks), and the difference curve (grey line) between observed and calculated profiles are shown.

[M^{II}(*p*BDC-F_4)$(H_2O)_4$] (1,2): The asymmetric unit is composed of one M^{II}-ion, one organic linker, and four water molecules. The coordination polyhedron $M^{II}O_9$ comprises two carboxylate oxygen atoms from two monodentate *p*BDC-F_4^{2-} anions and seven water-oxygen atoms (**Figure 5.3a**). The $M^{II}O_9$ polyhedra are connected via common faces to adjacent $M^{II}O_9$ polyhedra resulting in a chain structure. These chains are connected by *p*BDC-F_4^{2-} anions to form layers of M^{II}-tetrafluoroterephthalate units wherein, the M^{II}-ions are linked by bidentate *p*BDC-F_4^{2-} anions. The layers are stacked parallel to the c-axis (**Figure 5.1a**). The layered six-member rings of *p*BDC-F_4^{2-} anions are stacked by weak π-π interactions along the a-axis with distances of 3.7259(1) Å in compound **1** and 3.9249(2) Å in compound **2**. Each two adjacent metal cations from two layers are bridged by three water molecules to form chains of a 2D layered framework and introducing unique polymeric chains {[M^{II}-$(H_2O)_3]_2$}$_n$. The formed chains are parallel to a-axis.[87]

[{M^{II}(*m*BDC-F_4)(H_2O)$_2$}·H_2O] (**3,4**): The asymmetric unit consists of one M^{II}-cation, one organic anion, and three water molecules. The M^{II}-ion is eight-fold coordinated (**Figure 5.3b**). The polyhedron $M^{II}O_8$ comprises six carboxylate-oxygen atoms from five *m*BDC-F_4^{2-} anions and two oxygen atoms belong to two metal-bound water molecules in terminus. The metal atoms are bridged by two carboxyl-oxygen atoms in chains. The metal chains are bridged via the organic linkers to form 3D crystal structures (**Figure 5.1b**). The presence of the cocrystallized water molecule (O5w) in addition to the oxygen anions from the organic anion (O3 and O4) and the coordinating water molecule (O6w) lead to the formation of a hydrogen bonding network (HBN).[88]

[M^{II}(*o*BDC-F_4)(H_2O)$_2$] (5,6): The similarity between Ca- and Sr-tetrafluorophthalates was confirmed by the results of the thermal analysis, MAS NMR, and ATR-IR measurements (See Sections 5.1.4 and 5.1.5). To gain better structural information, a *LeBail* refinement was performed for the measured PXRD pattern of Ca-CPs **5** starting from the lattice parameters derived from the crystal structure of Sr-tetrafluorophthalate **6**. The refinement result is shown in **Figure 5.2f** and indicates the proper agreement between the measured and simulated powder data. The lattice parameters after refinement and the derived parameters from the crystal structure of Sr-tetrafluorophthalate **6** are compared in **Table A.3** . Also, this result is consistent with the crystal structures of Ca- and Sr-FCPs based on tetrafluorobenzene-dicarboxylic acids, where both Ca- and Sr-FCPs crystallize isomorphously in their coordination with tetrafluoroterephthalic acid and tetrafluoroisophthalic acid, respectively.[87,88]

In the crystal structure of **6**, the asymmetric unit consists of one Sr^{2+}-cation, one *o*BDC-F_4^{2-} anion, and two water molecules. The Sr^{2+}-ion is coordinated by (8+1) oxygen atoms (**Figure 5.3c**) comprising six carboxylate-oxygen atoms from five *o*BDC-F_4^{2-} anions and two oxygen atoms belonging to two coordinated water molecules. The oxygen atom (O2w') lies at a longer distance respecting the Sr^{2+}-ion (Sr-O2w' = 3.183(2) Å). $SrO_{(8+1)}$ polyhedra are connected via the carboxylate oxygen atoms (O1, O2) and extend into a 1D polymeric chain along the crystallographic a-axis. The 1D polymeric chains are bridged by the organic linkers and the coordinating water molecules (O2w, O2w') and extend into a 2D polymeric chain along the crystallographic a- and c-axes. A network of hydrogen bonds between the metal-bound water molecule (O2w) and the carboxylate-oxygen atoms (O3, O4) is found

within the 2D polymeric chains. Layers of 2D chains build up the crystal structure of **6** (**Figure 5.1**).[90]

5.1.3. Coordination System and EXAFS Data

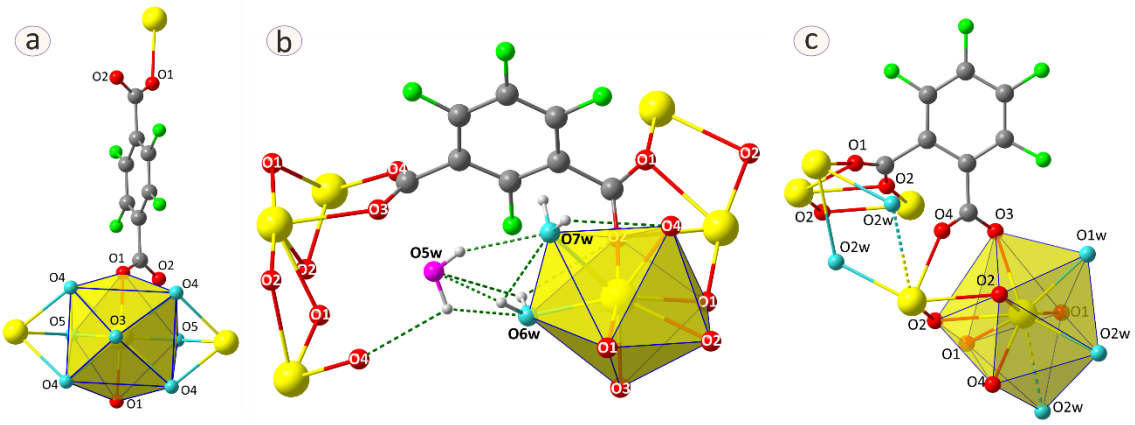

Figure 5.3: Coordination modes of organic linkers, local coordination around metals, and bridged chains in the crystal structures of compounds **1**, **2** (a), **3**, **4** (b), and **6** (c). Only one polyhedron is shown in each structure for clarity. **Color code*: Metal (yellow), carbon (grey), carboxyl-oxygen (red), coordinating water-oxygen (aqua), cocrystal water-oxygen (pink), fluorine (bright green), and hydrogen (light grey). Hydrogen bonds are represented as green dashed lines.

Tetrafluorobenzene-dicarboxylic acids vary in their coordination modes depending on the geometry of each ligand. In the *para*-isomer *p*BDC-F_4^{2-}, each carboxylate group coordinates to one metal (Ca or Sr) in a monodentate fashion (**Figure 5.3a**). *p*BDC-F_4^{2-} anions bridge the infinite 1D aqua-metallic chains to propagate the coordination system of **1** and **2** into 2D-FCPs with the connectivity of I^1O^1. In the crystal structures of **3** and **4**, each *meta*-organic linker *m*BDC-F_4^{2-} coordinates to five M^{II}-cations (**Figure 5.3b**). One carboxyl group (O1, O2) chelates one metal and bridges it to the next two M^{II}-cations forming zig-zag metal chains. The other carboxyl group (O3, O4) acts as a bidentate ligand bridging every two adjacent metals within a chain. The metal chains are bridged via the organic linkers to form 3D-FCPs (**Figure 5.1**).

In the structure of **6**, each of the *ortho* ligand anions *o*BDC-F_4^{2-} coordinates to five Sr^{2+}-ions (**Figure 5.3c**). One carboxyl group (O1, O2) chelates one Sr^{2+}-ion and bridges it to two adjacent metals. For the second carboxyl group, each oxygen atom (O3, O4) acts monodentately and indirectly connects two Sr^{2+}-ions.

The presence of water molecules and carboxylate-oxygen atoms stabilizes the crystal structures of **1**-**6** via bridging modes or building up HBNs. In **1** and **2**, water molecules bridge metals in infinite 1D-inorganic chains. In **3** and **4**, the cocrystallized water (O5w) and the metal-bound water molecules form hydrogen bridges that further stabilize the 3D-FCPs. In **6**, metal-bound water molecules are engaged in bridging the metal-organic chains and the formation of HBNs.

Longer bond lengths are found for the Sr-compounds compared to their Ca-analogs due to the larger radius of the Sr^{2+}-cation (**Table 5.1**). The $M^{II}\cdots M^{II}$ distances also vary between the isomorphic structures depending on the metal size. The $M^{II}\cdots M^{II}$ distances separated by the triple aqua bridges amount to 3.7259(1) Å in Ca-based FCP **1** and 3.9249(2) Å in Sr-based FCP **2.** The Ca···Ca distance in the structure of **3** (Ca···Ca = 3.973(3) Å) is shorter than the Sr···Sr distance in the structure of **4** (Sr···Sr distance = 4.181(3) Å). In **6**, the intermetallic distances between every two adjacent polyhedra within a 1D polymeric chain are 4.242(5) Å for each Sr···(O1, O1')···Sr separation and 4.008(6) Å for each Sr···(O2, O2')···Sr separation. The latter separations are also indirectly connected by the bidentate carboxyl group (O3, O4). These results are comparable to the reported M^{II}-O(carboxylate) bond lengths and $M^{II}\cdots M^{II}$ distances in related compounds (M = Ca, Sr).[140,147] The coordination environments and crystal data of **1-6** are summarized in **Table 5.1**. The local coordination environments around Ca^{2+}-cations (in FCPs **1**,**3**) and Sr^{2+}-cations (in FCPs **2**,**4**,**6**) were investigated by extended X-ray absorption spectroscopy (EXAFS). The fits of experimental EXAFS data along with the simulated spectra are shown in **Figure A.4**. The first coordination spheres around the respective metals are consistent with those of the determined structures.[88,90] The bond lengths within the first coordination spheres in $M^{II}O_9$ (FCPs **1**, **2**), scattering paths, and fit parameters are given in **Table A.4**.

5.1.4. Thermal Properties

The thermal behavior of each two isomorphic compounds is comparable and confirms the formation of hydrated compounds. Ca- and Sr-containing samples exhibit similar thermal stabilities.

$[M^{II}(p\text{BDC-}F_4)(H_2O)_4]$ (1,2): The thermoanalytical curves of **1** and **2** indicate two consecutive mass loss steps in both samples, which correspond to the mass release of the four water molecules. The four water molecules were released at 259 °C in the Ca-compound and at

254 °C in compound **2**. FCPs **1** and **2** are stable in air and maintain their structural integrity at ambient conditions up to 250 °C. The thermal post-treatment of the two tetrahydrate compounds **1** and **2** at 250 °C for one hour resulted in new PXRD patterns.[87]

[{M^{II}(*m*BDC-F_4)(H_2O)$_2$}·H_2O] (3,4): The thermoanalytical curves depict two consecutive steps with total mass losses of -17.3% and -14.3% that correspond to the release of three water molecules in compounds **3** (calculated: -16.3%) and **4** (calculated: -14.3%), respectively. The release of the three water molecules is complete at 276 ˚C for **3** and 285 ˚C for **4**. The fluorinated compounds **3** and **4** exhibit similar thermal stabilities (Both frameworks are stable up to 300 ˚C). The complete release of the coordinating water molecules is observed together with releasing fractions of CO_2. Also, thermal post-treatment of compounds **3** and **4** were performed based on their corresponding thermoanalytical curves. The thermal annealing of compounds **3** and **4** at 240 ˚C for 1 h resulted in products which are partially hydrated. By the thermal annealing at 280 ˚C for 2 h, the frameworks of **3** and **4** were partially decomposed.[88]

[M^{II}(*o*BDC-F_4)(H_2O)$_2$] (5,6): The thermogravimetric (TG) curves depict the expected mass loss of two equivalent water molecules in compounds **5** and **6** (**Figure A.5**) with a mass loss of about -11% (calc. -11.5%) in sample **5** and two consecutive steps with a total mass loss of -10% (calc. -10.01%) in sample **6**. The liberation of water continues along with the release of CO_2. The water-free frameworks of **5** and **6** are mainly stable between 200 and 300 °C. The PXRD patterns of the hydrated samples are compared in **Figure A.6a**. The thermally treated samples of **5** and **6** at 300 ˚C show that both samples are decomposed, and residues of CaF_2 and SrF_2 are formed (**Figure A.6b**). The immediate decomposition of samples can be rationalized by the overlap between the late release of the strongly bridged water molecules and the decomposition of the water-free framework as depicted from the thermoanalytical curves.[200] The similarity between compounds **5** and **6** is also supported by comparing MAS NMR spectra and ATR-IR spectra.

5.1.5. MAS NMR and IR Spectra

The chemical compositions and the formation of the hydrated FCPs **1**-**6** were confirmed by the carbon and hydrogen content determined by elemental analysis (**Table A.2**). The presence of water and the resemblance of each two isomorphic structures were validated by the MAS NMR spectra (**Figure 5.4**).

The ^{1}H MAS NMR spectra (**Figure 5.4a**) indicate the coordination of carboxylic groups to the metal cations in FCPs **1**-**6** by the absence of the peak at about 13 ppm which assigned to strongly bridged protons of carboxylic groups in the organic linkers (black spectra). In the black spectra, the chemical shifts around 8 ppm could indicate the formation of hydrogen bonds (O—H···O) within dimers of dicarboxylic acids.[199] The small peak at δ = 13.5 ppm in the spectrum of **1** indicates residues of H_2*p*BDC-F_4 in agreement with the ^{13}C spectrum (at δ = 114 and 165 ppm). The presences of crystal water in the FCPs are indicated by the contributions at about 5.4 ppm (FCPs **1**,**2**), 3 ppm (FCPs **3**,**4**), 5.7 and 3.2 ppm (FCPs **5**,**6**). Compared to the typical signal for water and crystal water at about 4.8 - 5 ppm, both signals in **3, 4**, and **6** are high-field shifted indicating networks of hydrogen bridges. Additional signals that belong to the bridged water are recorded at δ = 14 and 16.3 ppm in the red spectrum of **5**.

The ^{1}H→^{13}C CP MAS NMR spectra (**Figure 5.4b**) depict two carbon signals belonging to the carboxylic group at δ = 167 ppm in both FCPs **1** and **2** and the aromatic carbon atoms at δ = 119 ppm. The four positions of carbon in the ring could not be fully resolved due to their similarities, but the shape and broadness of carbon signals at δ = 119 ppm in **1** and **2** suggest that these positions are covered by the broad peak. Compared to FCP **4**, compound **3** contains higher water content indicated by the presence of many spinning sidebands in ^{1}H MAS NMR spectrum. Consequently, it was no problem to measure the ^{1}H→^{13}C CP MAS NMR spectrum for compound **3**. Instead, the direct ^{13}C MAS NMR spectrum was recorded for compound **4**. Both spectra give evidence for the existence of two different carbon sites in carboxylate groups at δ = 168 and 165 ppm (in FCPs **3**) and at δ = 169 and 165 ppm (in FCP **4**). The separations between the two chemical shifts assigned to carbon atoms in carboxylate groups are 2.8 ppm and 3.6 ppm in FCPs **3** and **4**, respectively. Such relatively high separations compared to the organic ligand (separation is 1.3 ppm) indicate the participation of carboxylic groups in the coordination system. In the spectrum of **5**, three carbon sites in the carboxylate groups appear at δ = 173, 171, and 167 ppm. Two different carbon sites in the carboxylate groups are recorded at δ = 170 ppm and at δ = 168 for **6**. Only two carbon sites in the benzene ring are identified at δ = 125 and 122 ppm for **5**. However, the four aromatic carbon sites known from the crystal structure of Sr-tetrafluorophthalate **6** are also not completely resolved since they all are fluorinated. In the spectrum of the latter, only one carbon site was identified for the aromatic carbon atom at δ = 123 ppm.

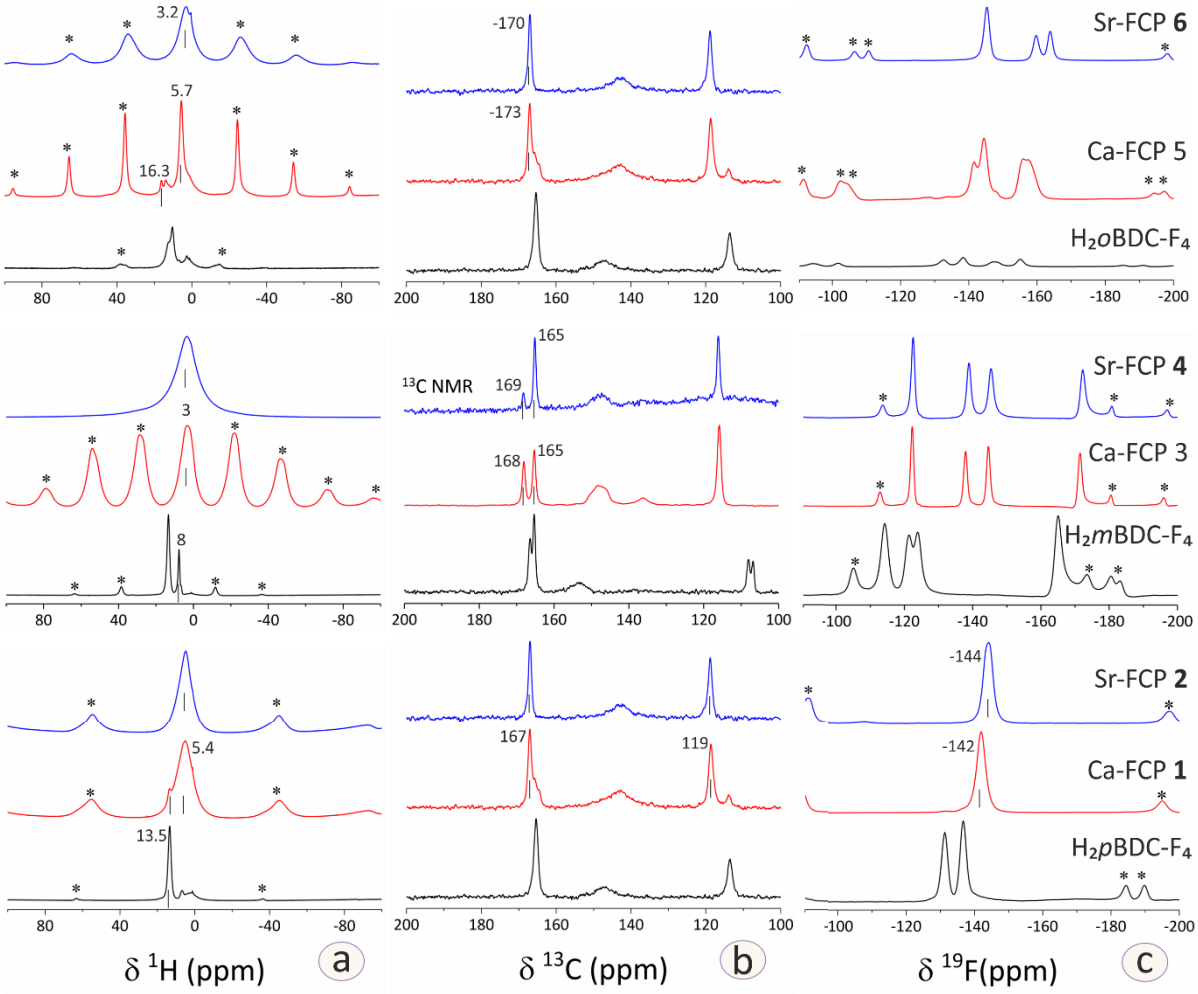

Figure 5.4: MAS NMR spectra for organic linkers: H_2*p*BDC-F_4, H_2*m*BDC-F_4, H_2*o*BDC-F_4 (black spectra), Ca-FCPs **1**, **3**, **5** (red spectra), and Sr-FCPs **2**, **4**, **6** (blue spectra). (a) ^{1}H NMR, ν_{rot} = 20 kHz (ν_{rot} = 12 KHz for H_2*o*BDC-F_4). (b) ^{1}H→^{13}C CP MAS NMR spectra, ν_{rot} = 10 kHz, contact time = 10 ms (for **4**, the direct ^{13}C MAS NMR spectrum was measured). (c) ^{19}F MAS NMR spectra, ν_{rot} = 20 kHz (ν_{rot} = 22 kHz for H_2*m*BDC-F_4 and FCPs **3** and **4**. Spinning sidebands (*).

The ^{19}F MAS NMR spectra (**Figure 5.4c**) depict signals at δ = -142 ppm (FCP **1**) and -144 (FCP **2**). The shape and broadness of the fluorine signals suggest that the two distinguishable crystallographic positions of fluorine atoms are hidden within the broad peak. Two signals at δ = -130 ppm and -136 ppm of low intensity in **1** refer to unreacted residues of H_2*p*BDC-F_4 (not visible). The similarity of ^{19}F MAS NMR spectra in both FCPs **3** and **4** indicates the resemblance of their structures. Both spectra depict four distinguishable positions of fluorine atoms in the crystal structures. In the recorded spectra of **5** and **6**, all signals are shifted compared to the organic linker (black spectrum) that depicts four distinguishable positions of fluorine atoms at δ = -133, -138, -147, and -155 ppm which are known from

the crystal structure (RefCode: BOLNAR).[181] For compound **5,** three distinguishable fluorine sites could be resolved. The fourth fluorine site, known in the crystal structure, is covered by one of the broad fluorine signals. For compound **6,** four distinguishable fluorine sites are resolved at chemical shifts of -141, -144, -156, and -157 ppm.

The FT-IR and ATR-IR spectra depicted in **Figure 5.5** and **Figure 5.6** give an overview of the chemical binding environment and allow the assignment of crystal water molecules in FCPs **1**-**6**. The fraction of broad vibration bands above 3000 cm^{-1} in the IR spectra of the formed complexes indicates the presence of water molecules. For FCP **1** (**Figure 5.5**, red spectrum), two peaks and a shoulder appear at approximately 3572 cm^{-1}, 3410 cm^{-1}, and 3192 cm^{-1}, indicating the presence of different water moieties in the sample. The broad peak at 3410 cm^{-1} results from water at the surface, whereas the small overlapped band at 3192 cm^{-1} could be assigned to contributions of coordinating water molecules. The vibration bands of water at surface appear at 3409 cm^{-1} and 3593 cm^{-1} in the IR spectrum of FCP **2** (**Figure 5.5**, blue spectrum), while the crystal water band appears at 3247 cm^{-1}.[149]

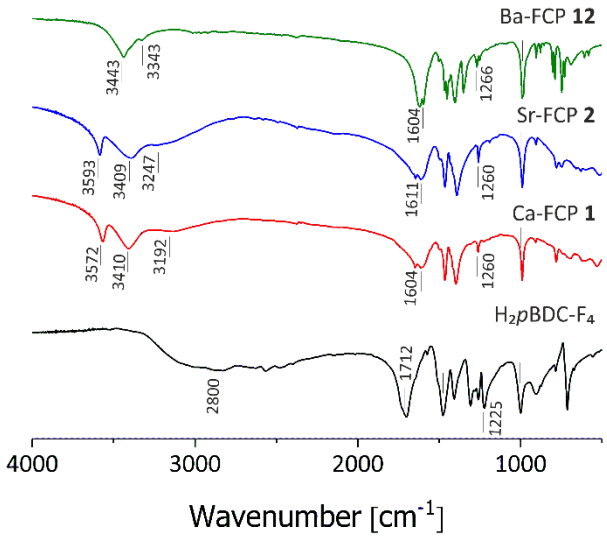

Figure 5.5: FT-IR spectra of H_2*p*BDC-F_4 (black spectrum), [Ca(*p*BDC-F_4)(H_2O)$_4$] (**1**) (red spectrum), [Sr(*p*BDC-F_4)(H_2O)$_4$] (**2**) (blue spectrum), and [Ba(*p*BDC-F_4)(H_2O)$_{0.5}$] (**12**) (green spectrum).

For FCPs **3** and **4** (**Figure 5.6a**), the broad contributions around 3429 cm^{-1} (red spectrum) and around 3413 cm^{-1} (blue spectrum) and the vibrational band at 3684 cm^{-1} in both spectra are mainly due to the coordinating water molecules and the formation of HBNs along the crystal structure. Similar to Sr-tetrafluorophthalate **6** (**Figure 5.6b**, blue spectrum), the contribution above 3000 cm^{-1} in the spectrum of **5** (red spectrum) are attributed to the presence of water.[148] The contribution around 3398 cm^{-1} is assigned to the HBNs within the crystal lattices of **5** and **6**.

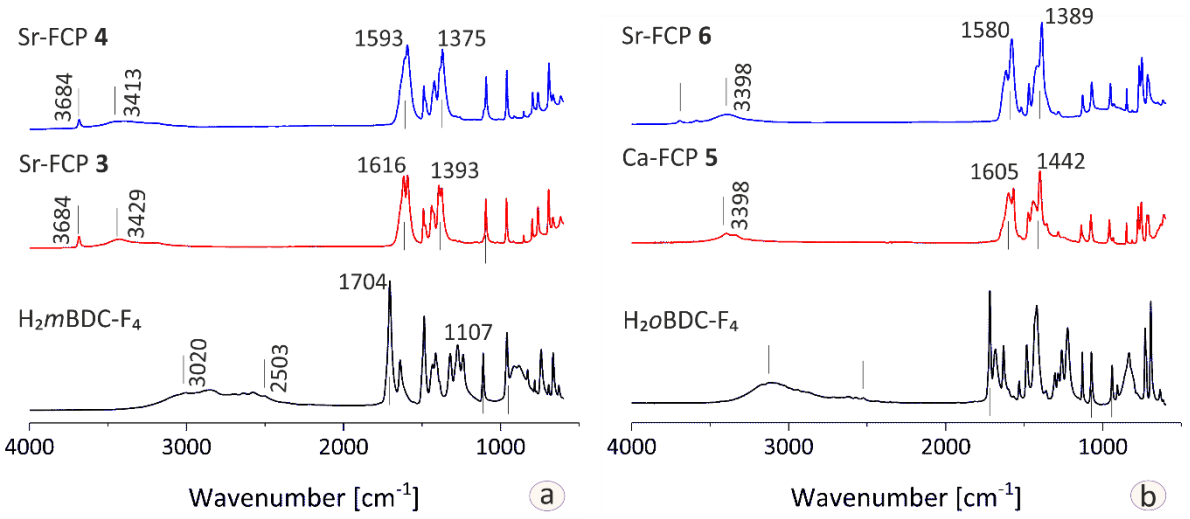

Figure 5.6: ATR spectra of organic linkers, Ca-FCPs, and Sr-FCPs. (a) H_2*m*BDC-F_4 (black spectrum), compound **3** (red spectrum), compound **4** (blue spectrum). (b) H_2*o*BDC-F_4 (black spectrum), compound **5** (red spectrum), compound **6** (blue spectrum).

The IR spectra show the expected bands resulting from the coordination of calcium and strontium cations to the carboxylate oxygen atoms in BDC-F_4^{2-} anions. For FCPs **1** and **2**, the conversion of protonated carboxylic groups of H_2*p*BDC-F_4 leads to the absence of the vibration at 2800 cm^{-1} and at 1712 cm^{-1} in the formed [M^{II}(*p*BDC-F_4)(H_2O)$_4$] samples. The absorption at 1225 cm^{-1} (C-O stretching and OH deformation of COOH) is shifted to weak vibration bands at 1260 cm^{-1} in both compounds **1** and **2**. The vibrations of the deprotonated carboxylic groups appear at 1604 cm^{-1} and 1611 cm^{-1} in **1** and **2**, respectively. The typical band of the deformation vibration of water, which usually appears at ~ 1600 cm^{-1},[201,202] could be covered by the strong vibration of carboxylate at the vibration range between 1604 and 1611 cm^{-1}. The vibration band assigned to the C-F stretching in the coordinated tetrafluoroterephthalate is shifted to 994 cm^{-1} in both compounds **1** and **2**. In the spectra of FCPs **3** and **4,** the vibrational bands assigned to the carboxylate stretching appear at 1616 cm^{-1} and 1593 cm^{-1} for asymmetric stretching, and at 1393 cm^{-1} and 1375 cm^{-1} for symmetric stretching. The separation (Δ_{a-s}) between asymmetric (ν_{as}) and symmetric (ν_s) stretching of carboxylate groups is about 223 cm^{-1} in **3** and **4**, respectively. For compound **5**, the main vibrational band assigned to the carboxylate stretching appear at 1605 and 1570 cm^{-1} for asymmetric stretching, and at 1442 and 1400 cm^{-1} for symmetric stretching. The separation (Δ_{a-s}) is about 170 cm^{-1}. For FCP **6**, the carboxylate stretching appears at 1580 cm^{-1} for asymmetric stretching, and at 1389 cm^{-1} for symmetric stretching (black spectrum).

The separation (Δ_{a-s}) is about 191 cm^{-1}. The relatively high separations (Δ_{a-s}) between asymmetric (ν_{as}) and symmetric (ν_s) stretching of carboxylate groups in FCPs **1**-**6** are attributed to the chelating and bridging modes of carboxylate groups.[73,203]

5.1.6. Sorption Properties and Morphology

The hydrated samples of compounds **1**-**6** exhibit small surface areas which increase in the thermally treated samples as a result of the release of crystal water.[87,88] For example, the hydrated samples of **3** and **4** show surface areas of 5.4 m^2/g and 3.1 m^2/g, respectively. Even after pretreatment at 200 ˚C, the BET surface areas remain unchanged. At 240 ˚C, the BET surface areas of **3** and **4** increase to 12.6 m^2/g and 13.6 m^2/g, respectively. The BET results of samples as-synthesized and after thermal treatments are given in **Table 5.4**. The SEM images shown in **Figure 5.7** depict similar morphologies of plate-like structures for samples of **1**-**6**.

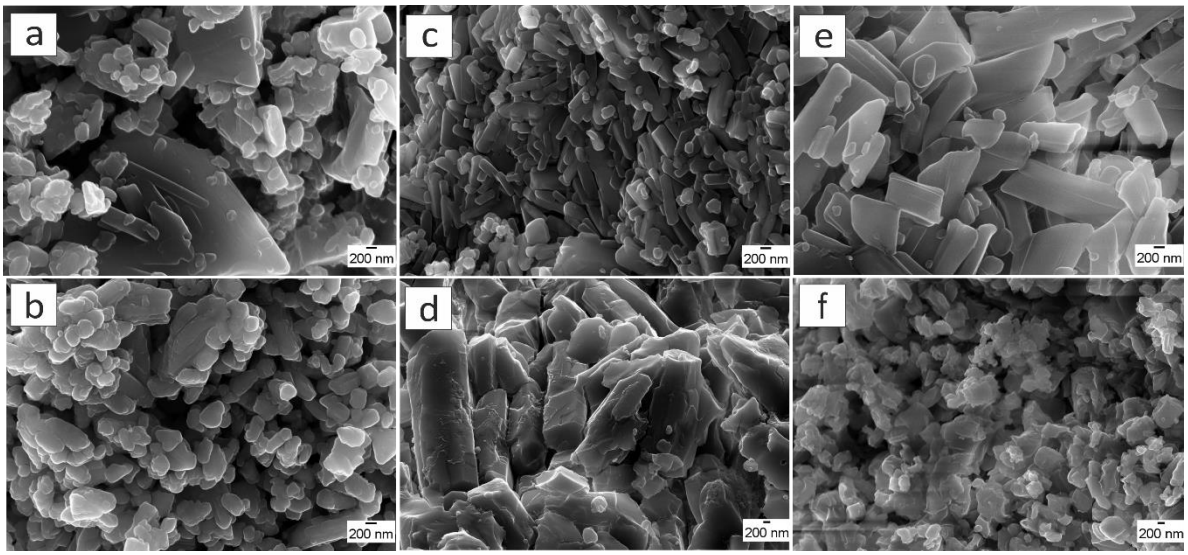

Figure 5.7: SEM images for samples of Ca- and Sr-FCPs **1**-**6**. (a) [Ca(*p*BDC-F_4)(H_2O)$_4$] (**1**). (b) [Sr(*p*BDC-F_4)(H_2O)$_4$] (**2**). (c) [{Ca(*m*BDC-F_4)(H_2O)$_2$}·H_2O] (**3**). (d) [{Sr(*m*BDC-F_4)(H_2O)$_2$}·H_2O] (**4**). (e) [Ca(*o*BDC-F_4)(H_2O)$_2$] (**5**). (f) [Sr(*o*BDC-F_4)(H_2O)$_2$] (**6**).

5.1.7. Comparison and Conclusion

New fluorinated coordination polymers (FCPs) were synthesized by milling powders of Ca- and Sr-hydroxides with tetrafluorobenzene-dicarboxylic acids (H_2BDC-F_4) in a stoichiometric ratio of 1:1 in a planetary mill (**Figure 5.1**). The structures of the obtained polycrystalline powders were solved *ab initio* from PXRD data and subsequently refined using the Rietveld

refinement (structural properties of compound **5** was confirmed by the *LeBail* refinement). The variations in water content of the inorganic precursors do not influence the number of coordinated water molecules in the final products. The latter finding contrasts with the mechanochemical synthesis of alkaline earth metal-(benzene-dicarboxylate) compounds. In the latter, the number of coordinating water molecules of the final products was influenced by the water content of inorganic samples. However, the water contents of the reactants affect at least the crystallinity of the newly formed FCPs, which increased by adding a small fraction of water (130 µL) to the $Ca(OH)_2$ or by using strontium hydroxide octahydrates. Ca- and Sr-based FCPs of a given ligand crystallize isomorphously and exhibit similar thermal and sorption properties. Along with these findings, the water content of the reactants has a strong influence on the necessary milling time. The lower the water content, the longer is the required milling time.

Topologies and geometries of the perfluorinated organic precursors ($H_2BDC\text{-}F_4$) strongly influence the coordination environments in the resulting FCPs **1**-**6**. The *para*-isomer *p*$BDC\text{-}F_4^{2-}$ reacts as a bidentate ligand (each carboxyl is a monodentate) and links the aqua-metallic chains to form 2D-layered structures of [Ca(*p*$BDC\text{-}F_4$)$(H_2O)_4$] (**1**) and [Sr(*p*$BDC\text{-}F_4$)$(H_2O)_4$] (**2**). In the crystal structures of [{Ca(*m*$BDC\text{-}F_4$)$(H_2O)_2$}·H_2O] (**3**) and [{Sr(*m*$BDC\text{-}F_4$)$(H_2O)_2$}·H_2O] (**4**), the inorganic chains are crosslinked by the *meta*-anions *m*$BDC\text{-}F_4^{2-}$ to build up 3D-FCPs. Each *m*$BDC\text{-}F_4^{2-}$ chelate one metal and bridge another four. The *ortho*-Isomer *o*$BDC\text{-}F_4^{2-}$ exhibits a coordination mode similar to *meta*-anion. The geometry of the ortho anions only allows bridging 1D-chains to keep the two-dimensionality of [Sr(*o*$BDC\text{-}F_4$)$(H_2O)_2$] (**6**).

The determined structures were supported by fitting the simulated and measured EXAFS spectra. The hydrated compounds exhibit small surface areas that were relatively increased after thermal treatments. The thermal stabilities of these compounds are very similar. The release of crystal water molecules is around 250 °C in **1** and **2**, 280 °C in **3** and **4**, 290 °C in **5** and **6**. All the compounds begin to decompose around 300 °C. Mechanochemical synthesis, structures, and properties of the fluorine-free counterparts are discussed in **Section 5.2** and followed by the comparison of the behavior and local coordination of alkaline earth metals in their coordination to the perfluorinated and fluorine-free organic ligands (**Section 5.3**).

Table 5.1: Coordination environments, refined parameters, and crystal data derived from the crystal structures of compounds **1**, **2**, **3**, **4**, **6**, and **12**.

	[Ca(*p*BDC-F_4)(H_2O)$_4$] (**1**)	[Sr(*p*BDC-F_4)(H_2O)$_4$] (**2**)	[{Ca(*m*BDC-F_4)(H_2O)$_2$}·H_2O] (**3**)	[{Sr(*m*BDC-F_4)(H_2O)$_2$}·H_2O] (**4**)	[Sr(*o*BDC-F_4)(H_2O)$_2$] (**6**)	[Ba(*p*BDC-F_4)(H_2O)$_{0.5}$] (**12**)
C.N.	CaO_9	SrO_9	CaO_8	SrO_8	$SrO_{(8+1)}$	BaO_8F_2
Coordinating oxygen (carboxyl)	2 (2 linkers)		6O (5 Linkers)		6O (5 Linkers)	7 (6 Linkers)
Coordinating oxygen (water)	7 (1 terminal, 6 bridging)		2 terminals		2 (O1w, O2w)	1 (bridging)
Cocrystal water	-	-	1 (O5w)		-	-
Coordination mode (Ligand)	2 metals (bidentate)		5 metals (chelate, bridge)		5 metals (chelate, bridge)	6 metals (chelate, bridge)
M-O(carboxylate) (Å)	2.6001(1)	2.6191(1)	2.266(8) - 2.619(8)	2.389(9) - 2.767(1)	2.426(2) - 2.774(1)	2.6966(1) - 2.9703(1)
M-O (water) (Å)	2.3879(1) - 2.5714(1)	2.4118(1) - 2.6472(1)	2.389(6) - 2.581(6)	2.570(9) - 2.690(8)	2.688(1) - 2.732(1), 3.183(2)	2.9052(1)
M ··· F (Å)	4.881(1)	4.924(2)	4.808(1)	4.593(1)	4.803(2)	2.975(2), 3.107(3)
M-(bridged)-M (chain) (Å)			3.973(4)	4.181(3)	4.242(5), 4.008(6), 5.063(5)	4.372(5)
M-(BDC-F_4)-M (Å)	12.5377(2)	12.6252(5)	8.313(2)	8.386(1)	5.063(5)	8.150(5)
π-π distance	3.726(1)	3.925(2)	6.706(2)	6.954(1)	4.879(2)	3.410(7)
O-M-O angle (°)	63.782(1) - 145.274(1)	67.388(1) - 145.991(1)	51.672(2) – 171.690(3)	48.932(2) – 170.452(3)	49.434(4) - 150.287(7)	62.831(1) – 156.620(9)
M-M-M angle (°)	180	180	51.672(2) – 171.690(3)	48.932(2) – 170.452(3)	80.987(4), 116.391(7), 126.068(6)	109.280(1)
Dimensionality	2D (I^1O^1)		3D (I^2O^1)		2D (I^1O^1)	3D (I^2O^1)
Cell parameters						
Formula sum	$Ca_2(C_8F_4O_4)_2(H_2O)_8$	$Sr_2(C_8F_4O_4)_2(H_2O)_8$	$Ca_4(C_8F_4O_4)_4(H_2O)_{12}$	$Sr_4(C_8F_4O_4)_4(H_2O)_{12}$	$Sr_4(C_8F_4O_4)_4(H_2O)_8$	$Ba_8(C_8F_4O_4)_8(H_2O)_4$
Formula weight (g/mol)	680.31	775.394	1296.612	1486.780	1422.782	3059.292
Cell volume (Å^3)	563.07(3)	602.85	1296.612	1486.780	1089.58(12)	1757.766(16)
Crystal system	monoclinic		Orthorhombic		monoclinic	monoclinic
Space group	P 2_1/m (11)		P $2_12_12_1$ (19)		P 1 2_1 /c 1 (14)	C 1 2/c 1 (15)

	[Ca(*p*BDC-F_4)(H_2O)$_4$] (**1**)	[Sr(*p*BDC-F_4)(H_2O)$_4$] (**2**)	[{Ca(*m*BDC-F_4)(H_2O)$_2$}·H_2O] (**3**)	[{Sr(*m*BDC-F_4)(H_2O)$_2$}·H_2O] (**4**)	[Sr(*o*BDC-F_4)(H_2O)$_2$] (**6**)	[Ba(*p*BDC-F_4)(H_2O)$_{0.5}$] (**12**)
a (Å)	3.7259(1)	3.9249(2)	13.2223(7)	13.4135(4)	8.101(5)	12.61221(7)
b (Å)	22.4805(5)	22.6208(11)	13.1667(7)	13.3578(4)	26.399(12)	7.16626(4)
c (Å)	6.7332(2)	6.8030(3)	6.7057(4)	6.9538(2)	6.989(4)	19.84594(10)
β (°)	93.5435(19)	93.5435	90	90	133.198(1)	101.4918(3)
Cell ratio						
a/b	0.1657	0.1735	1.0042	1.0042	0.307	1.760
b/c	3.3388	3.3251	1.9635	1.9209	3.777	0.3611
c/a	1.8071	1.7333	0.5072	0.5184	0.863	1.5735
Z	2	2	4	4	4	8
Density, calc. (g/cm^3)	2.01	2.14	1.844	1.981	2.168	2.89
Refinement parameters						
R_{wp}	5.07	6.44	3.01	2.68	2.99	10.26
R_p	3.88	4.19	1.89	1.70	2.08	7.94
R_{Bragg}			2.123	1.832	1.558	2.968
GOF			4.60	4.16	3.64	1.22
PXRD measurements						
Instrument/ BeamLine	D8 Discover					Rapid Access Beamline
Calibration	Si standard powder					
λ (Å)	1.54056 (Cu-$K_{\alpha1}$)					0.825862(10)
2θ range (°)	5 – 65					0 - 150
step size	0.009°, 5 s per step					-
Collection time	35 h					30 min
Deposition in CSD						
CCDC	1443540	1443539	1535203	1535204	1562229	
Refcode	GONTEK01	EJEPEQ			YECVUA	

5.2. Ca- and Sr-(Benzene-Dicarboxylates): $[M^{II}(BDC)(H_2O)_n]$

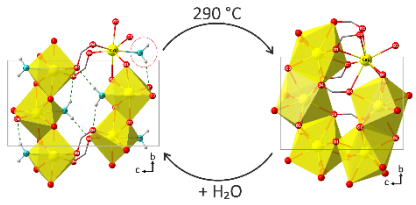

i. A. Al-Terkawi, G. Scholz, C. Prinz, A. Zimathies, F. Emmerling, E. Kemnitz. *CrystEngComm.* **2018**, *20*, 946-961.

ii. A. Al-Terkawi, G. Scholz, F. Emmerling, E. Kemnitz, *Dalton Trans.* **2017**, *46*, 12574–12587.

iii. A. Al-Terkawi, G. Scholz, F. Emmerling, E. Kemnitz. (*Dalton Trans. accepted*)

Scientific Aspects:

- Ca- and Sr-CPs based on the isomers of benzene-dicarboxylic acid were mechanochemically synthesized.
- Variation in the water content of inorganic sources can affect the coordination systems of final products.
- Ca-based CPs obtained by milling are similar to reported compounds obtained via solvothermal treatments.
- Milling of $Sr(OH)_2{\cdot}8H_2O$ with benzene-dicarboxylic acids resulted in new compounds.
- [Ca(*p*BDC)$(H_2O)_3$] (**7**) and [Sr(*p*BDC)$(H_2O)_3$][84] crystallize isomorphously as 1D-CPs with I^1O^0 connectivity.
- [Ca(*m*BDC)$(H_2O)_{3.4}$] (**8**) and [Sr(*m*BDC)$(H_2O)_{3.4}$] (**9**) crystallize isomorphously as 1D-CPs (I^1O^0).
- [Ca(*o*BDC)$(H_2O)_1$] (**10**) crystallizes as a 2D-CP with a hybrid inorganic-organic I^1O^1 connectivity.
- [Ca(*o*BDC)] (**10-H_2O**), obtained after the thermal post-treatment of **10** in a reversible phase transition process, crystallizes as a 2D-CP (I^2O^0).
- [{Sr(*o*BDC)$(H_2O)_2$}$\cdot H_2O$] (**11**) crystallizes as a 2D-CP (I^2O^0).
- The new materials are thermally stable up to 400 ˚C. The hydrated samples exhibit small specific surfaces which can slightly increase after thermal treatment.

5.2.1. Mechanochemical Synthesis

Ca- and Sr-CPs based on benzene-dicarboxylic systems (H_2BDC) were obtained by milling the metal hydroxides with the respective ligand. In contrast to their fluorinated counterparts (FCPs), the variations in water content of the inorganic samples mainly influence the final coordination of systems of the resulting fluorine-free CPs.

The mechanochemical synthesis of the hydrated [Ca(*p*BDC)$(H_2O)_3$] (**7**) and [Sr(*p*BDC)$(H_2O)_3$] were described elsewhere.[83] Ca-CP **7** is similar to reported structures via solvothermal treatments.[146,149–151] [Ca(*m*BDC)$(H_2O)_{3.4}$] (**8**) was prepared by milling the organic precursor isophthalic acid (H_2*m*BDC) with $Ca(OH)_2$ and a small amount of water for 1 h. In the absence of water, a poor crystalline product was formed by milling of the powder mixture for 4 h.[204] The structure of **9** is similar to the reported structure by Yu *et al.* and by Dale *et al.* and can be identified for simplicity as [Ca(*m*BDC)$(H_2O)_{3.4}$].[147,148] More precisely, a composition of [{$Ca_{2.5}$(*m*BDC)$_{2.5}(H_2O)_{4.5}$}·$4H_2O$] can be assigned. Both reported structures were synthesized via hydrothermal treatments. [Sr(*m*BDC)$(H_2O)_{3.4}$] (**9**) was formed by milling $Sr(OH)_2·8H_2O$ and H_2*m*BDC. The milling time was varied between 15 min, 1 h, and 4h. The comparison between the PXRD patterns indicates the formation of the same compound regardless of the variations of milling time as shown in **Figure A.7** (PXRD patterns: 9 and 9b). Milling $Sr(OH)_2$ + 130 µl H_2O with H_2*m*BDC for 15 min did not lead to the formation of a new compound. By milling the latter powder mixture for 1h, a new compound was formed (PXRD pattern: 9d). Without adding water to the reaction mixture, an amorphous product was formed.[200] These findings agree with the results from the mechanochemical reaction of Sr-hydroxides with terephthalic acid.[83] Here, the variation of the water content in the inorganic precursors influence the crystallinity and the coordination environments of the final products. [Ca(*o*BDC)(H_2O)] (**10**) was synthesized by milling phthalic acid (H_2*o*BDC) with $Ca(OH)_2$ and 130 µL H_2O. The milling time was varied between 30 min, 1h, or 4 h leading to the formation of the same compound **10**. In the absence of water, compound **10** was formed after milling the powder mixture for 4 h.[204] The structure of compound **10** is similar to the reported compounds via solvothermal treatment by Gupta *et al.*, Schuckmann *et al.*, and Zhang *et al*.[145,146] [{Sr(*o*BDC)$(H_2O)_2$}·H_2O] (**11**) was synthesized by milling Sr-hydroxide octahydrate $Sr(OH)_2·8H_2O$ and phthalic acid H_2*o*BDC. Two more products were obtained by milling $Sr(OH)_2$

with H_2*o*BDC for 1 h after adding a small amount of water or by milling the same powder mixture for 4h without adding water.[90]

5.2.2. Crystal Structures

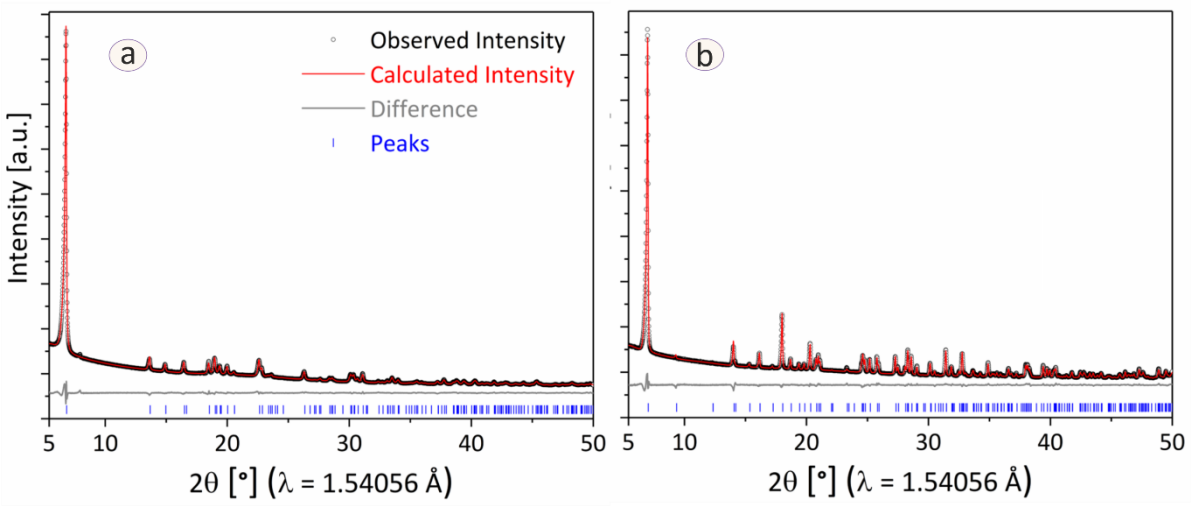

Figure 5.8: Rietveld refinements for the crystal structure of (a) [Ca(*o*BDC)] (**10-H_2O**) and (b) [{Sr(*o*BDC)$(H_2O)_2$}·H_2O] (**11**).

The hydrated Ca-CPs **7**, **8**, and **9** were successfully refined via the Rietveld method (**Figure A.8a**,**b**,**d**). The new crystal structures of dehydrated Ca-phthalate (**10-H_2O**) and hydrated Sr-phthalate **11** were determined from PXRD data and subsequently refined using the Rietveld method (**Figure 5.8**). The isomorphism of Ca- and Sr-isophthalates was confirmed by performing the *LeBail* refinement for the PXRD pattern of Sr-isophthalate (**Figure A.8c**). The lattices parameters of [Sr(*m*BDC)$(H_2O)_{3.4}$] (**9**) after refinement are compared to those derived from Ca-isophthalate in **Table A.5**.[200] The coordination environment and crystal data derived from the crystal structures of **7**, **8**, **10**, and **10-H_2O** are summarized in **Table 5.2**.

[Ca(*p*BDC)$(H_2O)_3$] (7): Both compounds of Ca- and Sr-terephthalates obtained by milling crystallize isomorphously.[84] In [Ca(*p*BDC)$(H_2O)_3$], the asymmetric unit consists of one Ca^{2+}-cation, one *p*BDC^{2-} anion, and three water molecules. Ca^{2+}-ion is surrounded by eight oxygen atoms comprising four carboxylate oxygen atoms from three organic anions, two bridging water-oxygen atoms, and two terminal water molecules (**Figure 5.13**a). Each CaO_8 polyhedron shares three edges (O1,O2,O2w) with each neighboring CaO_8 polyhedrons and extending the inorganic connections into 1D polymeric chains along the crystallographic c-axis (**Figure 5.9**b). The Ca-(O1,O2,O2w)-Ca unit is 3.640(1) Å. The 1D chains are linked to

a 3D-array by a hydrogen-bonding network including the non-coordinating carboxyl groups (O3,O4) and the water molecules in addition to the aromatic π–π stacking. The structures of Sr-terephthalate, dehydrated Ca- and Sr-terephthalates were described in the reported work by Scholz *et al.* and Mazaj *et al*.[84,152] In the crystal structures of [Ca(*p*BDC)] and [Sr(*p*BDC)], $M^{II}O_6$ are arranged in infinite chains that are bridged via *p*BDC^{2-} anions to form 3D-CPs (**Figure 5.9c** and **Figure 5.13b**).[84,152]

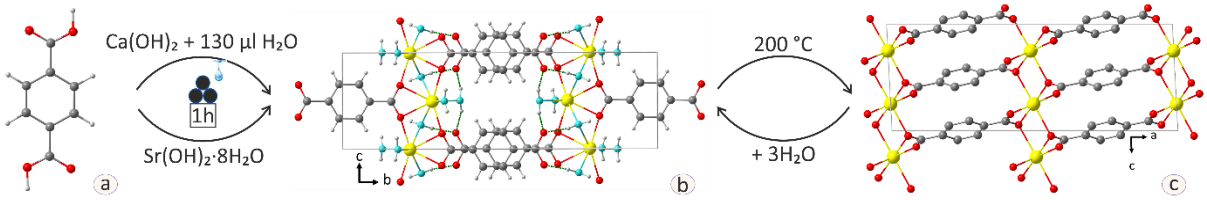

Figure 5.9: Mechanochemical synthesis and isomorphic structures of [M^{II}(*p*BDC)(H_2O)$_3$] and [M^{II}(*p*BDC)] (M^{II}=Ca or Sr). (a) Ca-CP was obtained by milling H_2*p*BDC and $Ca(OH)_2$ after adding 130 µl H_2O. Sr-CP was produced by grinding H_2*p*BDC and $Sr(OH)_2{\cdot}8H_2O$ (Scholz *et al.*). The molar ratio between organic and inorganic precursors was maintained as 1:1. Milling time was 1h for all reactions. (b) The crystal structures of [M^{II}(*p*BDC)(H_2O)$_3$]. (c) The hydrated samples transform into new dehydrated phases by thermal annealing at 200 °C. **Color code*: Metal (yellow), carbon (grey), carboxyl-oxygen (red), coordinating water-oxygen (aqua), and hydrogen (light grey). Hydrogen bonds are represented as green dashed lines.

[Ca(*m*BDC)(H_2O)$_{3.4}$] (8): The asymmetric unit contains three independent Ca^{2+} positions (Ca1 and Ca2 are in general positions while Ca3 lies on a two-fold axis). The water molecules comprise four Ca-bound water molecules, a bridging water molecule, and four cocrystallized water molecules. Ca1 has a coordination number of eight comprising six carboxylate oxygen atoms, and two terminal coordinating water molecules (**Figure 5.13c**). Like Ca1, Ca2 is eight-fold coordinated except for one of the two coordinating water molecules that bridge Ca2 to the next metal center Ca3. The third cation Ca3 is nine-fold coordinated with six carboxylate oxygen atoms, one water molecule in terminus, and two bridging water molecules in the coordination sphere. The carboxylate oxygen atoms and the water-oxygen atoms bridge the metal centers and subsequently lead to the formation of 1D helical strands (**Figure 5.10b**). The Helices are connected via extensive hydrogen-bonding network (HBN) that originates between the metal-coordinating water molecules, water molecules of crystallization, and carboxyl oxygen atoms and form 3D arrays. The Ca···Ca distances are 3.977(1) Å, 3.8747(2) Å, 3.6414(1) Å for the units Ca1-(O1,O1')-Ca1, Ca1-(O6,O7)-Ca2, and

Ca2-(O8,O12,O11)-Ca3, respectively. The Ca-O(carboxylate) bond lengths range from 2.3626(1) – 2.6567(1) Å. The Ca-O(aqua) distances range between 2.3446(1) and 2.6373(1) Å.

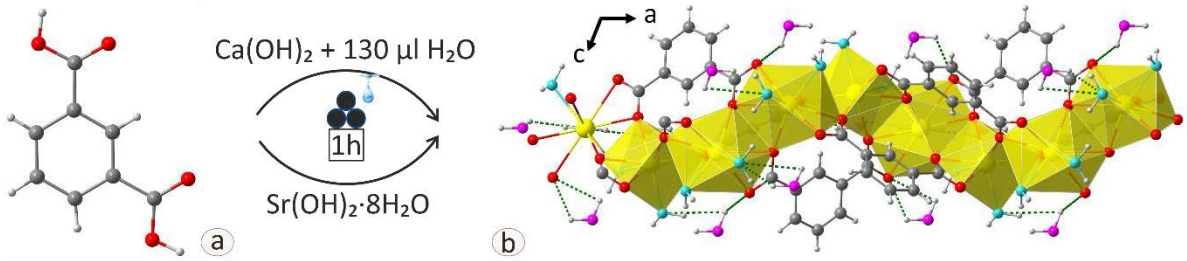

Figure 5.10: Mechanochemical synthesis and isomorphic structures of $[M^{II}(m\text{BDC})(H_2O)_{3.4}]$ (M^{II}=Ca or Sr). The crystal structures of $[Ca(m\text{BDC})(H_2O)_{3.4}]$ consists of 1D-helical chains which are connected via intensive hydrogen bonds. **Color code*: Metal (yellow), carbon (grey), carboxyl-oxygen (red), coordinating water-oxygen (aqua), cocrystal water-oxygen (pink), and hydrogen (light grey). Hydrogen bonds are represented as green dashed lines.

[Ca(*o*BDC)(H₂O)] (10): The asymmetric unit consists of one calcium ion, one $o\text{BDC}^{2-}$, and one water molecule. The Ca^{2+}-ion is seven-fold coordinated (**Figure 5.13d**) comprising six carboxylate oxygen atoms from four organic anions and one water molecule in terminus.

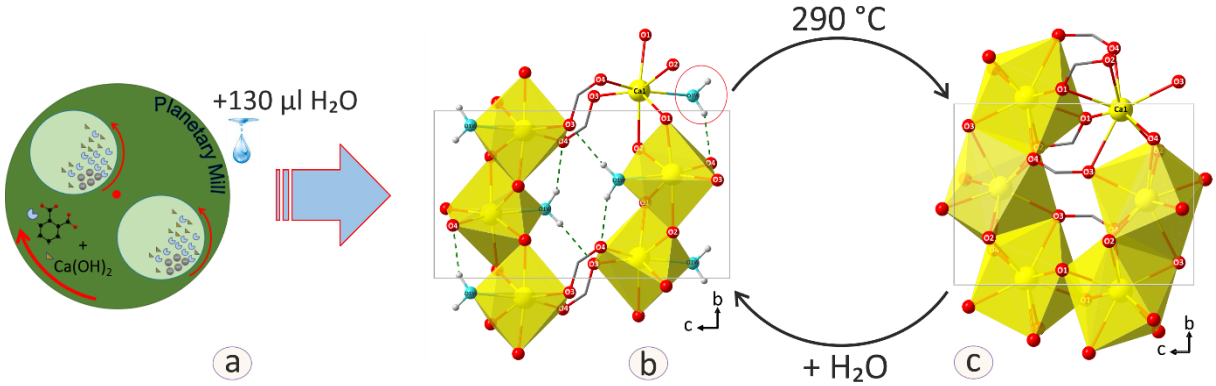

Figure 5.11: Mechanochemical synthesis and crystal structures of Ca-phthalate. (a) [Ca(*o*BDC)(H₂O)] (**10**) was obtained by milling powder mixture of $Ca(OH)_2$ and phthalic acid $H_2o\text{BDC}$ in a planetary mill. (b) Crystal structure of [Ca(*o*BDC)(H₂O)] (**10**). (c) A new dehydrated phase [Ca(*o*BDC)] (**10-H₂O**) was obtained by the thermal annealing of the hydrated sample. The hydrated-dehydrated phase transition is reversible. **Color code*: Metal (yellow), carbon (grey), carboxyl-oxygen (red), coordinating water-oxygen (aqua), and hydrogen (light grey). Hydrogen bonds are represented as green dashed lines.

The water molecule is linked via hydrogen bonds to the carboxylate oxygen atoms O1 and O2 (**Figure 5.11b**). Each CaO_7 polyhedron shares two edges (O1, O2) with the neighboring CaO_7

polyhedrons (**Figure 5.13d**) and to form infinite chains along the crystallographic b-axis. The intermetallic distance within the 1D chains is 3.898(3) Å for each CaO_7-(O1, O2)-CaO_7 unit. The 1D polymeric chains are bridged via *o*BDC^{2-} (O3, O4) along the crystallographic c-axis to form the final 2D layer structure of **10**. The distance between the bridged chains is 4.895(2) Å for each CaO_7-(O3, O4)-CaO_7 unit. The interlayer Ca···Ca distance amounts to 11.221(2) Å.

[Ca(*o*BDC)] (10-H_2O): The thermoanalytical data of **10** indicate the formation of a dehydrated compound around 290 °C which is stable up to 400 °C (**Figure 5.14a**). Upon this result, a thermal post-treatment was performed for the hydrated compound **10** at 290 °C. The PXRD patterns of the resulting dehydrated Ca-phthalate [Ca(*o*BDC)], named (**10-H_2O**), and the hydrated compound **10** are compared in **Figure 5.20c**. The new structure of **10-H_2O** was solved in the monoclinic space group $P2_1/c$. The asymmetric unit is composed of one Ca^{2+}-ion and one phthalate anion. Ca^{2+}-ion is surrounded by eight carboxylate oxygen atoms (**Figure 5.13**) from six organic ligands. The average Ca-O(carboxyl) distance is 2.446 Å, which is slightly longer than the corresponding one in the hydrated compound **10**. Each polyhedron shares edges with the neighboring polyhedrons to from 1D chains along the crystallographic b-axis. The intermetallic distance within a 1D polymeric chain is 3.561(5) Å for each Ca-(O2,O3,O4)-Ca unit. The chains are alternately bridged via two carboxylate oxygen atoms. The distance is 3.633(5) for each Ca-(O1,O1')-Ca unit. Layers of the 2D polymeric chains form the final structure of **10-H_2O** (**Figure 5.11c**).

[{Sr(*o*BDC)(H_2O)$_2$}·H_2O] (11): The asymmetric unit is formed from one Sr^{2+}-cation, one *o*BDC^{2-} anion, and three water molecules. The nine-fold coordination of the Sr^{2+}-ion (**Figure 5.13f**) comprises six carboxylate oxygen atoms from four *o*BDC^{2-} anions and three oxygen atoms belong to the coordinating water molecules. Each SrO_9 polyhedron shares one edge with each of the three adjacent SrO_9 polyhedra and extends into a 2D polymeric chain along the crystallographical b- and c-axes (**Figure 5.12**). The separations between each two neighboring metal centers are 4.238(2) Å for the two Sr···(O1w,O3)···Sr and 4.167(2) Å for the Sr···(O2, O2')···Sr. The 2D chains are stabilized by hydrogen bonding network via the cocrystallized water molecule (O3w). Layers of the 2D chains form the crystal structure of **11**. The interlayer separation is Sr^{2+} ··· Sr^{2+} is 12.612(2) Å.

Compared to its fluorinated counterpart, the crystal structure of the fluorine-free CP **11** embraces a cocrystallized water molecule besides the two Sr-bound water molecules (**Figure 5.12b**).

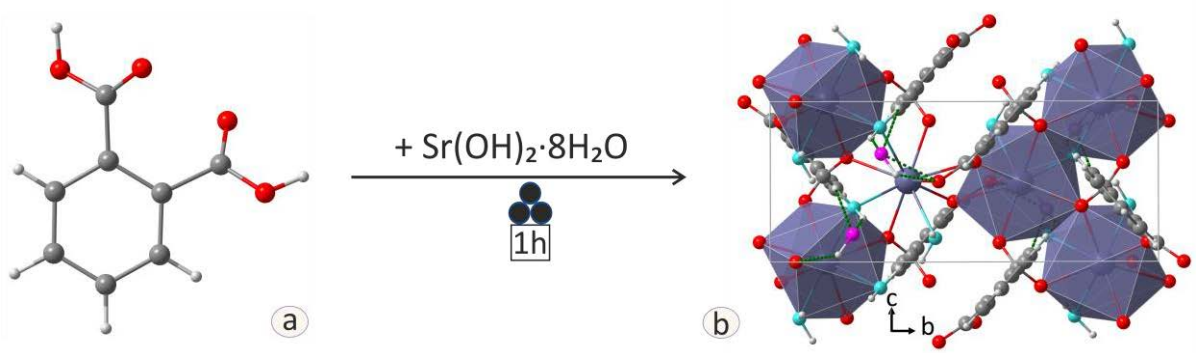

Figure 5.12: Mechanochemical synthesis and Crystal structure of [{Sr(*o*BDC)(H₂O)₂}·H₂O] (**11**). **Color code*: Metal (grey-blue), carbon (grey), carboxyl-oxygen (red), coordinating water-oxygen (aqua), cocrystal water-oxygen (pink), and hydrogen (light grey). Hydrogen bonds are represented as green dashed lines.

The crystal structure of the fluorinated compound **6** only comprises two Sr-bound water molecules (**Figure 5.1c**). The presence of the water molecules and the carboxylate oxygen atoms stabilize the crystal structures of **6** and **11** via building up hydrogen bonding networks. The average Sr-O(carboxyl) bond length is 2.566 Å in the structure of **6** which is shorter than the average Sr-O(carboxyl) bond length 2.675 Å in the structure of **11**. In the structure of **6**, the average Sr-O(water) bond length is 2.750 Å in addition to the longer Sr–O2w' bond length 3.162(2) Å. The average Sr–O(water) bond length is 2.678 Å in the structure of **11**. These results are comparable to the reported Sr-O bond lengths in related compounds deposited in the Cambridge Structural Database,[143] except for the longer distance of Sr-O2w' = 3.183(2) Å in **6** which is rarely described for Sr-O(water) bond lengths.[205]

5.2.3. Coordination System and EXAFS Data

The coordination modes of *para*-, *meta*-, and *ortho*-organic linkers are influenced by their different geometries (**Figure 5.13**). In the hydrated structures of Ca- and Sr-terephthalates, *p*BDC^{2-} anions chelate one metal and bridge another two metals via one carboxylate group. The other carboxylate is free of coordination (**Figure 5.13a**). In the dehydrated systems, both carboxylate anions participate equally in the coordination and extend the dimensionality to 3D-CPs (**Figure 5.9c**). The angular linker *m*BDC^{2-} chelates two metals and bridge another two metals to form 1D-helices (**Figure 5.13c**). The two carboxylates in *ortho* positions allow

the *o*BDC^{2-} linker to chelate metal cations via two oxygen atoms from two carboxylates (**Figure 5.13d-f**).

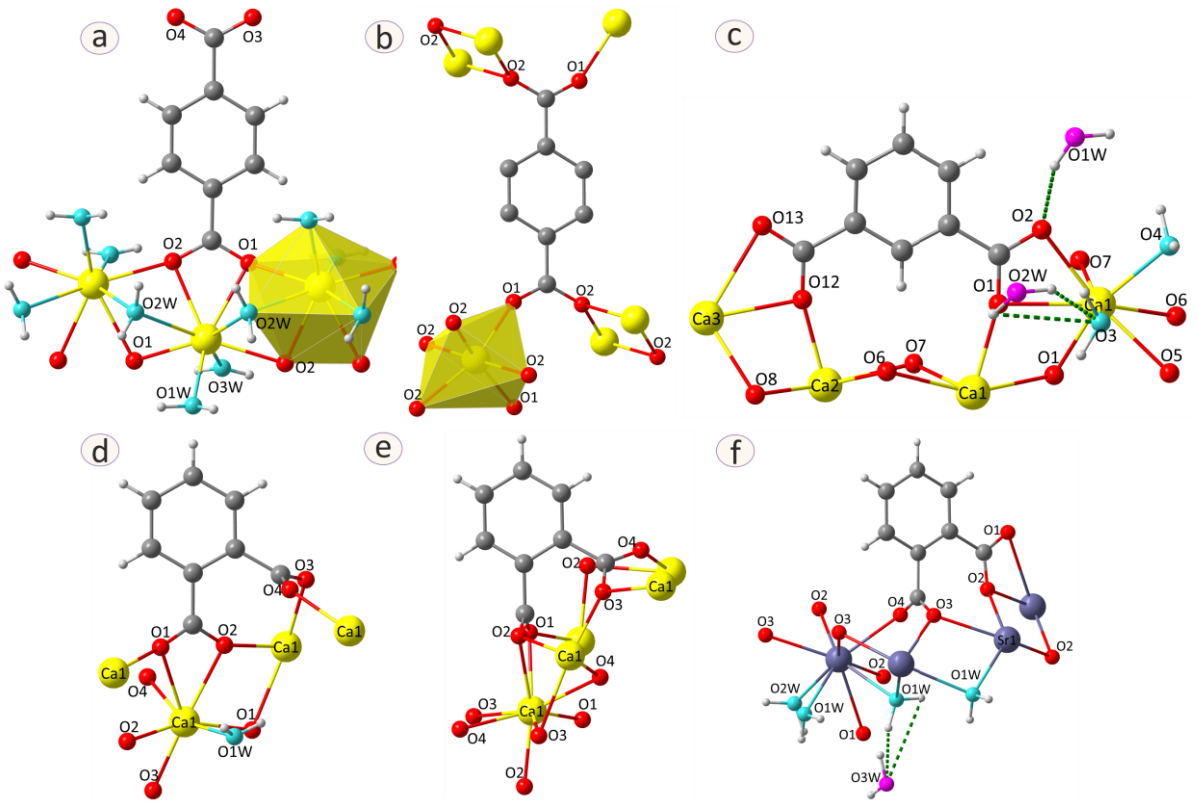

Figure 5.13: Coordination modes of organic linkers, local coordination around metals, and bridged chains in the crystal structures of compounds **7** (a), the dehydrated structure of **7** (b), **8** (c), **10** (d), **10-H$_2$O** (e), **11** (f). Only one polyhedron is shown in each structure for clarity. **Color code*: Metal (yellow, grey-blue), carbon (grey), carboxyl-oxygen (red), coordinating water-oxygen (aqua), cocrystal water-oxygen (pink), and hydrogen (light grey). Hydrogen bonds are represented as green dashed lines.

These fluorine-free linkers differ from their perfluorinated analogs in their coordination modes to Ca- and Sr-ions. For example, the perfluorinated organic linker *o*BDC-F$_4^{2-}$ and the fluorine-free organic linker *o*BDC^{2-} have different coordination modes in their coordination to Sr-ions. Each *o*BDC-F$_4^{2-}$ anion coordinates to five Sr^{2+}-ions. One carboxyl group (O1, O2) chelates one Sr^{2+}-ion and bridges it to two adjacent metals. For the second carboxyl group, each oxygen atom (O3, O4) acts monodentately and indirectly connects two Sr^{2+}-ions (**Figure 5.3c)**. Each *o*BDC^{2-} anion coordinates to four Sr^{2+}-ions. One carboxyl group (O1, O2) chelates one Sr^{2+}-ion. For the second carboxyl group, each oxygen atom (O3, O4) coordinates to one metal atom. Notably, the two carboxylic groups are bridged via the coordination of the two carboxylate oxygen atoms (O2 and O4) to the fourth Sr^{2+}-ion (**Figure 5.13f**). The local

coordination environment around Ca^{2+}-ions in the refined structures of **7, 8, 10** and Sr^{2+}-ion in **11** was investigated by EXAFS data. The fits of the experimental data along with the simulated spectra are shown in **Figure A.9** indicating good agreements between the first coordination spheres around the respective metal with those of the determined structures.[204]

5.2.4. Thermal Properties

For compound **7**, the release of the three coordinating water molecules is completed at 200 °C. The water-free [Ca(*p*BDC)] is stable up to 400 °C.[83] The thermal annealing of the mechanochemically synthesized Ca- and Sr-terephthalates[83] resulted in the formation of the dehydrated compounds [M^{II}(*p*BDC)].[83,152] The similarity between Ca-isophthalate **8** and Sr-isophthalate **9** is established by the thermal analysis measurements (**Figure A.10**). The thermogravimetric (TG) curve of compound **8** (**Figure A.10a**) depicts consecutive mass losses with a total Δm = -23.5% which correspond to the liberation of the water molecules (calc. 23.1% for equivalent 3.4 H_2O). The release of the water molecules is complete at 457 ˚C. The decomposition of the already water-free frameworks [Ca(*m*BDC)] continues with a massive mass loss of 15.8% between 457 °C and 602 °C. In contrast to [Ca(*o*BDC)] (**10-H_2O**), which depicts a long range of stability (290 - 430 °C), the water-free [Ca(*m*BDC)] (**8-H_2O**) does not show long stability. The latter begins immediately to decompose after the liberation of the crystal water molecules. The TG curves support the finding that **9** is similar to the Ca-containing sample **8** (**Figure A.10c**). The thermoanalytical curves of **9** (**Figure A.10b**) initiate with a mass loss of -6.4% in the temperature range between 17˚C and 138˚C (peak maximum 125˚C). This step is followed by another mass loss of -12.4% between 138˚C and 266˚C (peak maximum 179˚C). These consecutive two steps with a total mass loss of -18.8% are mainly caused by the liberation of crystal water. The continuing release of water in the latter step is accompanied by release fractions of CO_2. The quantification of both releases was not possible. The decomposition of [Sr(*m*BDC)] framework continues with a tiny mass loss of -0.8% at the temperature range 266˚C - 423˚C. This step was followed by a mass loss of -9.3% between 423˚C and 601˚C with continues release of CO_2. The PXRD patterns of compounds **8** and **9** as-synthesized and after thermal annealing are compared in **Figure A.11**. The thermoanalytical curves (**Figure 5.14a**) depict the expected mass losses belonging to the loss of one water molecule in the hydrated compound **10**. The release of the coordinating water molecule is complete at 290 ˚C with a total Δm = -10.1% (calc. 10% for $1H_2O$).

The already water-free framework [Ca(*o*BDC)] is stable up to 430 ˚C. A new crystalline compound [Ca(*o*BDC)] (**10-H_2O**) was formed after thermal annealing of **10** at 290 °C.[204]

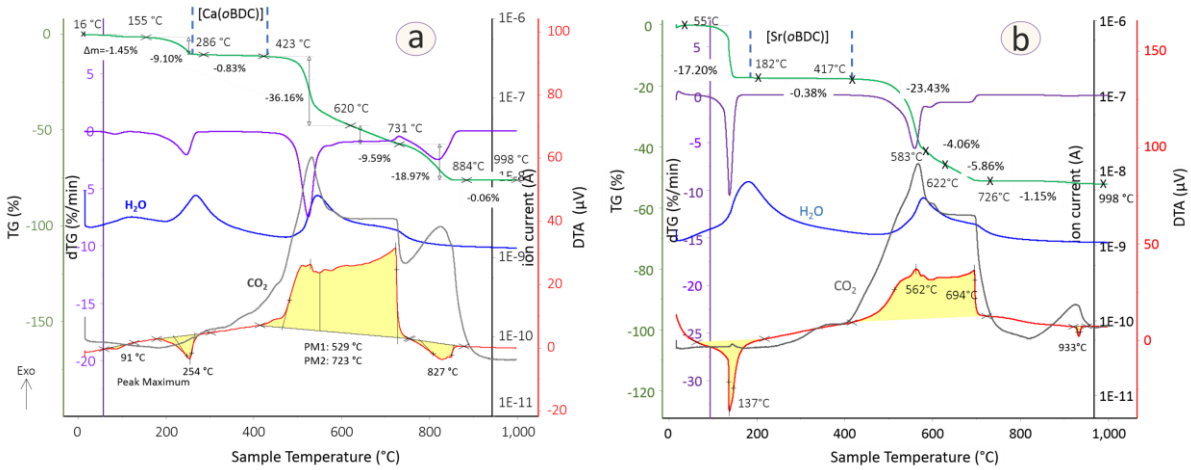

Figure 5.14: Thermoanalytical curves of (a) [Ca(*o*BDC)(H_2O)] (**10**) and (b) Thermoanalytical curves of [{Sr(*o*BDC)(H_2O)$_2$}·H_2O] (**11**).

The TG curve of Sr-CP **11** (**Figure 5.14b**) begins with two consecutive steps with a total mass loss of -17.40% correspond to the release of three water molecules (calculated: -17.7%). The water-free [Sr(*o*BDC)] framework exhibits higher thermal stability and begins to decompose at about 400 °C with a mass loss of -23.4% along with the release of CO_2 fractions (peak maximum: 372 ˚C). Mass losses of -4.06% and -5.86% are followed. The complete release of the coordinating water molecules occurs mainly together with the release of CO_2 molecules. The elemental analysis results after the thermal post-treatment at 300 °C and 400 °C are given **Table A.2**. The thermally treated sample exhibits the formation of a new phase which is different from the hydrated compound. The PXRD patterns of hydrated and dehydrated samples are compared in **Figure 5.20d**.

5.2.5. MAS NMR and IR Spectra

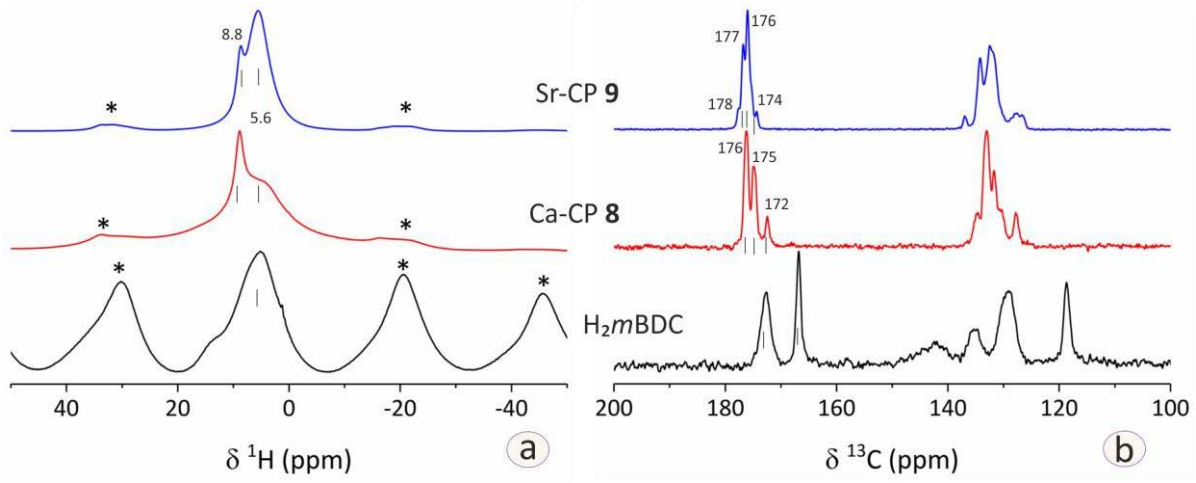

Figure 5.15: MAS NMR spectra of the organic ligand [H_2*m*BDC] (black spectra), [Ca(*m*BDC)(H_2O)$_{3.4}$] (**8**) (red spectra), and [Sr(*m*BDC)(H_2Oa)$_{3.4}$] (**9**) (blue spectra). (a) ^{1}H MAS NMR spectra (ν_{rot} = 10 KHz). (b) ^{1}H→^{13}C CP MAS NMR spectra (ν_{rot} = 10 KHz, the applied contact time (P15) = 10 ms.

In the ^{1}H MAS NMR spectra (**Figure 5.15a**), the presence of water molecules embedded within the crystal structures. Ca-isophthalate **8** (red spectrum) and Ca-isophthalate **9** (blue spectrum) are indicated by the contribution at a chemical shift of 5.6 ppm in both spectra**.** The narrower lines around δ = 8.8 ppm in both spectra are mainly due to the strongly bridged hydroxyl groups and the existence of hydrogen bonding interactions. The ^{1}H→^{13}C CP MAS NMR spectra (**Figure 5.15b**) depict different contributions and are assigned to different types of carbon atoms in carboxylate groups at δ = 176, 175, and 172 ppm for compound **8** (red spectrum). These contributions are attributable to the different coordination modes of carboxylic groups in their coordination with Ca-atoms. The chemical shifts around δ = 135, 133, 132, 130, and 128 ppm in the red spectrum are assigned to non-equivalent crystallographic positions of carbon atoms in the aromatic ring. Similar to Ca-isophthalate, the ^{1}H→^{13}C CP MAS NMR spectrum of **9** (blue spectrum) shows various contributions are assigned to different types of carboxyl carbon atoms (at δ = 178, 177, 176, and 174 ppm). The chemical shifts around δ = 137, 134, 132, 128, and 127 ppm in the blue spectrum are assigned to non-equivalent crystallographic positions of carbon atoms in the aromatic ring (five different carbon atoms, at least). These similarities between the measured MAS NMR spectra of **8** and **9** support our finding that both compounds are isomorphous.

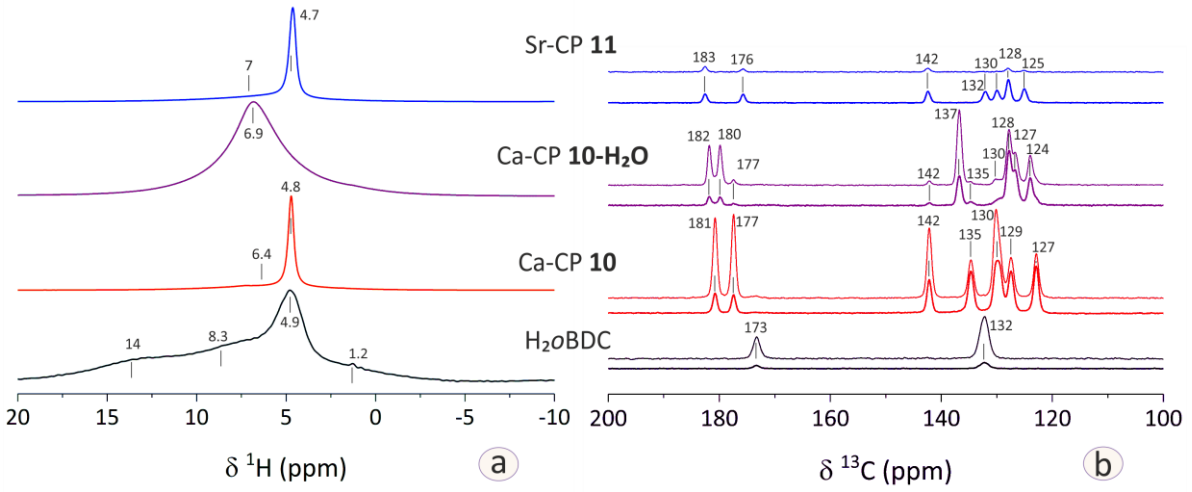

Figure 5.16: MAS NMR spectra of the organic ligand [H_2*o*BDC] (black spectra), [Ca(*o*BDC)(H_2O)] (**10**) (red spectra), [Ca(*o*BDC)] (**10-H_2O**) (purple spectra), and [{Sr(*o*BDC)(H_2Oa)$_2$}·H_2O] (**11**) (blue spectra). (a) ^{1}H MAS NMR spectra (ν_{rot} = 10 KHz). (b) ^{1}H→^{13}C CP MAS NMR spectra (ν_{rot} = 10 KHz, the applied contact time = 1 and 10 ms.

In the ^{1}H MAS NMR spectra (**Figure 5.16a**), the presence of a water molecule embedded within the crystal structure of **10** is indicated by the contribution at a chemical shift of 4.8 ppm (red spectrum)**.** The small contribution at δ = 6.4 ppm (not visible in the shown red spectrum) and at δ = 6.9 ppm in the dehydrated compound **10-H_2O** (purple spectrum) are due to the bridged protons. The ^{1}H→^{13}C CP MAS NMR spectra (**Figure 5.16b**) depict different contributions and are assigned to different types of carbon atoms in carboxylate groups at δ = 181 and 177 ppm for compound **10** (blue spectrum) and δ = 182, 180, and 177 ppm for compound **10-H_2O** (purple spectrum). These contributions are attributable to the different coordination modes of carboxylic groups in their coordination with Ca-atoms. The chemical shifts around δ = 142, 135, 130, 129, and 127 ppm in **10** and at δ = 142, 137, 135, 130, 128, and 124 ppm in **10-H_2O** are assigned to non-equivalent crystallographic positions of carbon atoms in the aromatic ring.

The ^{1}H MAS NMR spectrum of compound **11** (blue spectrum) is dominated by a narrow ^{1}H signal at a chemical shift of 4.7 ppm. It covers a broad peak at 7 ppm which can be attributed to the protons in the benzene ring. The narrow line can be assigned to crystal water. The presence of a broad peak at about 7 ppm is supported by the simulation of the ^{1}H MAS NMR spectrum of **11**. Both recorded and simulated spectra are in a good agreement as shown in **Figure 5.17**. The ^{1}H→^{13}C CP MAS NMR spectra (**Figure 5.16b**, blue

spectrum) of CP **11** provides evidence for the existence of two different carbon sites in the carboxylate groups at δ = 183 ppm and at δ = 176 ppm. The separation between the two chemical shifts assigned to the two carbon sites in carboxylate groups is 5 ppm. Four carbon sites are identified for the carbon atoms in the benzene ring at δ = 132, 130, 128, and 125 ppm. The intensity of the four signals is reduced applying the longer contact time (contact time: 10 ms), which is typical for the magnetization transfer over a longer distance.

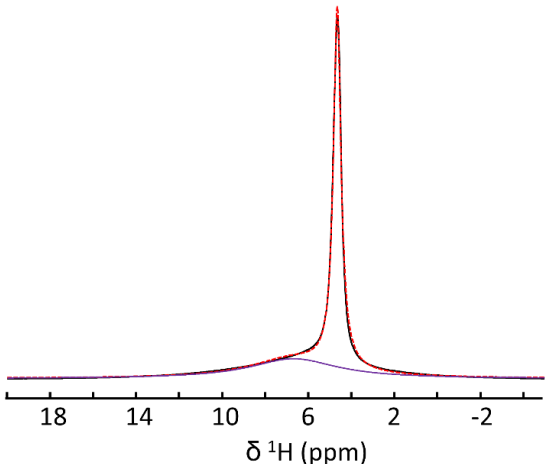

Figure 5.17: The simulation of ^{1}H MAS NMR spectrum for [{Sr(*o*BDC)(H_2Oa)$_2$}·H_2O] (**11**).

The ATR-IR spectra of Ca-isophthalate **8** and Sr-isophthalate **9** are compared in **Figure 5.18a**. The main vibrational bands assigned to carboxylate stretching in compounds **8** appear at 1528 cm^{-1} for asymmetric stretching and 1392 cm^{-1} for symmetric stretching (red spectrum). The vibrational bands assigned to the carboxylate stretching in **9** (blue PXRD pattern) appears at 1530 cm^{-1} and 1441 cm^{-1} for asymmetric stretching and 1384 cm^{-1} for symmetric stretching. The separations between the two vibrational modes ($\Delta_{as\text{-}s} = \nu_{as} - \nu_s$) are 146 cm^{-1} and 52 cm^{-1} which are similar to Ca-isophthalate **8** (red PXRD pattern) and are attributable to the multidentate coordination mode of carboxylate groups in both compounds.[73,203] The broad contributions around 3500 cm^{-1} in both compounds are due to the crystal water molecules and the formation of hydrogen-bonding networks along the crystal structures.[148] The main vibrational bands assigned to carboxylate stretching in compounds **10** (**Figure 5.18b**) are at 1544 cm^{-1} for asymmetric stretching and at 1408 cm^{-1} for symmetric stretching (red spectrum). In the dehydrated compound **10-H_2O** (purple spectrum), the main contributions correspond to asymmetric and symmetric stretching are assigned at 1528 and 1406 cm^{-1}, respectively. The separations between the two vibrational modes in CPs **10** and **10-H_2O** are 136 cm^{-1}. The broad contribution around 3400 cm^{-1} in compound **10** is due to the crystal water molecules and the formation of hydrogen-bonding networks along the crystal structure.[148] The absence of the latter vibrational bands in the purple spectrum indicates that CP **10-H_2O** is free of water. The formation of

the Sr^{2+}-O(carboxylates) and the presence of the water molecules in **11** are also indicated by the ATR-IR spectrum (**Figure 5.18b**, blue spectrum). The main vibrational bands assigned to the carboxylate stretching appear at 1530 cm^{-1} for asymmetric stretching, and at 1393 cm^{-1} for symmetric stretching. The separation (Δ_{a-s}) is about 137 cm^{-1}. The broad contributions around 3065 - 3395 cm^{-1} is assigned to the HBNs within the crystal lattices. The bands at 3563 cm^{-1} indicate that some of OH groups do not participate in the HBNs.

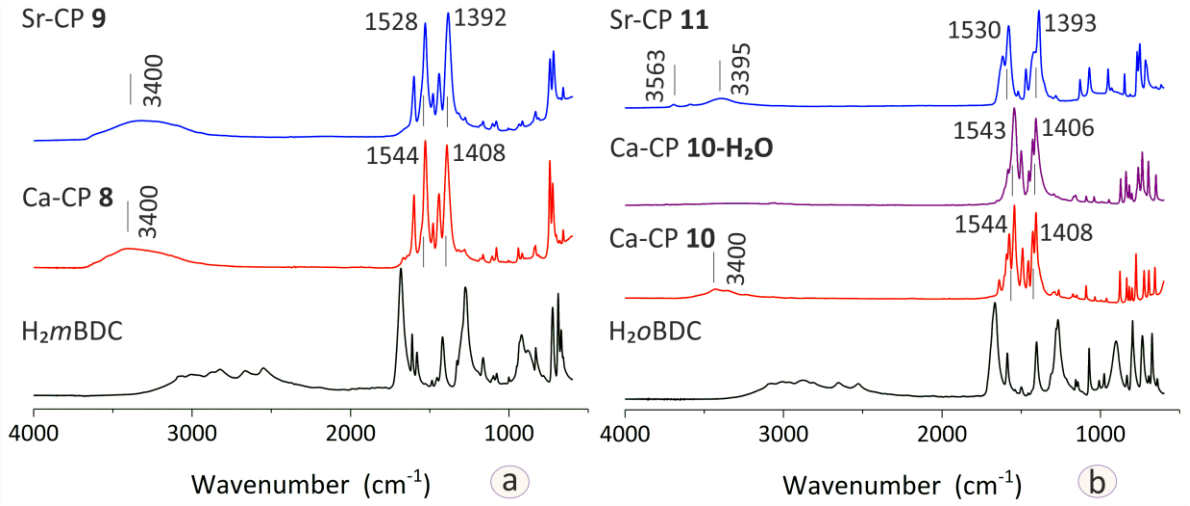

Figure 5.18: ATR-IR spectra of the organic ligands and CPs. (a) [H_2*m*BDC], [Ca(*m*BDC)(H_2O)$_{3.4}$] (**8**), and [Sr(*m*BDC)(H_2Oa)$_{3.4}$] (**9**). (b) [H_2*o*BDC], [Ca(*o*BDC)(H_2O)$_1$] (**10**), [Ca(*o*BDC)] (**10-H_2O**), and [{Sr(*o*BDC)(H_2O)$_2$}·H_2O] (**11**).

5.2.6. Sorption Properties and Morphology

The BET surface areas were determined based on N_2 adsorption isotherms. The hydrated samples exhibit small surface areas.[87,88] Similar to Ca-isophthalate, the surface area of CP **9** remains almost unchanged even after sample treatment at different temperatures. The hydrated compound **10** depicts a small specific surface area (4.2 m^2/g) which increases in the dehydrated compound **10-H_2O** to 14.3 m^2/g. The hydrated CP **11** exhibits a small surface area of 5 m^2/g. After treatment at 250 ˚C, the surface area decreased to 4.3 m^2/g. At 290 ˚C and 390 ˚C, the surface area remains unchanged in the water-free compound.

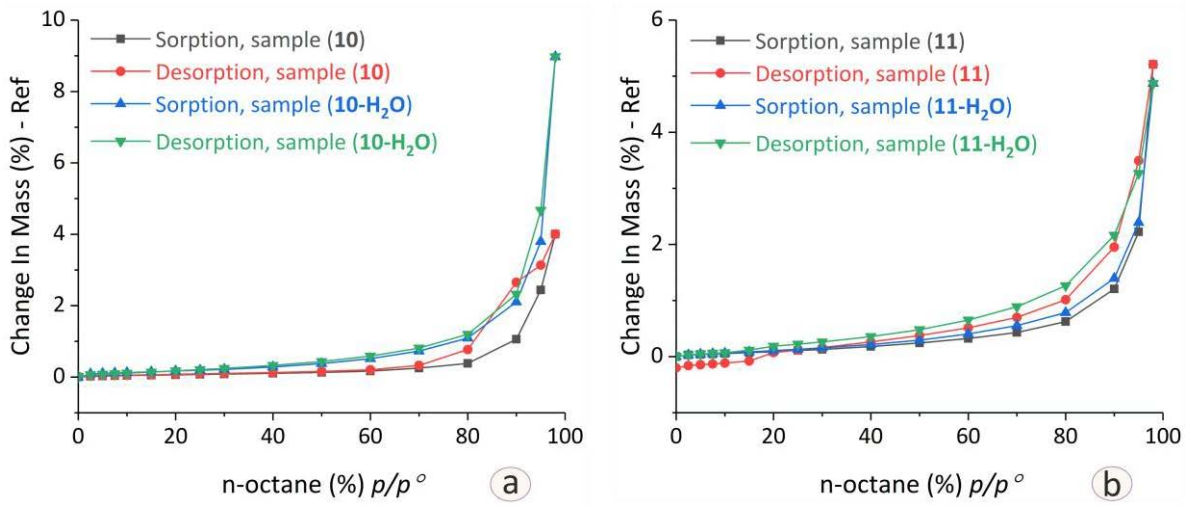

Figure 5.19: Isotherm curves for the dynamic vapor sorption of *n*-octane on samples as synthesized (black and red curves) and after thermal post-treatment (blue and green curves). (a) Ca-CP **10** and **10-H₂O**. (b) Sr-CPs **11** and **11-H₂O**.

These results are consistent with the measured BET surface areas for the hydrated and dehydrated Sr-terephthalates. The latter exhibits even a smaller surface area (6.1 m^2/g) compared to the hydrated sample (9.5 m^2/g).[84]

For more investigations, the dynamic vapor sorption (DVS) of n-octane on samples of the hydrated CPs **10** and **11** and their dehydrated phases were performed. The sorption properties of the dehydrated sample **10-H₂O** are notably enhanced compared to the hydrated CP **10** as shown in **Figure 5.19**. The isotherm curves for the DVS of water on the dehydrated compound **10-H₂O** depict that water is chemically adsorbed over the dehydrated sample and indicate the formation of a new rehydrated compound (**Figure 5.20a**). The PXRD pattern of the sample after controlled rehydration is identical to the PXRD pattern of the sample as-synthesized and indicate that the phase transition is a reversible process (**Figure 5.20c**). The DVS of water over the dehydrated sample of Sr-CP **11-H₂O** indicate physical sorption (**Figure 5.20b**) and that phase transition is irreversible (**Figure 5.20d**).

SEM images of CPs **7**-**11** depict similar morphology to their fluorinated counterparts, plate-like structures as shown in **Figure 5.21**.

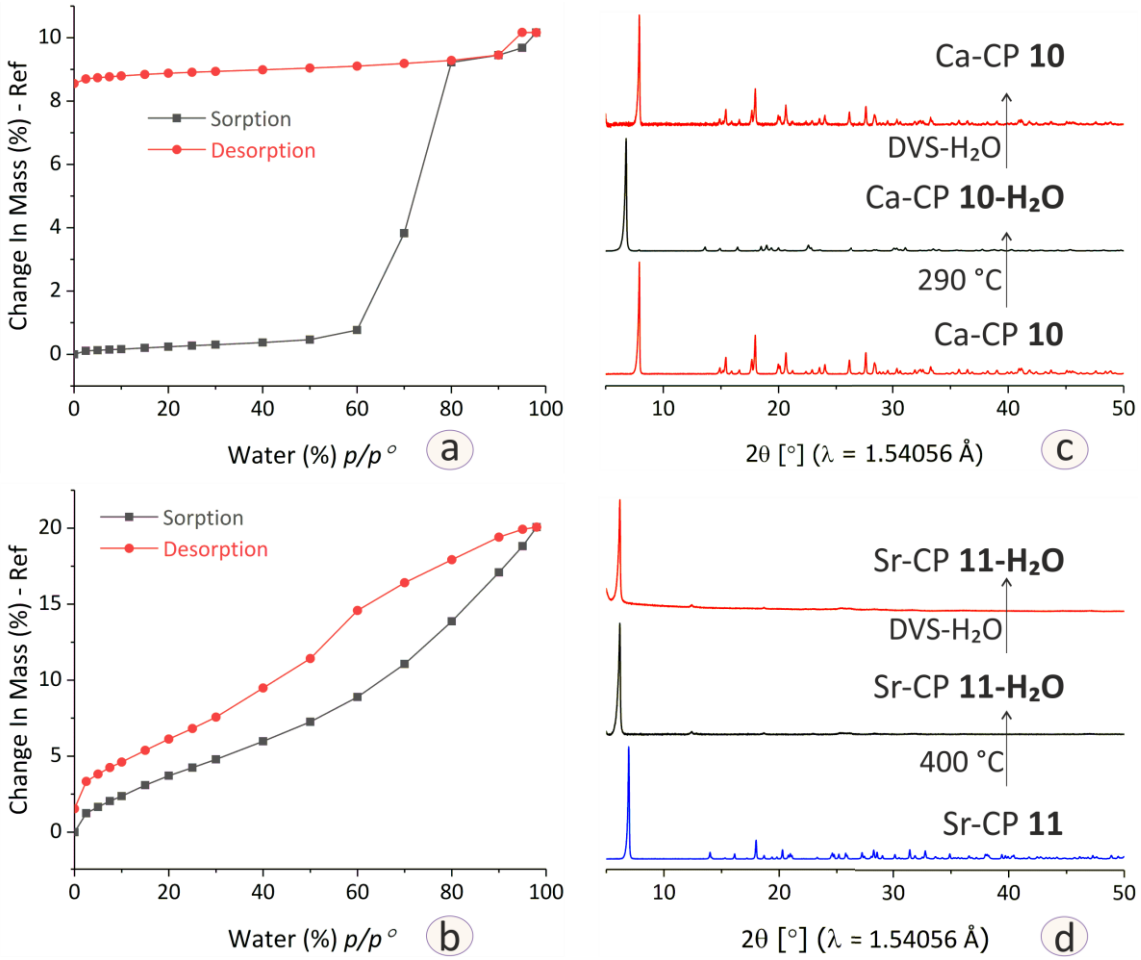

Figure 5.20: Isotherm curves for the dynamic vapor sorption of water on the dehydrated samples: (a) [Ca(*o*BDC)] (**10-H₂O**) and (b) [Sr(*o*BDC)] (**11-H₂O**). PXRD patterns of samples as synthesized, dehydrated, and after DVS of water: (c) [Ca(*o*BDC)(H_2O)$_1$] (**10**) and (**10-H₂O**), (d) [{Sr(*o*BDC)(H_2O)$_2$}·H_2O] (**11**) and **(11-H₂O**).

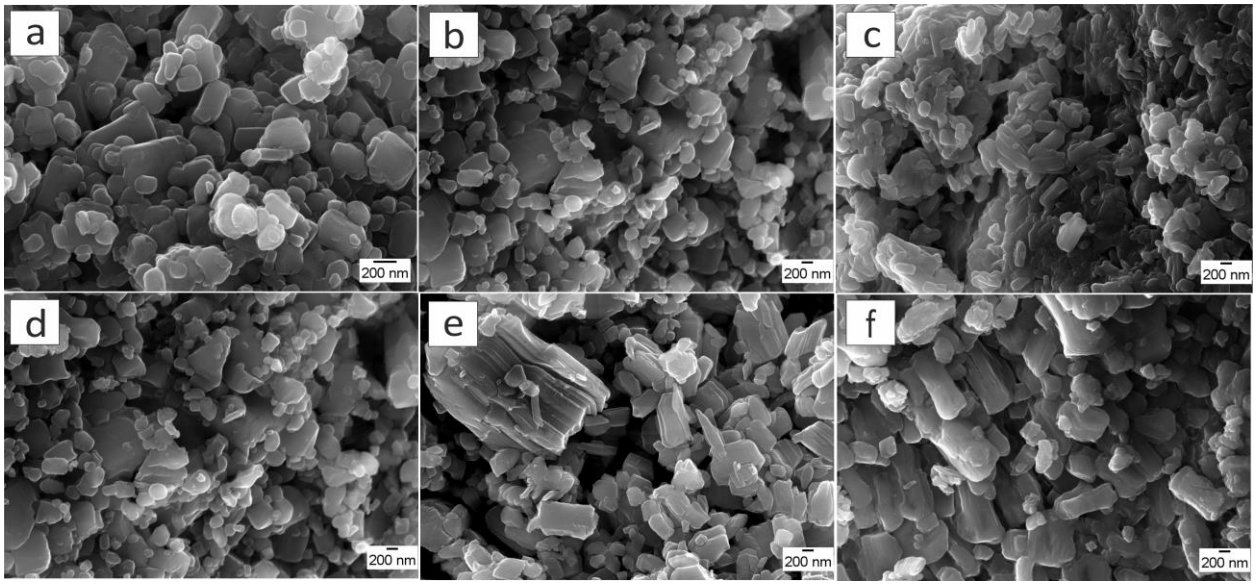

Figure 5.21: SEM images for the compounds (a) [Ca(*p*BDC)(H_2O)$_3$] (**7**), (b) [Ca(*m*BD)(H_2O)$_{3.4}$] (**8**), (c) [Sr(*m*BDC)(H_2O)$_{3.4}$] (**9**), (d) [Ca(*o*BDC)(H_2O)$_1$] (**10**), (e) [Ca(*o*BDC)] (**10-H_2O**), (f) [{Sr(*o*BDC)(H_2O)$_2$}·H_2O] (**11**).

5.2.7. Comparison and Conclusion

In summary, Ca- and Sr-coordination polymers based on benzene-dicarboxylates [M^{II}(BDC)(H_2O)$_n$] were synthesized by milling powders of $Ca(OH)_2$ or $Sr(OH)_2·8H_2O$ with terephthalic acid (H_2*p*BDC), isophthalic acid (H_2*m*BDC), or phthalic acid (H_2*o*BDC). Mechanochemical reactions were performed in a planetary mill. The stoichiometric ratio between the inorganic and organic reactants was 1:1. The best crystalline products were obtained when a small amount of water (130 µl H_2O) was added to the powder mixture of $Ca(OH)_2$ and H_2*p*BDC and by using $Sr(OH)_2·8H_2O$ as an inorganic source. Like Ca-terephthalates (**7**), a dehydrated compound [Ca(*o*BDC)] (**10-H_2O**) was obtained after the thermal post-treatment of the hydrated Ca-phthalate (**10**) in a reversible phase transition process. The thermal annealing of [Ca(*m*BDC)(H_2O)$_{3.4}$] (**9**) resulted in very poor crystalline products. The dehydrated Ca-terephthalate is reported. The new crystal structure of the dehydrated compound (**10-H_2O**) and the Sr-based CP (**11**) were solved *ab initio* based on the powder X-ray diffraction data. The structures of compounds **7**, **8**, **10**, **10-H_2O,** and **11** were refined using the Rietveld method. The determined structures were validated by fitting the recorded and simulated EXAFS spectra. The structural topologies and coordination environments in the resulting Ca- and Sr-based coordination polymers are determined by

the chemical nature and geometries of organic linkers (**Figure 5.13**). In its coordination with Ca and Sr atoms, the *para*-systems acts as a unidentate to extend the polymeric chains in 1D-connections. The connections rise to a 3D network via hydrogen bonds. Both *ortho*- and *meta*-isomers bridge Ca-atoms in an exo-bidentate fashion to propagate the polymeric network in 2D or 1D-networks, respectively. In addition to the covalent Ca-O interaction, intensive networks of the non-covalent interactions stabilize the hydrated crystal structures. In the dehydrated systems, both *para*- and *ortho*-linkers play crucial roles for extending the coordination into 3D- and 2D-structures, respectively.

[{Sr(*o*BDC)(H_2O)$_2$}·H_2O] (**11**) was obtained by grinding $Sr(OH)_2·8H_2O$ with phthalic acid (H_2*o*BDC). Similar to the fluorinated counterpart **6**, compound **11** crystallizes in the monoclinic space group $P2_1/c$ as a 2D-CP. The water-free framework of **11** begins to decompose only above 400 ˚C. The hydrated compound **11** exhibits a small surfaces area which remains unchanged for the dehydrated sample. Both hydrated and dehydrated samples show similar dynamic sorption isotherms. The transformation of CP **11** into a new dehydrated phase upon a thermal post-treatment is irreversible.

Table 5.2: Coordination environment, crystal data, and refined parameters derived from the crystal structures of compounds **7**, **9**, **11**, **11-H_2O**, **and 12**.

	[Ca(*p*BDC)$(H_2O)_3$] (**7**)	[{$Ca_{2.5}$(*m*BDC)$_{2.5}(H_2O)_{4.5}$}·4H_2O] (**8**)	[Ca(*o*BDC)$(H_2O)_1$] (**10**)	[Ca(*o*BDC)] (**10-H_2O**)	[{Sr(*o*BDC)$(H_2O)_2$}·H_2O] (**11**)
C.N.	CaO_8	CaO_8 (Ca1, Ca2) / CaO_9 (Ca3)	CaO_7	CaO_8	$SrO_{(8+1)}$
Coordinating oxygen (carboxyl)	4O (from 3 ligand anions)	6O (from 4 ligand anions)	6O (from 4 ligand anions)	8O (from 6 ligand anions)	6O (5 Linkers)
Coordinating oxygen (water)	2 terminals (O1w, O3w) 2 bridging (O2w, O2w')	Ca1 (2 terminal: O3 and O4), Ca2 (1 terminal: O10, 1 bridging: O11), Ca3 (1 terminal: O14, 2 bridging: O11, O11')	1 (O1w)	-	2 (O1w, O2w)
Cocrystal water	-	4 (O1w, O2w, O3w, O4w)	-	-	-
Coordination mode (Ligand)	3 metals (chelate, bridge)	4 metals (chelate, bridge)	4 metals (chelate, bridge)	6 metals (chelate, bridge)	5 metals (chelate, bridge)
M-O(carboxylate) (Å)	2.350(1) - 2.530(1)	2.3626(1) - 2.6567(1)	2.307(5) - 2.595(5)	2.283(8) - 2.633(9)	2.426(2) - 2.774(1)
M-O(water) (Å)	2.375(1) - 2.637(1)	2.3446(1) - 2.6373(1)	2.381(5)	-	2.688(1) - 2.732(1), 3.183(2)
O-M-O angle (°)	51.689(1) - 148.551(1)	50.280 (2) - 159.641(2)	51.001(1) - 157.254(2)	51.345(3) -154.472(3)	49.434(4) - 150.287(7)
M-(bridged)-M (chain) (Å)	Ca1-(O1, O2, O2w)-Ca = 3.640(1)	3.8747(1) (Ca1-(O6, O7)-Ca2) 3.6414(2) (Ca2-(O8, O11, O12)-Ca3)	Ca-(O1,O2)-Ca = 3.898(3)	Ca-(O2,O3, O4)-Ca = 3.561(5) Ca-(O1,O1')-Ca = 3.633(5)	Sr-(O1,O1')-Sr = 4.242(5), Sr-(O2,O2')-Sr = 4.008(6), Sr-(O2w,O2w')-Sr = 5.063(5)
M—M—M angle (°)	Ca-O1-Ca = 96.346(1) Ca-O2-Ca = 97.044(1)	Ca1-O1-Ca1 = 104.646(2) Ca1-O6-Ca2 = 102.354(2) Ca1-O7-Ca2 = 103.501(2) Ca2-O8-Ca3 = 96.974(2) Ca2-O12-Ca3 = 96.430(2)	Ca-O1-Ca = 105.184(2) Ca-O2-Ca = 108.091(2)	Ca-O1-Ca = 97.584(3) Ca-O2-Ca = 92.556(3) Ca-O3-Ca = 89.783(3) Ca-O4-Ca = 96.107(4)	80.987(4), 116.391(7), 126.068(6)
Dimensionality	1D, I^1O^0	1D, I^1O^0	2D, I^1O^1	2D, I^2O^0	2D, I^2O^0
Cell parameters					
Formula sum	$Ca_4(C_8H_4O_4)_4(H_2O)_{12}$	$Ca_{20}(C_8H_4O_4)_{20}(H_2O)_{68}$	$Ca_4(C_8H_4O_4)_4(H_2O)_4$	$Ca_4(C_8H_4O_4)_4$	$Sr_4(C_8H_4O_4)_4(H_2O)_{12}$
Formula weight (g/mol)	1032.955	5171.818	888.833	816.772	1422.782
Cell volume ($Å^3$)	1014.53(7)	5334.1(5)	888.59	823.50(10)	1089.58(12)

	[Ca(*p*BDC)(H_2O)$_3$] (**7**)	[{$Ca_{2.5}$(*m*BDC)$_{2.5}$(H_2O)$_{4.5}$}·4H_2O] (**8**)	[Ca(*o*BDC)(H_2O)$_1$] (**10**)	[Ca(*o*BDC)] (**10-H_2O**)	[{Sr(*o*BDC)(H_2O)$_2$}·H_2O] (**11**)
Crystal system	Monoclinic	Monoclinic	Monoclinic	Monoclinic	monoclinic
Space group	$P2_1/c$ (14)	C2/c (15)	$P2_1/c$ (14)	$P2_1/c$ (14)	$P2_1/c$ (14)
a (Å)	7.1114(2)	15.5899(7)	11.2207(3)	13.9820(10)	8.101(5)
b (Å)	21.6561(9)	21.4477(12)	6.68473(16)	6.6512(4)	26.399(12)
c (Å)	6.5925(3)	17.1872(8)	11.9906(3)	9.5747(6)	6.989(4)
β (°)	92.208(5)	111.848(3)	98.8862(8)	112.356(2)	133.198(1)
Cell ratio					
a/b	0.328	0.7269	1.6786	2.1022	0.307
b/c	3.285	1.2479	0.5575	0.6947	3.777
c/a	0.927	1.1025	1.0686	0.6848	0.863
Z	4	8	4	4	4
Density(calc.) (g/cm^3)	1.690	1.610	1.661	1.647	2.168
Refinement parameters					
R_{wp}	3.14	2.13	2.28	2.51	2.99
R_p	2.00	1.60	2.62	1.77	2.08
R_{Bragg}	1.747	0.571	1.143	1.014	1.558
GOF	3.00	1.25	2.19	3.46	3.64
PXRD measurements					
Instrument/ BeamLine	D8 Discover				
Calibration	Si standard powder				
λ (Å)	1.54056 (Cu-$K_{\alpha1}$)				
2θ range (°)	5 – 65				
step size	0.009°, 5 s per step				
Collection time	35 h				
Deposition in CSD					
CCDC	158674	158675	1582672	1582673	1562228
Refcode	CATPAL04	EMIDEJ02	CAPHTH03	PEYYAT02	YECVOU

5.3. Ba-Coordination Polymers: $[Ba(BDC\text{-}F_4)(H_2O)_n]$ and $[Ba(BDC)(H_2O)_n]$

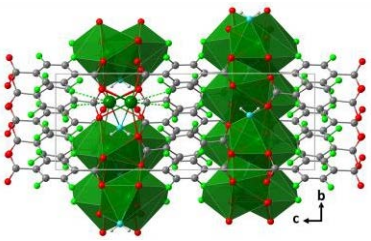

A. Al-Terkawi, G. Scholz, F. Emmerling, E. Kemnitz. *Solid State Sci.*, **2018**, 79, 99-108.

Scientific Aspects:

- Ba-based FCPs and CPs were synthesized by milling Ba-hydroxides with the isomers of tetrafluorobenzene-dicarboxylic systems and their nonfluorinated analogs.
- In milling reactions of Ba-hydroxides with perfluorinated isomers, the variations in the water content of inorganic sources do not influence the coordination systems but affect the crystallinity of final products and the necessary time for complete conversion.
- Variations in the water content of inorganic samples in their milling with benzene-dicarboxylic acids result in different products.
- $[Ba(p\text{BDC-}F_4)(H_2O)_{0.5}]$ (**12**) crystallizes as a 3D-FCP with hybrid inorganic-organic I^2O^1 connectivity.
- The new materials are thermally stable and exhibit small surface areas.

5.3.1. Mechanochemical Synthesis

The milling of Ba hydroxides that vary in their water content and a perfluorinated ligand leads to the formation of the same compound regardless the variation of water content. $[Ba(p\text{BDC-}F_4)(H_2O)_{0.5}]$ (**12**) was obtained by milling $H_2p\text{BDC-}F_4$ and $Ba(OH)_2{\cdot}8H_2O$ (**Figure 5.22**). The same powder product **12** was formed by milling $H_2p\text{BDC-}F_4$ and $Ba(OH)_2{\cdot}H_2O$, $Ba(OH)_2$ and 130 µL water for one hour (12c), or $Ba(OH)_2$ for one hour (12d) (**Figure A.12a**). $[Ba(m\text{BDC-}F_4)(H_2O)_{0.5}]$ (**13**) and $[Ba(o\text{BDC-}F_4)(H_2O)_{1.5}]$ (**14**) were synthesized by milling the perfluorinated ligand with $Ba(OH)_2{\cdot}8H_2O$, $Ba(OH)_2$, or $Ba(OH)_2$ + 130 µl H_2O.[206] However, the water content of the inorganic precursors influences at least the crystallinity of the resulting products and the required time for milling. The highest crystallinity was obtained by using $Ba(OH)_2{\cdot}8H_2O$ as an inorganic source.[87,206]

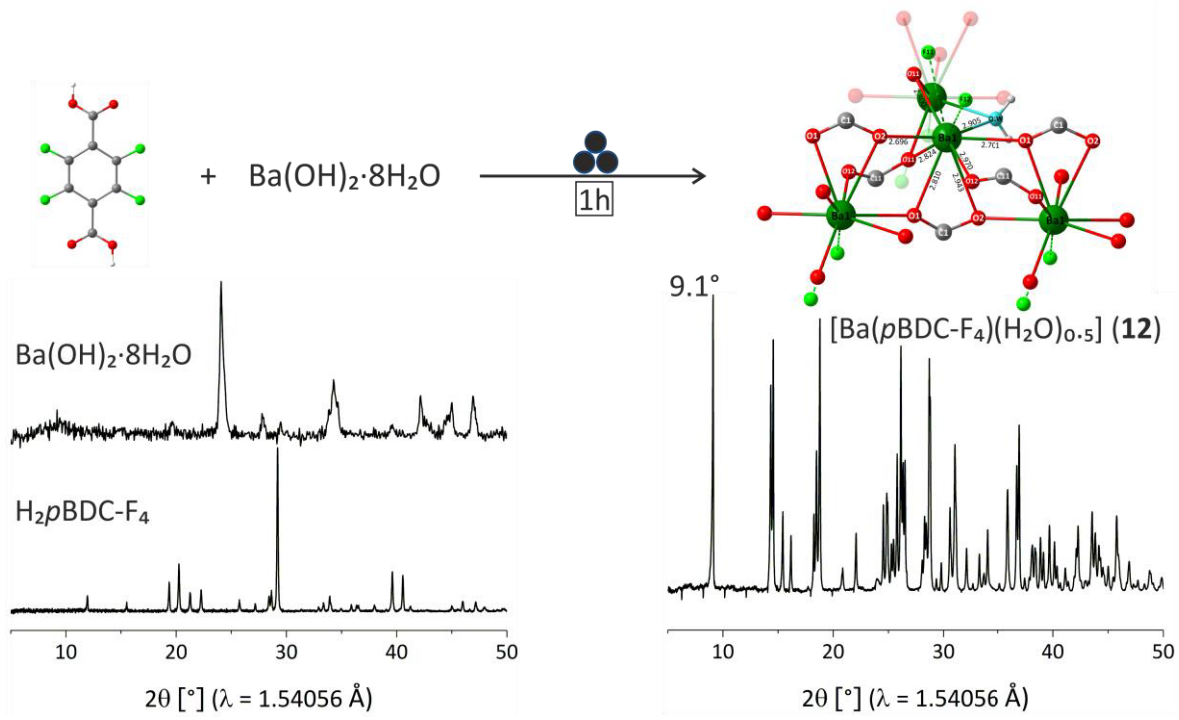

Figure 5.22: Mechanochemical synthesis and experimental PXRD patterns of the reactants and Ba-FCP **12**. [Ba(*p*BDC-F_4)(H_2O)$_{0.5}$] (**12**) was obtained by milling H_2*p*BDC-F_4 and Ba(OH)$_2$·8H_2O. The molar ratio between organic and inorganic precursors was 1:1. Milling time was 1h. A polymeric chain in the 3D-CP **12** is depicted. Parts of the organic linkers are omitted for clarity. **Color code*: Metal (green), carbon (grey), carboxyl-oxygen (red), water-oxygen (aqua), fluorine (bright green), and hydrogen (light grey).

Against this background, the variation of water content mainly influences the coordination system of the fluorine-free products. [Ba(*m*BDC)(H_2O)$_{2.5}$] (**15**) and [Ba(*o*BDC)(H_2O)] (**16**) were obtained by milling Ba(OH)$_2$·8H_2O and isophthalic acid (H_2*m*BDC) and phthalic acid (H_2*o*BDC), respectively. Different products were formed by using Ba(OH)$_2$ as an inorganic precursor or by adding water to the powder mixture (**Figure A.12b**).[206] These results are consistent with the reported work on the mechanochemical synthesis of terephthalate-based CPs where the variation of water content influences the coordination environment of the products.[83] Here; the focus is on products **15** and **16** obtained by milling Ba(OH)$_2$·8H_2O and H_2BDC acids.

5.3.2. Ba-Tetrafluoroterephthalate [Ba(*p*BDC-F_4)(H_2O)$_{0.5}$]

The crystal structure of **12** was calculated and refined based on the synchrotron PXRD data. The first hypothesis of the water-free compound was declined after solving the crystal structure and performing more analytical measurements.[87] The refinement of

[Ba(*p*BDC-F_4)(H_2O)$_{0.5}$] was possible wherein, a water molecule bridges two adjacent Ba^{2+}-ions. The experimental and the simulated powder data after the Rietveld refinement are in a good agreement as depicted in **Figure 5.23**. Crystal data and refined parameters are given in **Table 5.1**.

[Ba(*p*BDC-F_4)(H_2O)$_{0.5}$] (**12**) crystallizes in the monoclinic C2/c space group. The asymmetric unit consists of one metal, two half ligands, and a half water molecule. Ba^{2+}-ion is surrounded by one bridging water molecule, seven carboxylate-oxygen atoms from six organic linkers, in addition to the short Ba···F distances amount to 3.107(3) and 2.975(2) Å for Ba···F11 and Ba···F12, respectively (**Figure 5.24a**). The crystal structure of **12** comprises longer Ba-O distances compared to **1** and **2** (**Table 5.1**). One carboxylate (O1-C1-O2) chelates one Ba-atom and bridge another two. In the other carboxylate (O11-C11-O2), O11 is bidentate to two metal atoms while O12 acts as monodentate to one Ba-atom. Ba^{2+}-ions are arranged in 2D-chains. The inorganic chains are bridged by *p*BDC-F_4^{2-} anions to form the 3D crystal structure of **12** with a hybrid inorganic-organic I^2O^1 connectivity (**Figure 5.24b**). The crystal structure of **12** is similar to the reported structure by Blair *et al.* with small deviations in cell parameters and cell volume.[153]

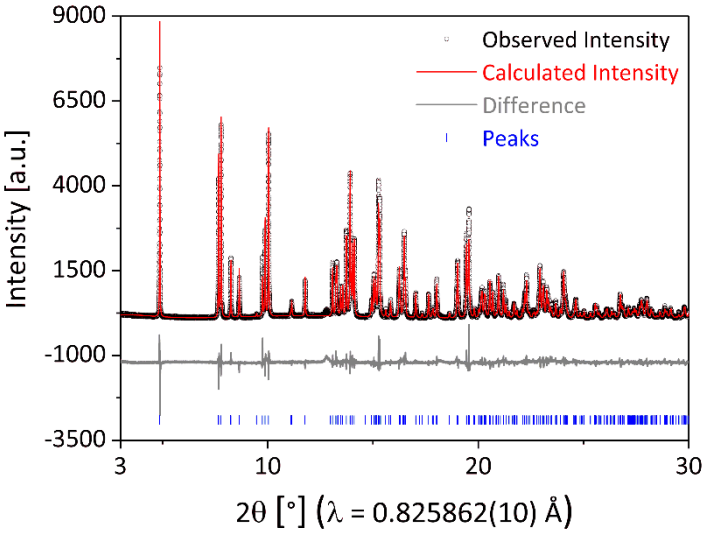

Figure 5.23: Rietveld refinement of the crystal structure of [Ba(*p*BDC-F_4)(H_2O)$_{0.5}$] (**12**).

The formation of [Ba(*p*BDC-F_4)(H_2O)$_{0.5}$] (**12**) was confirmed by different analytical methods including elemental analysis, thermal analysis, and the spectroscopic methods; MAS NMR and FT-IR. The elemental analysis (given in **Table A.2**) indicates the presence of only 0.2% of hydrogen (calculated 0.26%), this result is below the detection limit and does not confirm the presence of crystal water in **12**. The measured carbon ratio is 24.5% (calculated: 25.1%).

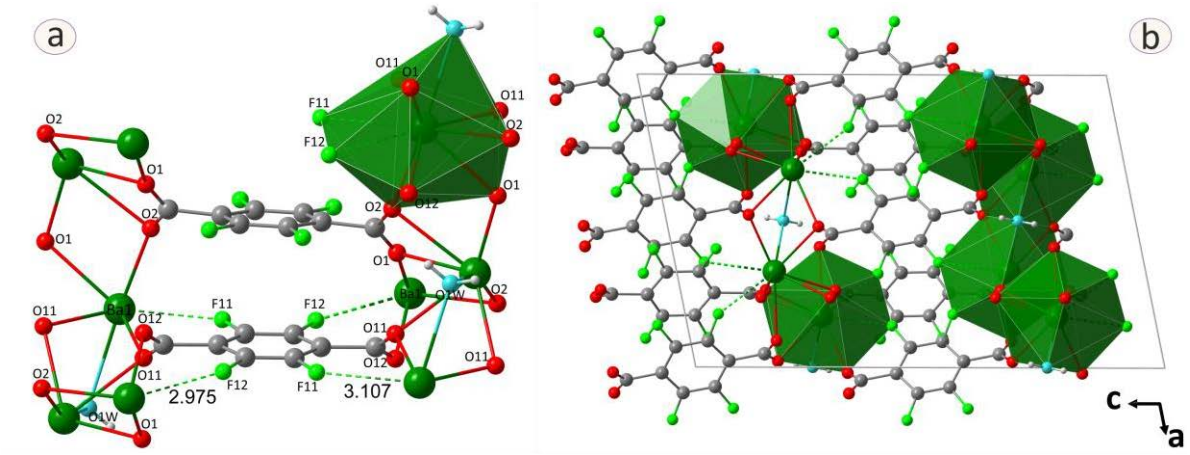

Figure 5.24: Crystal structure of [Ba(*p*BDC-F_4)(H_2O)$_{0.5}$] (**12**). (a) The coordination modes of the organic linker and the local coordination environment around Ba atom (All Ba^{2+}-ions are (8+1)-fold coordinated. Only one $M^{II}O_8(F_2)$ polyhedron is shown for clarity). The $M^{II}O_8$ (F_2) polyhedron comprises one water-oxygen atom (O1w), seven oxygen atoms from six (*p*BDC-F_4)$^{2-}$ anions (O1, O1', O2, O2', O11, O11', O12) and two Ba···F short distances (dashed lines) of 3.107 and 2.975 Å (F11, F12). (b) In the 2D-inorganic chains, Ba ions are separated via carboxylate- and water oxygen atoms; Ba-(O1w, O11)-Ba = 4.372(5) Å, Ba-(O1,O2)-Ba = 4.520(5) Å. Chains are bridged via ligand anions to form the 3D-crystal structure along the crystallographic b-axis. **Color code*: Metal (green), carbon (Grey), oxygen (red), fluorine (bright green), and hydrogen (light grey).

The thermoanalytical curves (**Figure 5.25**) show a mass loss of -39.8% at 243 °C which suggests that the strongly bridged water molecule is liberated within the decomposition process.

The MAS NMR spectra of [Ba(*p*BDC-F_4)(H_2O)$_{0.5}$] (**12**) (**Figure 5.26**) support the different structural properties of **12** in comparison with compounds **1** and **2** (**Figure 5.4**). The comparatively narrow signal at a chemical shift 4.4 ppm in the ^{1}H MAS NMR spectrum (**Figure 5.26a**) indicates the presence of water. In the ^{1}H→^{13}C CP MAS NMR spectrum (**Figure 5.26b**), the broad signal of the two carboxylic groups (known from the crystal structures) is almost at the same position as for the precursor H_2*p*BDC-F_4 at δ = 165 ppm (**Figure 5.4b**).

The signal assigned to carbon in the aromatic rings in compound **12** has a chemical shift of 119 ppm. The two fluorine signals at δ = -140 ppm and δ = -143 ppm in addition to the peak at δ = -135 ppm in the ^{19}F MAS NMR spectrum (**Figure 5.26c**) refer at least to three

crystallographic positions of fluorine atoms. The fourth fluorine atom known in the crystal structure is hidden by one of the broad fluorine signals.

The IR spectrum of compound **12** shown in **Figure 5.5** (green spectrum) depicts the vibration bands of water at the surface at 3443 cm^{-1}. The shoulder at 3343 cm^{-1} is assigned to the contribution of the crystal water known from the structure of **12**. In the lower wavenumber region, the weak vibration bands at 1266 cm^{-1} refer to C-O stretching. The vibration of the deprotonated carboxylate appears at 1604 cm^{-1}. The vibration band assigned to the C-F stretching vibration is shifted to 987 cm^{-1}.

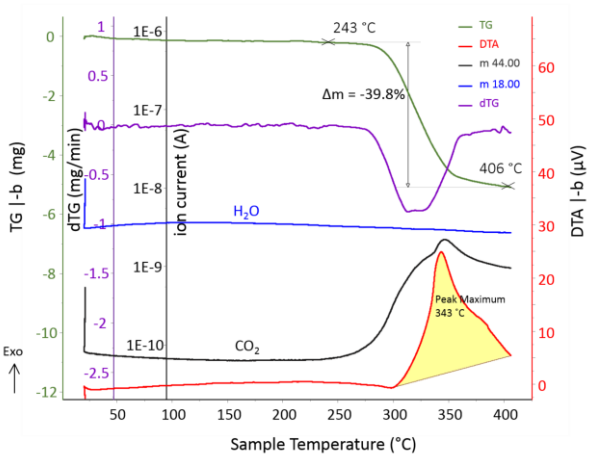

Figure 5.25: Thermoanalytical curves of [Ba(*p*BDC-F_4)(H_2O)$_{0.5}$] (**12**).

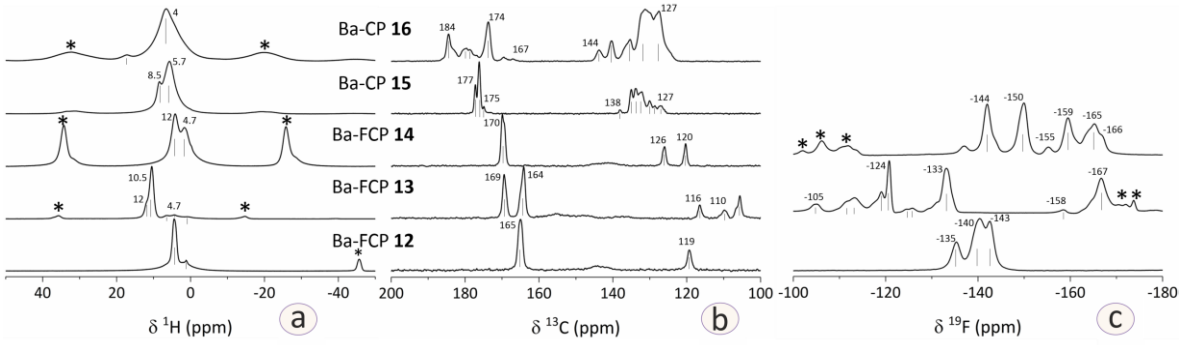

Figure 5.26: MAS NMR spectra of compounds [Ba(*p*BDC-F_4)(H_2O)$_{0.5}$] (**12**), [Ba(*m*BDC-F_4)(H_2O)$_{0.5}$] (**13**), [Ba(*o*BDC-F_4)(H_2O)$_{1.5}$] (**14**), [Ba(*m*BDC)(H_2O)$_{2.5}$] (**15**), [Ba(*o*BDC-F_4)(H_2O)$_1$] (**16**). (a) ^1H MAS NMR spectra. ν_{rot} = 10 KHz. (b) $^1H \rightarrow ^{13}C$ CP MAS NMR spectra. ν_{rot} = 10 KHz, contact time is 10 ms. (c) ^{19}F MAS NMR spectra. ν_{rot} = 20 KHz. Spinning sidebands (*).

Ba-CPs based on dicarboxylate aryls were reported. For example, Lo *et al*. synthesized a 3D-Ba-terephthalate.[156] The formed compound was free of coordinating water molecules, although the synthesis was processed under aqueous condition. A water-free Ba-terephthalate was also obtained mechanochemically by milling terephthalic acid (H_2*p*BDC) with $Ba(OH)_2$ or $Ba(OH)_2 \cdot H_2O$ while a hydrated barium compound [Ba(*p*BDC)(H_2O)$_{2(1.5)}$] was obtained by using $Ba(OH)_2 \cdot 8H_2O$ as an inorganic source.[83]

The SEM images of compounds **1**, **2** (**Figure 5.7a-b**) and **12** (**Figure 5.32a**) depict similar morphology, plate-like structures. These compounds comprise small surface areas.

In summary, Ba-tetrafluoroterephthalate **12** was synthesized by milling H_2*p*BDC-F_4 and Ba-hydroxides that vary in their water contents. Compound **12** crystallizes as 3D-CP and exhibits high thermal stability.

5.3.3. Ba-Tetrafluoroisophthalate [Ba(*m*BDC-F_4)$(H_2O)_{0.5}$]

The estimation of carbon ratio in the Ba-containing samples was difficult. The calculated H% for a half water molecule in **13** is 0.26% which is slightly higher than the measured one (0.2%). The measured fluorine content was below the expected ratio due to the difficult splitting of C–F bond in the aromatic ring after the transformation of the powder sample into a soluble form for fluorine detection. The thermoanalytical curves of compound **13** are shown in **Figure 5.27**. The TG curve indicates a small mass loss -0.7% up to 218 ˚C. This mass loss could be related to the liberation of fractions of water. The mass loss of -28.7% at the temperature range between 218 ˚C and 328 ˚C is supplemented with the release of CO_2 (peak maximum at 317 ˚C). Despite the tiny mass loss of -0.7%, there is not enough indication for the presence of crystal water. A mass loss corresponding to water is noticed along with the release of CO_2 between 328 ˚C and 359 ˚C (peak maximum at 340 ˚C). This late liberation of water could indicate for strongly bridged water within the crystal structure of **13**.

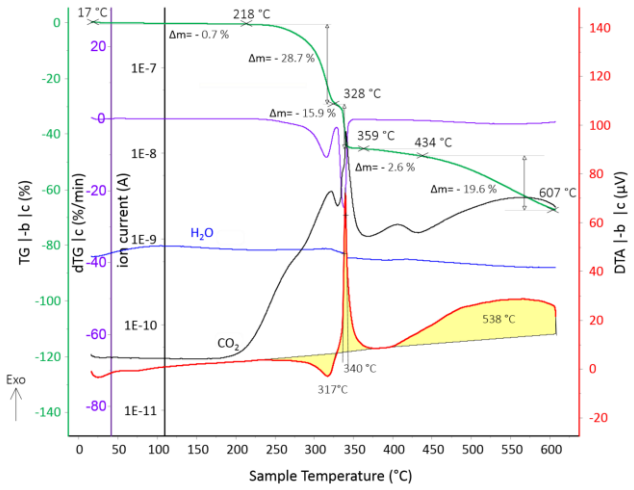

Figure 5.27: Thermoanalytical curves of [Ba(*m*BDC-F_4)$(H_2O)_{0.5}$] (**13**).

In the ^{1}H MAS NMR spectra, the two signals belonging to the protons of the two carboxylic groups at δ = 13.4 and 7.6 ppm in the spectrum of the organic ligand H_2*m*BDC-F_4 (**Figure 5.4a**), (black spectrum) disappear in the spectrum of compound **13** (**Figure 5.26a**). The latter spectrum depicts a comparatively narrow signal at a chemical shift of 10.5 ppm and a shoulder at δ = 12 ppm in addition to small signals at δ = 6.8 and 4.7 ppm. The former narrow signal

indicates the existence of strongly bridged protons. The two latter signals at δ = 6.8 and 4.7 ppm support the presence of additional less bridged protons and water in the crystal structure of **13**. This assumption together with the results from elemental analysis and ATR-IR spectrum indicate the presence of -at least- a half crystal water molecule within the crystal structure of **13**.

The $^{1}H \rightarrow ^{13}C$ CP MAS NMR spectrum of H_2*m*BDC-F_4 (**Figure 5.26b**, black spectrum) depicts two signals belong to the carboxylic groups (at δ = 166 and 165 ppm). These two signals are shifted to δ = 169 and 164 ppm in the spectrum of compound **13** (**Figure 5.26b**) and indicate the coordination between carboxylate anions and Ba-ions. Moreover, the pronounced separation between the two signals (δ = 5 ppm) compared to the organic ligand (separation is about 1 ppm) indicates the participation of carboxylate groups in the coordination system of **13**. In the latter spectrum, four carbon sites in the aromatic ring are resolved at δ = 116, 110, and 106 ppm, and in addition to the shoulder at δ = 106.5 ppm. The ^{19}F MAS NMR spectrum of H_2*m*BDC-F_4 (**Figure 5.4c**, black spectrum) depicts four fluorine signals at δ = -114, -121, -124, and -165 ppm corresponding to the four fluorine positions known from the crystal structure (Refcode: ODUSEM).[180] Nine fluorine positions are resolved in the ^{19}F MAS NMR spectrum of compound **13** (**Figure 5.26c**) at δ = -105, -112, -119, -121, -124, -126, -133, -158, and -167 ppm.

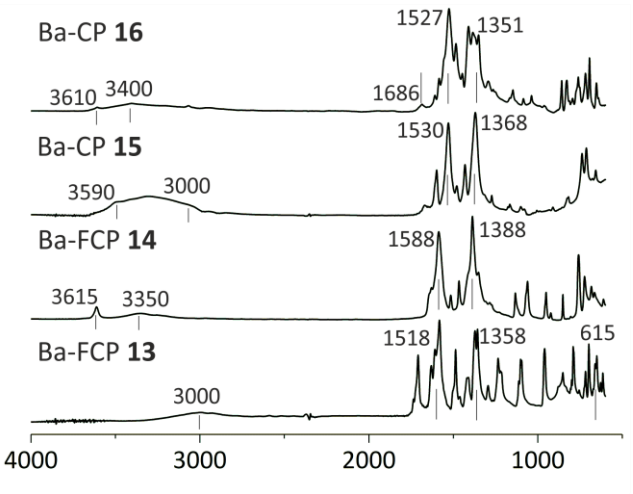

Figure 5.28: ATR-IR spectra of compounds [Ba(*m*BDC-F_4)$(H_2O)_{0.5}$] (**13**), [Ba(*o*BDC-F_4)$(H_2O)_{1.5}$] (**14**), [Ba(*m*BDC)$(H_2O)_{2.5}$] (**15**), and [Ba(*o*BDC)$(H_2O)_1$] (**16**).

The ATR-IR spectrum (**Figure 5.28**) confirms the formation of the barium carboxylate and the presence of a small amount of water. Ba-O(carboxylate) is indicated by the vibrational bands at 615 cm^{-1}. The bands assigned to the carboxylate stretching appear at 1583 cm^{-1} for asymmetric stretching and 1358 cm^{-1} for symmetric stretching. The separation (Δ_{a-s}) between asymmetric (ν_{as}) and symmetric (ν_s) stretching of carboxylate are about 225 cm^{-1}. The separation is attributed to the multi-dentate mode of carboxylate groups in **13**.[73,203]

The broad contribution around 3000 cm^{-1} indicates the presence of water molecules and the expected formation of HBN along the crystal structure of **13**.[148] Moreover, the carboxylate stretching separation (Δ_{a-s}) and the vibrational band assigned to water molecules in ATR-IR spectrum of **13** are very similar to those from Ca- and Sr-tetrafluoroisophthalates (**3**,**4**). The latter crystallize isomorphously and comprise three crystal water molecules. In the latter structures, the organic linker show multidentate coordination modes of carboxylic groups.[88] Compound **13** exhibits a small surface area (12.5 m^2/g). Even after treatment of the samples at 200 ˚C and 240 ˚C, the measured specific areas remain within the same range; 13.6 m^2/g and 15.1 m^2/g, respectively. SEM images of compound **13** (**Figure 5.32b**) depict similar morphology FCPs based on tetrafluoroterephthalate and tetrafluoroisophthalate (plate-like structures).[87,88] The *ab initio* structure determination of **13** was not successful. The growth of crystals from the powder product failed due to the poor solubility in different organic solvents including ethanol, acetone, DMF, or in a mixture of these solvents.

In summary, Ba-tetrafluoroisophthalate **13** obtained by milling contains -at least- a half crystal water molecule. The results from MAS NMR and ATR-IR spectroscopies are comparable to those of Ca- and Sr-tetrafluorisophthalates and suggest the presence of strongly bridged water species. Compound **13** exhibits small surface area even after treatment at different temperatures. The dehydrated sample is thermally stable up to 220 ˚C.

5.3.4. Ba-Tetrafluorophthalate [Ba(*o*BDC-F_4)(H_2O)$_{1.5}$]

The formation of the hydrated compound **14** was confirmed by the results of the elemental analysis (**Table A.2**) and thermal analysis (**Figure 5.29**). The measured carbon, hydrogen, and fluorine contents indicate that compound **14** contains 1.5H_2O molecules. The thermoanalytical curves depict a mass loss of -4.3% up to 193 ˚C belong to the liberation of one water molecule (Calc. 4.6%). The liberation is followed by a mass loss

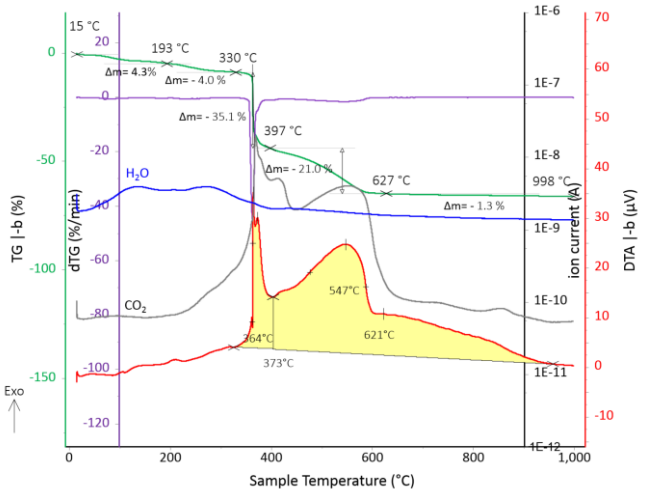

Figure 5.29: Thermoanalytical curves of [Ba(*o*BDC-F_4)(H_2O)$_{1.5}$] (**14**).

of -4.0% between 193 ˚C and 330 ˚C belong to the continued liberation of water along with a release of CO_2. A part of the latter belongs at least to a half water molecule (Calc. 2.35%). The decomposition of the framework continues with a massive mass loss of -35.1% between 330 and 397 ˚C.

The ^{1}H MAS NMR spectrum of compound **14** (**Figure 5.26a**) indicates the presence of crystal water by the signal at a chemical shift of 4 ppm. The $^{1}H \rightarrow ^{13}C$ CP MAS NMR spectrum of the organic ligand (**Figure 5.4b**, black spectrum) depicts two signals at δ = 175, and 163 ppm belong to the two carboxylic groups. The spectrum of compound **14** depicts only one signal at δ = 170 ppm with a small shoulder belonging to carboxylate carbon atoms which suggests that both carboxylate groups have almost the same reaction mode in their coordination to Ba-atoms. Two carbon sites in the aromatic ring could be identified in both spectra at δ = 118 and 113 ppm for the organic ligand and δ = 126 and 120 ppm for compound **14**. The ^{19}F MAS NMR spectrum of H_2*o*BDC-F_4 (**Figure 5.4c**, black spectrum) depicts fluorine signals at δ = -132, -138. -147, and -155 ppm is corresponding to the four fluorine positions known from the crystal structure (Refcode: BOLNAR).[181] Seven fluorine sites for compound **14** (**Figure 5.26c**) are resolved at δ = -137, -142, -150, -155, -159, -165, and the shoulder at -166 ppm.

The ATR-IR spectrum (**Figure 5.28**) depicts vibrational bands assigned to the carboxylate stretching at 1588 cm^{-1} for asymmetric stretching and 1388 cm^{-1} for symmetric stretching. The separation between asymmetric (ν_{as}) and symmetric (ν_s) stretching of carboxylate groups is about 200 cm^{-1}. The broad contributions above 3000 cm^{-1} are attributed to the presence of different types of water molecules and the formation of hydrogen-bonding network (HBN) along the crystal structures.[148] The broad contributions around 3350 cm^{-1} are assigned to the HBNs within the crystal lattices of **14**. The band at 3615 cm^{-1} indicates that some of the water molecules do not participate in the HBNs.

The hydrated compound **14** exhibits a small surface area (3.9 m^2/g) which slightly increases after treatment of samples at 200 ˚C and 250 ˚C to be 5.5 m^2/g and 7.6 m^2/g, respectively. One crystal structure of Ba-CP based on tetrafluorophthalic acid was reported by Coles and co-workers (Refcode: HUFLEB).[140] The crystal structure contains two Ba-bound water molecules and a pyridine molecule. Ba has a coordination number of nine.

In summary, Ba-based tetrafluorophthalate was obtained by milling. [Ba(*o*BDC-F_4)$(H_2O)_{1.5}$] (**14**) contains a higher content of water compared to compound **12** and **13**. The presence of water species within the crystal structure of **14** was confirmed by the results from MAS NMR and ATR-IR spectra. The water content was quantified via elemental analysis and thermal analysis. The water-free framework of **14** is thermally stable up to about 300 ˚C which is higher than compound **14**. The latter begins to decompose around 220 ˚C.

5.3.5. Ba-Isophthalate [Ba(*m*BDC)$(H_2O)_{2.5}$]

The measured hydrogen ratio is 2.7% and suggests that compound **15** contains 2.5H_2O molecules (calc. H% is 2.6%). The thermoanalytical curves confirm that compound **15** is hydrated (**Figure 5.30**). The thermogravimetric (TG) curve begins with a tiny mass loss of 0.6% in the temperature range between 19 ˚C and 67 ˚C. This step is followed by two consecutive mass losses of 3.8% and 8.6% at 120 ˚C and 194 ˚C, respectively. The total mass loss is 13% which corresponds to 2.5H_2O molecules (calculated 13%). The mass loss of 1.8% between 194 ˚C and 380 ˚C is related to residues of water in addition to the release of fractions from CO_2. The separation between the release of water and CO_2 in the latter step is difficult to be quantified. The decomposition of the framework [Ba(*m*BDC)] continues with two convective mass losses of -1.3% and -17.3% in the temperature range between 380 ˚C and 601 ˚C.

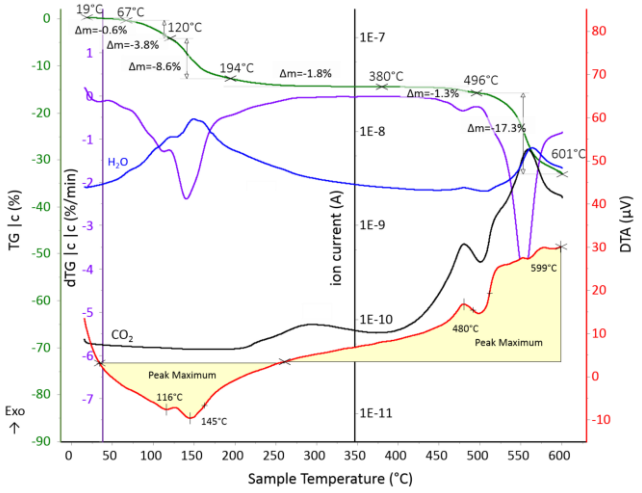

Figure 5.30: Thermoanalytical curves of [Ba(*m*BDC)$(H_2O)_{2.5}$] (**15**).

In the ATR-IR spectrum of **15**, the formation of Ba-O (carboxylate) is indicated by the vibration at 658 cm^{-1} (**Figure 5.28)**. The vibrational bands assigned to the carboxylate stretching are at 1530 cm^{-1} for asymmetric stretching and at 1368 cm^{-1} for symmetric stretching. The separation between the two vibrational modes is about 162 cm^{-1}. The broad contribution

in the range between 3590 and 3000 cm^{-1} indicates the presence of different types of water in the crystal structure of **15**.

The ^{1}H MAS NMR spectrum of **15** (**Figure 5.26a**) provides evidence for the presence of water molecules by the broad contribution at a chemical shift of 5.7 ppm which is a typical for coordinating water. The chemical shift at 8.5 ppm is mainly due to bridged protons and water-hydroxyl groups within the crystal structure. The $^{1}H \rightarrow ^{13}C$ CP MAS NMR spectrum (**Figure 5.26b**) shows different contributions at δ = 177, 176, and 175 ppm assigned to different types of carbon atoms in carboxylate groups and indicate the rule of carboxylate groups within the coordination environment. The signals at the chemical shifts between 138 and 127 ppm assign to several carbon sites in the aromatic ring.

Compound **15** exhibits a very small surface area (2.2 m^2/g). Even after thermal treatment, the BET specific surface remains unchanged. This result is comparable to Ca-isophthalate (S_{BET} = 3 - 4 m^2/g). The crystal structure of **15** was not solved from PXRD data. The crystallization of the powder obtained by milling in different solvents forms very poor crystals that are not sufficient for structure solution.

In summary, compound **15** was obtained by milling $Ba(OH)_2 \cdot 8H_2O$ and H_2*m*BDC. The new compound is hydrated. Thermal analysis indicates the presence of at least $2.5H_2O$ within the crystal structure of **15**. The dehydrated framework of **15** is stable up to 300 °C. Both hydrated and dehydrated samples of **15** exhibit very small surface areas.

5.3.6. Ba-Phthalate [Ba(*o*BDC)(H_2O)]

The formation of the hydrated compound **16** was confirmed by the results of the elemental analysis (**Table A.2**) and thermal analysis (**Figure 5.31**). The measured elemental carbon and hydrogen contents are 29% and 1.6%, respectively and point to that compound **16** contain one water molecule. The thermoanalytical curves depict three consecutive weight losses -2.5%, -1.1%, and -2.4% in the temperature range of

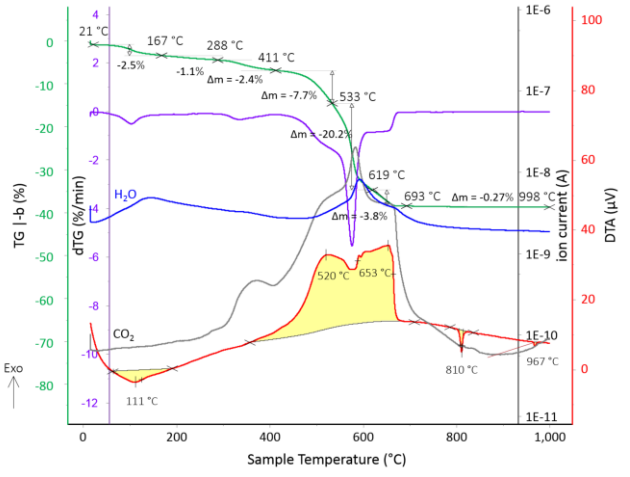

Figure 5.31: Thermoanalytical curves of [Ba(*o*BDC)(H_2O)] (**16**).

21 ˚C - 411 ˚C. These steps correspond to the liberation of one water molecule (calc. 5.6%). The latter step also comprises a release of CO_2. The decomposition of the already water-free framework continues with a mass loss of -7.7% up to 533 ˚C. This step is followed by a massive mass loss of -20.2%. The ^{1}H MAS NMR spectrum of compound **16** (**Figure 5.26a**) depicts a broad signal at δ = 6.6 ppm corresponding to strongly bridged protons in the benzene ring. The ^{1}H→^{13}C CP MAS NMR spectrum of the organic ligand H$_2$*o*BDC (**Figure 5.16b**) depicts two signals at δ = 173, and 132 ppm belong to carboxylic group and carbon in the aromatic ring, respectively. For compound **16** (**Figure 5.26b**), five carboxylates sites could be identified at δ = 184, 180, 174, 170, and 167 ppm and five carbon positions in the aromatic ring are resolved at δ = 144, 140, 135, 131, and 127 ppm.

In ATR-IR spectrum (**Figure 5.28**), the vibrational bands assigned to the carboxylate stretching are at 1527 cm^{-1} for asymmetric stretching and at 1410, 1383, and 1351 cm^{-1} for symmetric stretching. The separations between the two vibrational modes are about 117, 144, and 176 cm^{-1} and indicate the multidentate modes of carboxylic groups in the organic linker. Several contributions are assigned to the presence of water within the crystal structure of **16**. These contributions include the vibrational assigned to water bending (at 1686 cm^{-1}), the broad contribution around 3400 cm^{-1} which can be assigned to the presence of HBN within the crystal lattice, and OH stretching (at 3610 cm^{-1}) which indicate that some water molecules do not participate in the HBN.

Compound **16** exhibits a very small surface area (4.8 m^2/g). Even after treatment at different temperatures, the BET specific surface remains unchanged. In contrast to the dehydrated samples of Ca-phthalate (**10-H$_2$O**) which depicts a larger surface area (14.3 m^2/g) than the hydrated sample **10** (4.2 m^2/g).[204]

The structure determination and crystallization of **16** were not successful. The crystallization of the powder obtained by milling in different solvents resulted in very poor crystals. Few Ba-CPs based on phthalic acid and its derivatives are known from literature including the reported crystal structure by Zhang *et al*.[146,207–209] These compounds were synthesized via solvothermal treatments. In their crystal structures, the coordination number of the Ba atoms vary between 8 and 10.

In summary, Ba(*o*BDC)(H$_2$O)$_1$] **16** obtained by milling is different from the reported Ba-phthalates. Compound **16** shows high thermal stability. The dehydrated framework is

stable up to 400 °C which is comparable to dehydrated Ca-phthalate but unlike the dehydrated samples of the fluorinated counterpart **14** which begins to decompose around 220 °C. However, the dehydrated samples of the fluorine-free compounds **15** and **16** depict higher thermal stabilities than their fluorinated counterparts **13** and **14**. The hydrated and dehydrated samples of compound **16** exhibit small surface areas.

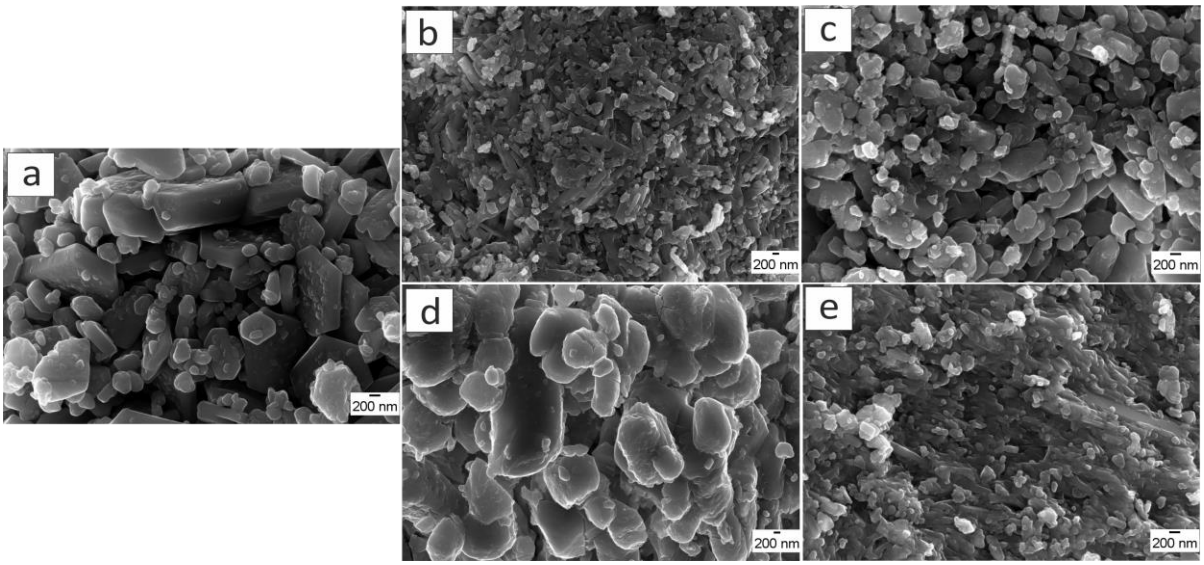

Figure 5.32: SEM images of Ba-CPs. (a) [Ba(*p*BDC-F_4)(H_2O)$_{0.5}$] (**12**), (b) [Ba(*m*BDC-F_4)(H_2O)$_{0.5}$] (**13**), (c) [Ba(*o*BDC-F_4)(H_2O)$_{1.5}$] (**14**), (d) [Ba(*m*BDC)(H_2O)$_{2.5}$] (**15**), (e) [Ba(*o*BDC)(H_2O)$_1$] (**16**).

5.3.7. Comparison and Conclusion

The mechanochemical syntheses and characterization of new coordination polymers obtained by milling $Ba(OH)_2{\cdot}8H_2O$ with different ligands are described. The organic linkers include the perfluorinated ligands H_2*p*BDC-F_4, H_2*m*BDC-F_4, and H_2*o*BDC-F_4, and the nonfluorinated analogs H_2*m*BDC, and H_2*o*BDC (**Figure 5.33**). The variation of the water content in the inorganic precursors by using $Ba(OH)_2{\cdot}8H_2O$ (including crystal water), $Ba(OH)_2$ or additional external water influences the final products obtained by milling. For the fluorinated CPs, the water content affects only the crystallinity of the final products but leads to the formation of the same compound. The best results are achieved when $Ba(OH)_2{\cdot}8H_2O$ is used as an inorganic precursor (crystal water) rather than using $Ba(OH)_2$ or $Ba(OH)_2$ + H_2O (external water). For the fluorine-free CPs, the coordination environments of final products are strongly influenced by the variation of water content in the inorganic

precursors and lead to the formation of different compounds. In this work, we focused on $Ba(OH)_2 \cdot 8H_2O$ as the metal source.

The new compounds are all hydrated but vary in their water content. The presence of water molecules embedded within the crystal structures and the coordination systems were investigated by the elemental analysis, MAS NMR, and ATR-IR spectra. The number of water molecules was quantified via the measured thermoanalytical curves. These compounds depict different thermal behavior. The fluorinated compounds **12, 13,** and **14** are stable up to 300 °C, but the fluorine-free frameworks **15** and **16** depict higher thermal stabilities and begin to decompose around 400 °C or even higher. The hydrated compounds $[Ba(pBDC\text{-}F_4)(H_2O)_{0.5}]$ (**12**), $[Ba(mBDC\text{-}F_4)(H_2O)_{0.5}]$ (**13**), $[Ba(oBDC\text{-}F_4)(H_2O)_{1.5}]$ (**14**), $[Ba(mBDC)(H_2O)_{2.5}]$ (**15**), and $[Ba(oBDC)(H_2O)_1]$ (**16**) exhibit small surface areas. The surface areas remain almost unchanged for the dehydrated samples.

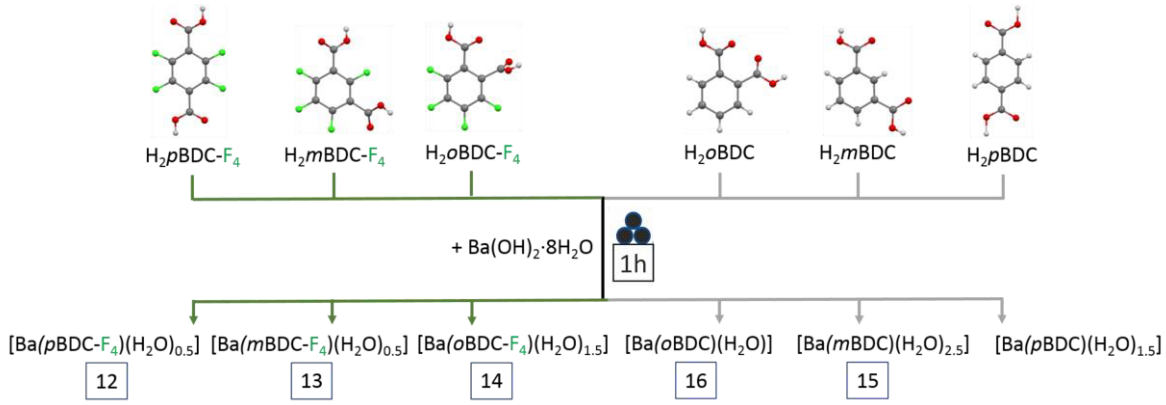

Figure 5.33: Mechanochemical synthesis of Ba-FCPs and CPs based on tetrafluorobenzene-dicarboxylic systems ($H_2BDC\text{-}F_4$) and their fluorine-free analogs (H_2BDC).

5.4. Comparative Study: Fluorinated and Fluorine-Free Benzene-Dicarboxylate Systems

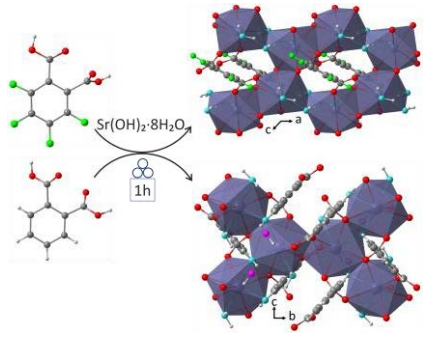

i. A. Al-Terkawi, G. Scholz, C. Prinz, A. Zimathies, F. Emmerling, E. Kemnitz. *CrystEngComm.* **2018**, *20*, 946-961.

ii. A. Al-Terkawi, G. Scholz, F. Emmerling, E. Kemnitz. (*Dalton Trans., accepted*)

Scientific Aspects:

- The water content of an inorganic sample influences only the crystallinity of FCPs obtained by milling. In contrast, both of crystallinity and the coordination system of fluorine-free CPs are influenced by the variations in water introduced to milling.
- Ca- and Sr-FCPs crystallize isomorphously in their coordination to a respective perfluorinated ligand.
- Like the hydrated CPs of Ca- and Sr-terephthalates, the hydrated Ca- and Sr-isophthalates crystallize isomorphously. Differently, Ca-phthalate is a monohydrate while Sr-phthalate is a trihydrate.
- The presence of fluorine influences the torsion angles of carboxylate groups concerning the planar ring and subsequently the structural properties of the resulting FCPS.
- Ba-FCPs and Ba-CPs vary in their properties based on the nature of an organic linker and the presence of fluorine atoms.
- The fluorine-containing frameworks are stable up to 300 °C. The fluorine-free CPs begin to decompose at 400 °C.
- The hydrated samples exhibit small specific surfaces which could increase after thermal treatment.

5.4.1. The Dual Role of Water

The millings of Ca-, Sr-, and Ba-hydroxides varying in their water contents with the isomers of tetrafluorobenzene-dicarboxylic acid ($H_2BDC\text{-}F_4$) lead to the formation of the same compound of a given metal cation regardless of the different water content in the inorganic precursors. The source of water can be internal (crystal water) via using the M^{II}-hydroxide octahydrates or external by adding a small amount of water to the M^{II}-hydroxides (**Scheme 4.1**). Here, the variations of water content influence at least the crystallinity of the products. The highest crystallinity of products is achieved when $Ca(OH)_2$ + H_2O, $Sr(OH)_2{\cdot}8H_2O$, or $Ba(OH)_2{\cdot}8H_2O$ are used as inorganic sources. These findings are based on the synthesis of Ca-, Sr-, and Ba-FCPs based on tetrafluoroterephthalic acid (H_2*p*$BDC\text{-}F_4$), tetrafluoroisophthalic acid (H_2*m*$BDC\text{-}F_4$), and tetrafluorophthalic acid (H_2*o*$BDC\text{-}F_4$).[87,88,90,200,206]

Against this background, the variation of water content mainly influences both crystallinity and coordination systems of products produced by milling M^{II}-hydroxides and the fluorine-free benzene-dicarboxylic acids (H_2BDC).[83,200,204,206] In this work, the focus is on the products obtained by using $Ca(OH)_2$ + 130 µl H_2O, $Sr(OH)_2{\cdot}8H_2O$, and $Ba(OH)_2{\cdot}8H_2O$ as metal sources (**Scheme 4.2**).[90,204,206]

The role of water (as a liquid) during milling enhances the molecular mobility of reactants, accelerates the milling process, and subsequently improves the crystallinity of the resulting polycrystalline powder products. Moreover, water (as a ligand) plays a role for stabilizing the crystal structures in both fluorinated and fluorine-free compounds to complete the local coordination environment of the metal (**Figure 5.1c**), bridge metal centers in chains (**Figure 5.1a**), or as a cocrystallized ligand that forms hydrogen bridges (**Figure 5.1b**).

5.4.2. Structural Trends

Structures of FCPs keep their stabilities even via using different water content during the milling process. The same coordination system for a given metal cation and a perfluorinated ligand was constructed regardless of the water variations during milling. In the nonfluorinated systems, the water content during milling could influence the number of metal-bound water molecules.[83,200,204,206] The stabilities of FCPs under humid conditions can be explained by the nature of the perfluorinated linkers that form high hydrophobic channels or cavities within the FCPs and do not allow empty rooms or additional coordination sites for

water ligands. Moreover, these FCPs are stable in air and maintain their structural integrity at ambient conditions up to 250 °C (**Section 5.1**).

In their coordination to a perfluorinated ligand, Ca- and Sr-based FCPs depict similar structural properties (**Figure 5.1**). In detail, Ca- and Sr-tetrafluoroterephthalates (**1**,**2**) crystallize isomorphously in the monoclinic $P2_1/m$ as 2D-CPs (**Figure 5.1a**).[87] Both crystal structures comprise four metal-bound water molecules with I^1O^1 connectivity. Ca- and Sr-tetrafluoroisophthalates (**3**,**4**) crystallize in the orthorhombic $P2_12_12_1$ space group as 3D-FCPs and exhibit hybrid I^1O^2 connectivity where the 1D-inorganic chains are cross-linked by the organic linkers.[88] Both crystal structures contain two metal-bound water ligands and one cocrystallized water molecule (**Figure 5.1b**). Ca- and Sr-tetrafluorophthalates (**5**,**6**) comprise two metal-bound water molecules in their crystal structures. The latter crystallizes in the monoclinic $P2_1/c$ system as a 2D-FCP with a classification of I^2O^0 (**Figure 5.1c**).[90] All these compounds were prepared under the same conditions. Here, structural properties are determined by the geometries of organic linkers in addition to the replacement of hydrogen by fluorine atoms in the perfluorinated ligands.

For the nonfluorinated counterparts, all Ca-based CPs obtained by the milling of $Ca(OH)_2$ + 130 µl H_2O with terephthalic acid, isophthalic acid, or phthalic acid are similar to reported crystal structures via hydrothermal treatments.[204] Sr-based CPs obtained by milling are new.[83,84,90,200] The crystal structures of the hydrated Ca- and Sr-CPs based on terephthalic (**Figure 5.9b**) and isophthalic acids (**Figure 5.10b**) reveal 1D inorganic connectivity (I^1O^0) that extend to 3D networks via hydrogen bonds.[84,200,204] The hydrated Ca-phthalate consists of 1D inorganic chains which are linked by an organic linker to form the final 2D-crystal structure with the hybrid inorganic-organic I^1O^1 connectivity (**Figure 5.11b**).[204] New dehydrated phases of Ca-, Sr-terephthalate, and Ca-phthalate were obtained in reversible phase transition processes by thermal post-treatment of the hydrated samples. The crystal structures of dehydrated Ca- and Sr-terephthalates (3D-CPs, I^2O^1) and Ca-phthalate (2D-CP, I^2O^0) are shown in **Figure 5.9c** and **Figure 5.11c**.

Compared to their nonfluorinated counterparts, the Ca- and Sr-FCPs show higher dimensionalities and hybrid inorganic and organic connections (I^1O^1 and I^1O^2). An exception is recorded for the fluorinated and fluorine-free CPs that based on ortho-dicarboxylate

systems. Here, both Sr-based FCP and CP possess the same 2D inorganic I^2O^0 connectivity (**Figure 5.1c** and **Figure 5.12b**).[90]

FCPs and CPs obtained by milling are all hydrated. The number of coordinating water molecules varies depending on the geometry of the organic linker and the metal species. The highest number of coordinating water molecules is found in FCPS **1** and **2** (**Figure 5.3a**) where the respective metal cation coordinates to four water molecules (six bridging water molecules and one metal-bound water molecule in terminus). The structures of **1** and **2** also have the fewer number of coordinating carboxylate-oxygen anions (two oxygen atoms from two organic linkers). The lowest number of the coordinating water molecules is found in Ba-FCPs **12** where Ba ions are bridged by a water molecule (**Figure 5.24a**). The same compound depicts the highest number of coordinating carboxylate-oxygen ions (seven oxygen atoms from six *p*BDC-F_4^{2-} anions). Cocrystallized water molecules are found in the structures of **3**, **4**, **8**, and **11** (**Figure 5.3b** and **Figure 5.13b**). The presence of the coordinating, bridging, and cocrystallizing water molecules lead to the formation of hydrogen bonding networks that subsequently stabilize the structures and could assist in increasing the dimensionality of the coordination system.

The highest coordination number (C.N.) within these structures is nine (FCPS **1**, **2**, and Sr-CP **11**). The common C.N. is eight (six structures). The lowest C.N. of a central metal is seven in (Ca-phthalate **10**). The monoclinic system is dominating in these crystal structures except for **3** and **4** that crystallize in the orthorhombic system. The most common space group is $P2_1/c$ (**Table 5.1** and **Table 5.2**).

5.4.3. Effect of Geometries and Fluorination of Organic Linkers

The substitutions of hydrogen atoms in benzene ring by fluorine atoms result in twisting of carboxylate groups by about 50-70° out the planar plane of the F-containing benzene ring. This twisting upon fluorination is attributable to the hydrophobic nature of fluorine atoms and the electrostatic repulsion between the highly electronegative fluorine atoms and the lone-pair electrons of carboxylate-oxygen atoms. Here the aromaticity of carboxylate groups decreases as a sequence of the electron-withdrawing nature of fluorine atoms.[197] In the fluorine-free ligands, the two carboxylate groups in terephthalic acid and isophthalic acid are nearly on the plane with the benzene ring. In phthalic acid, one is planar (with a torsion angle of 10°), the second has an off-planar orientation with a dihedral angle = 84° concerning

the benzene ring.[196] consequently, the presence of fluorine atoms plays a crucial role in increasing the dimensionality of the FCPs compared to their nonfluorinated counterparts. Furthermore, the difference within the FCPs or the CPs in their inorganic (I^n) and organic (O^m) connections is mainly attributed to the variety in geometries between the organic linkers and depending on the positions of the two carboxylate groups that occupy positions at 180° in the *para*-systems, 120° in the *meta*-systems, and 60° in the *ortho*-systems.

In their coordination with Ca^{2+}- and Sr^{2+}-ions, each of the two parallel carboxylic groups in *p*BDC-F_4^{2} anion act as a monodentate ligand and extend the 1D aqua-metallic polymeric chains into 2D layered structures (**Figure 5.1a** and **Figure 5.3a**).[87] The geometry of *m*BDC-F_4^{2-} anions plays a crucial role in extending the dimensionality of the resulting compound into 3D-CPs (**Figure 5.1c** and **Figure 5.3b**).[88] *o*BDC-F_4^{2} anions connect the metal polyhedra via the carboxylate oxygen ligands of the *ortho*-system and form 2D inorganic networks (**Figure 5.1c** and **Figure 5.3c**).[88,90]

In the fluorine-free counterparts, *p*BDC^{2-} anions chelate one metal and bridge another two via one carboxylate group and to form 1D-inorganic chains (**Figure 5.13a**). The angular linker *m*BDC^{2-} chelates two metals and bridge another two metals to form 1D-helices (**Figure 5.13c**). The two carboxylates in *ortho* positions allow *o*BDC^{2-} linker to chelate metal cations via two oxygen atoms from two carboxylates and extend the system into 2D-structure (**Figure 5.13d-f**). Coordination environments, coordination modes of the perfluorinated and nonfluorinated benzene-dicarboxylate anions, and crystal structures are depicted in **Figure 5.3**, **Figure 5.13**, and **Figure 5.24a**. The related structural properties and carboxylate torsion angles are summarized in **Table 5.3**.

5.4.4. Influence of Metal Cation Size

The alkaline earth metals (Mg, Ca, Sr, and Ba) were used in several studies to investigate the effect of the metal cation size on the structure and stability of extended hybrid materials of aryl-dicarboxylate frameworks.[146,210] Mg^{2+}-cations tend to have a six-fold coordinated environment. Sr^{2+}- and Ba^{2+}-cations are usually eight-fold coordinated, but the intermediate sized Ca^{2+}-cations can be six-, seven-, or even eight-fold coordinated. Also, eight, nine- and ten-fold coordinated Ba^{2+}-cations were reported.[146,150,153] The length of the M^{II}-O bond increases as the radius of the metal cation increases. Also, the M^{II}-O bond length increases by increasing the C.N. of the metal cation.[70,75] The binding mode of alkaline earth metals to

the aryl polycarboxylate anions confirms the predominant building block as a chain of metal centers bridged either by carboxylate moieties alone or by both carboxylate ligands and solvent molecules. All these samples described in the literature were prepared by solvothermal syntheses.

In the mechanochemically synthesized FCPs and CPs, Ca- and Sr-compounds crystallize isomorphously in their coordination with perfluorinated and fluorine-free benzene-dicarboxylic systems except for the phthalate system. The C.N. of Ca^{2+}-ions vary between seven (Ca-phthalate), eight (common), and nine (Ca-tetrafluoroterephthalate, Ca-isophthalate). C.N. of Sr^{2+}-ions is eight (common) or nine (Sr-tetrafluoroterephthalate, Sr-phthalate). The C.N. of nine is rarely described for Ca^{2+}-ions.[211] Though, only a few compounds with nine-fold coordination of Ca atoms are found in the literature.[147,148,212] Few compounds including the nine-fold coordination of strontium atoms were also reported.[58,213–215] The small difference in size between the Ca^{2+}-cation and the bigger Sr^{2+}-cation results in different M^{II}-O bond lengths in their coordination to BDC-F_4^{2-}, BDC^{2-} anions, and water molecules (**Table 5.1** and **Table 5.2**). Ba-tetrafluoroterephthalate (**12**) crystallizes as a 3D-FCP (**Figure 5.24**) which is different from the 2D-coordination systems in Ca- and Sr-tetrafluoroterephthalates (**Figure 5.1a**). Moreover, the bigger size of Ba^{2+}-cation allows interactions between the Ba^{2+}-ion and the nearby fluorine atoms.

5.4.5. Thermal Properties and Surface Areas

The FCPs and CPs exhibit high thermal stabilities. The liberation of crystal water molecules by the thermal post-treatment of the hydrated samples vary depending on the coordination systems. For example, the liberation of the strongly bridged water molecules in the FCPs **1**-**6** and CPs **8**-**9** took place along the release of CO_2 and indicating the decomposition of frameworks. The water-free frameworks are stable up to 300 °C in FCPs and up to 400 °C in the fluorine-free CPs.

The hydrated samples of FCPs-based on tetrafluorobenzene-dicarboxylates and CPs-based on benzene-dicarboxylates exhibit small surface areas which could slightly increase (as in Ca- and Sr- tetrafluoroisophthalates and Ca-phthalate).[88,90,204] The measured surface areas for Ca- and Sr-isophthalates and Sr-phthalate remain unchanged even after thermal treatment.[90,204] The BET surface areas and thermal stabilities for the hydrated and dehydrated samples of FCPs and CPs are compared in **Table 5.4**. These compounds have similar morphology as depicted in SEM images (**Figure 5.7**, **Figure 5.21**, and **Figure 5.32**).

Table 5.3: Structural properties of CPs based on tetrafluorobenzene-dicarboxylic acids and their nonfluorinated analogs. All compounds were synthesized via mechanochemical reactions. (HB: hydrogen bonds).

	Metal center	Crystal system	polyhedra	Cocrystallized H_2O	Connectivity (I^nO^m)	Dimensi-onality	bond type	Network	bond type (in the network)	Carboxylate torsion angles (°)
Fluorinated CPs										
$[M^{II}(p\text{BDC-}F_4)(H_2O)_4]$	Ca	Monoclinic, $P2_1/m$	$M^{II}O_9$ [2O(carboxyl), 7O[water)]	-	n=1, m=1	2D	$[M^{II}$–O(carboxyl) + $[M^{II}$–O(water)]	2D	+ HB	54.05(1)
	Sr									56.01(4)
$[Ba(p\text{BDC-}F_4)(H_2O)_{0.5}]$	Ba	Monoclinic, C2/c	$BaO_8(F_2)$ [7O(carboxyl), 1O[water)]	-	2, 1	3D	$[M^{II}$–O(carboxyl) + $[M^{II}$–O(water)]	3D	+ HB	33.88(8), 43.96(8)
$[M^{II}(m\text{BDC-}F_4)(H_2O)_3]$	Ca	Orthorhombic, $P2_12_12_1$	$M^{II}O_9$ [6O(carboxyl), 2O[water)]	1	1, 2	3D	$[M^{II}$–O(carboxyl)]	3D	+ HB	60.67(2), 75.01(2)
	Sr									67.06(2), 73.17(2)
$[M^{II}(o\text{BDC-}F_4)(H_2O)_2]$	(Ca) Sr	Monoclinic, $P2_1/c$	$M^{II}O_{(8+1)}$ [6O(carboxyl), 3O[water)]	-	2, 0	2D	$[M^{II}$–O(carboxyl) + $[M^{II}$–O(water)]	2D	+ HB	52.94(7), 69.56(9)
Nonfluorinated CPs										
$[M^{II}(p\text{BDC})(H_2O)_3]$	Ca	Monoclinic, $P2_1/c$	$M^{II}O_9$ [4O(carboxyl), 4O[water)]	-	1, 0	1D	$[M^{II}$–O(carboxyl) + $[M^{II}$–O(water)]	3D	via HB	4.14(4), 5.18(3)
	Sr									4.78(1), 11.99(1)
$[M^{II}(m\text{BDC})(H_2O)_{3.4}]$	Ca (Sr)	Monoclinic, C2/c	CaO_8 [6O(carboxyl), 2O[water)]	4	1, 0	1D	$[M^{II}$–O(carboxyl) + $[M^{II}$–O(water)]	3D	via HB	0.49(7), 1.98(7), 4.79(7), 5.66(7), 9.46(7), 8.52(7)

	Metal center	Crystal system	polyhedra	Cocrystallized H_2O	Connectivity (I^nO^m)	Dimensi-onality	bond type	Network	bond type (in the network)	Carboxylate torsion angles (°)
			CaO_9 [6O(carboxyl), 3O[water)]							
[Ca(*o*BDC)(H_2O)]	Ca	Monoclinic, $P2_1/c$	CaO_7 [6O(carboxyl), 1O[water)]	-	1, 1	2D	[M^{II}–O(carboxyl)]	2D	+ HB	32.78(2), 81.41(2)
[Sr(*o*BDC)(H_2O)$_3$]	Sr	Monoclinic, $P2_1/c$	$M^{II}O_9$ [6O(carboxyl), 3O[water)]	1	2, 0	2D	[M^{II}–O(carboxyl) + [M^{II}–O(water)]	2D	+ HB	11.46(1), 83.70(1)
Dehydrated CPs										
[M^{II}(*p*BDC)]	Ca	Monoclinic, C2/c	$M^{II}O_6$ [6O(carboxyl)]	-	2, 1	3D	[M^{II}– O(carboxyl)]	3D		4.54(1)
	Sr									9.13(1)
[Ca(*o*BDC)]	Ca	Monoclinic, $P2_1/c$	CaO_8 [8O(carboxyl]	-	2, 0	2D	[M^{II}–O(carboxyl)]	2D		47,45(5), 78.46(5)

Table 5.4: Thermal stabilities and BET surface areas (S_{BET} m^2/g) of Ca-, Sr-, and Ba-FCPs and CPs based on tetrafluorobenzene-dicarboxylic acids ($H_2BDC\text{-}F_4$) and their nonfluorinated analogs (H_2BDC). The samples were degassed for 24 h at room temperature and different temperatures. All samples were measured by liquid N_2.

CPs	S_{BET}	Liberation of water (°C)	stability of dehydrated samples (°C)	S_{BET} of dehydrated samples
[Ca(*p*BDC-F_4)$(H_2O)_4$] (**1**)	2.6 ± 0.02	23 – 250	250 – 300	-
[Sr(*p*BDC-F_4)$(H_2O)_4$] (**2**)	12.1 ± 0.1	23 – 260	260 – 300	-
[Ca(*m*BDC-F_4)$(H_2O)_3$] (**3**)	5.4 ± 0.04	23 – 280	280 – 300	12.9 ± 0.12
[Sr(*m*BDC-F_4)$(H_2O)_3$] (**4**)	3.1 ± 0.04	71 – 285	285 – 300	13.6 ± 0.02
[Ca(*o*BDC-F_4)$(H_2O)_2$] (**5**)	6.5 ± 0.04	23 – 290	290 – 300	43 ± 0.2
[Sr(*o*BDC-F_4)$(H_2O)_2$] (**6**)	5.6 ± 0.02	23 – 290	290 – 330	16.8 ± 0.1
[Ca(*p*BDC)$(H_2O)_3$] (**7**)	-	23 – 200	200 – 400	-
[Sr(*p*BDC)$(H_2O)_3$]	9.5	23 – 200	100 – 550	6.1
[Ca(*m*BDC)$(H_2O)_{3.4}$] (**8**)	3.3 ± 0.04	23 – 450	450 – 480	4.2 ± 0.02
[Sr(*m*BDC)$(H_2O)_{3.4}$] (**9**)	2.4 ± 0.06	23 – 420	420 – 420	2.2 ± 0.04
[Ca(*o*BDC)(H_2O)] (**10**)	4.2 ± 0.02	23 – 290	290 – 400	14.26 ± 0.08
[Sr(*o*BDC)$(H_2O)_3$] (**11**)	5.0 ± 0.05	55 – 180	180 – 420	4.08 ± 0.02
[Ba(*p*BDC-F_4)$(H_2O)_{0.5}$] (**12**)	5.3 ± 0.05	17 - 218	218 – 220	-
[Ba(*m*BDC-F_4)$(H_2O)_{0.5}$] (**13**)	12.5 ± 0.1	15 - 200	200 – 280	15.1 ± 0.1
[Ba(*o*BDC-F_4)$(H_2O)_{1.5}$] (**14**)	3.9 ± 0.01	19 - 194	200 – 300	7.6 ± 0.04
[Ba(*p*BDC)$(H_2O)_{1.5}$]	-	25 - 400	400 – 450	-
[Ba(*m*BDC)$(H_2O)_{2.5}$] (**15**)	2.2 ± 0.03	19 - 194	194 – 380	2.3 ± 0.02
[Ba(*o*BDC)(H_2O)] (**16**)	4.8 ± 0.02	21 - 411	400 – 420	4.8 ± 0.02

5.5. Ca-, Sr-, and Ba-Anthranilates: $[M^{II}(oABA)_2(H_2O)_n]$

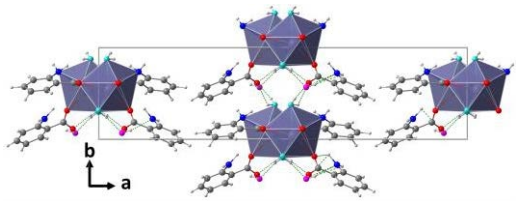

A. Al-Terkawi, G. Scholz, C. Prinz, F. Emmerling, E. Kemnitz. (*in preparation*).

Scientific Aspects:

- Mechanochemical synthesis and structural diversities of CPs based on AE metals and anthranilic acid are described
- Variation of the water content in inorganic sources is with little effect on the coordination systems of final products.
- C.N., connectivity, and the dimensionality of crystal structures are determined by metal cation sizes.
- Crystal water in the CPs based on the heavier metals (Sr and Ba) is involved in the bridging systems rather than only capping ligands (Ca-CP).
- $[Ca(oABA)_2(H_2O)_3]$ (**17**) crystallizes as a 1D-CP (Connectivity: I^0O^1).
- $[\{Sr(oABA)_2(H_2O)_2\}\cdot H_2O]$ (**18**) crystallizes as a 1D-CP (Connectivity: I^1O^0).
- $[Ba(oABA)_2(H_2O)]$ (**19**) crystallizes as a 2D-CP (Connectivity: I^1O^1).
- CPs **17**-**18** transform into new dehydrated phases upon thermal post-treatment which can be a reversible phase transition process (Ba-CP **18**).
- These materials are thermally stable and exhibit small surface areas.

5.5.1. Mechanochemical synthesis

Compounds **17**, **18**, and **19** were synthesized by milling anthranilic acid (*o*ABAH) and Ca-, Sr-, and Ba-hydroxides, correspondingly. The molar ratio between the organic and inorganic precursors was maintained as 2:1, respectively. The variations in the water content of inorganic precursors resulted in the same coordination of the respective metal cation (**Figure A.13**). For Sr-based products, the use of different water content led to products which are slightly different from **18**. However, the PXRD patterns are matched in their strong reflections suggesting that all Sr-based products are similar.

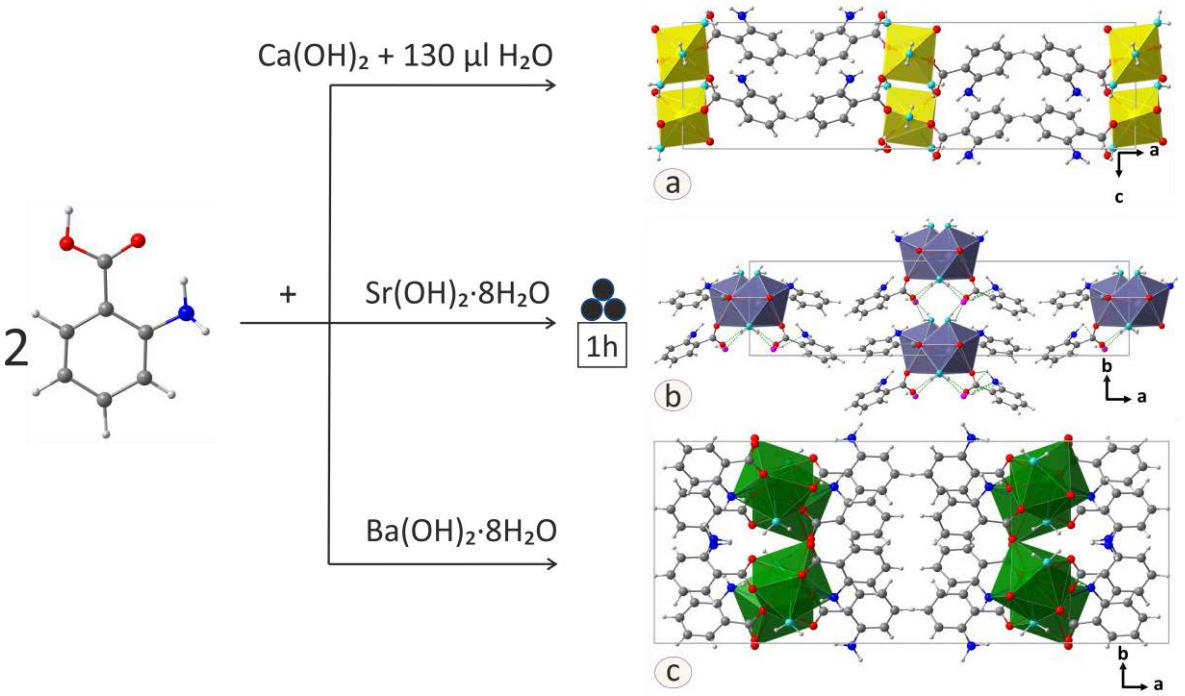

Figure 5.34: The mechanochemical synthesis and crystal structures of CPs **17**, **18**, and **19**. (a) [Ca(*o*ABA)$_2$(H$_2$O)$_3$] (**17**) was obtained by milling *o*ABAH and Ca(OH)$_2$ after adding 130 µL of H$_2$O to the powder mixture. The crystal structure consists of 1D-polymeric chains along c-axis. Every two neighboring polyhedra and organic linkers form the eight-membered ring (Ca$_2$O$_4$C$_2$). (b) [{Sr(*o*ABA)$_2$(H$_2$O)$_2$}·1H$_2$O] (**18**) obtained by milling *o*ABAH and Sr(OH)$_2$·8H$_2$O. In the crystal structure (top view along c-axis), the 1D-polymeric chains are formed in parallel to c-axis. The cocrystallized water molecules connect the 1D-polymeric chains along b-axis via building HBN (green dashed lines). (c) [Ba(*o*ABA)$_2$(H$_2$O)] (**19**) was obtained by milling *o*ABAH and Ba(OH)$_2$·8H$_2$O. The 2D-layered structure is depicted along c-axis. **color code:* calcium (yellow), strontium (blue-grey), barium (green), carboxyl-oxygen (red), coordinating water-oxygen (aqua), cocrystallized water-oxygen (pink), nitrogen (blue), carbon (grey), and hydrogen (light grey).

These findings are consistent with our results regarding the mechanochemical synthesis of the Ca-, Sr-, and Ba-FCPs using tetrafluorobenzene-dicarboxylic acids as organic linkers.[87,88,90,200,206] For the fluorine-free CPs based on benzene-dicarboxylic systems, the variations in water contents influence the crystallinity and the coordination systems of final products.[83,90,200,206]

5.5.2. Crystal Structures

The crystal structures of **17**, **18**, and **19** were successfully refined via the Rietveld method. The results of the refinement are shown in **Figure 5.35**. The crystal data derived from

the refined crystal structures are summarized in **Table 5.5**. The structures after refinements are similar to the reported crystal structures by Murugavel *et al.* via solvothermal treatments.[157]

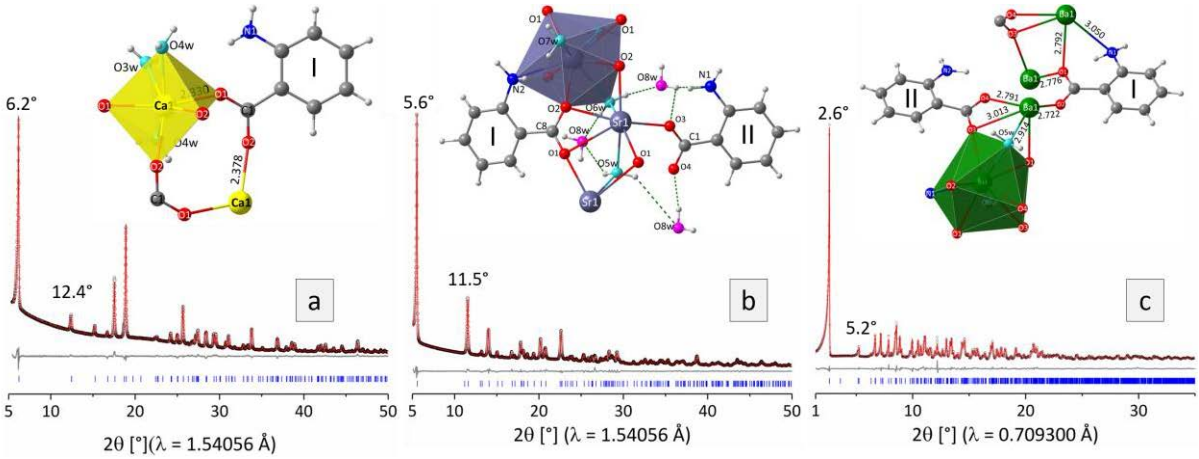

Figure 5.35: The results of Rietveld refinements and the local coordination in the structures of **17** (a), **18** (b), and **19** (c). Only one polyhedron is shown in each structure for clarity. In the refined data, scattered X-ray intensity at ambient conditions is shown as a function of diffraction angle 2θ. The observed pattern (black circles), the best Rietveld fit profile (red line), the reflection positions (blue tick marks), and the difference curve (grey line) between observed and calculated profiles are shown. (a) Ca-atoms in **17** are bridged via the carboxylic group (O1,O2) with I^0O^1 organic connectivity. (b) In Sr-CP **18**, every two SrO_8N polyhedra are connected by three common-faces via two bidentate carboxyl-oxygen atoms (O1 or O2) and one bridging water molecule (O5w or O6w) with inorganic I^1O^0 connectivity. The Cocrystallized water molecules (O8w) connect the 1D-polymeric chains via building HBN (green dashed lines). (c) Coordination environment around Ba-atom in **18** and the inorganic-organic I^1O^1 connectivity whereas the metals are connected via the atoms (O1,O3,O5w) in 1D-inorganic chains that are bridged by the organic linker to form 2D-chains. **color code*: calcium (yellow), strontium (blue-grey), barium (green), carboxyl-oxygen (red), coordinating water-oxygen (aqua), cocrystallized water-oxygen (pink), nitrogen (blue), carbon (grey), and hydrogen (light grey).

[Ca(*o*ABA)$_2$(H$_2$O)$_3$] (**17**): The Ca-based compound crystallizes in the orthorhombic centrosymmetric space group Pbcn. The asymmetric unit consists of one Ca^{2+}-ion and one water molecule that both lie in the two-fold axis, one organic linker, and two more water molecules. The CaO_7 polyhedron comprises four carboxylate-oxygen ligands from four organic linkers, and three terminal aqua-oxygen atoms (**Figure 5.34a**). The organic linkers bridge Ca^{2+}-ions by the two monodentate carboxylate oxygen atoms (O1,O2) and form 1D-polymeric chains (**Figure 5.35a**). The polymeric chains are further connected via HBN that originates

between the water molecules, carboxylate oxygen ligands, and amino groups to form the supramolecular structure of **17**.

[{Sr(*o*ABA)$_2$(H$_2$O)$_2$}·H$_2$O] (**18**): Sr-based CP crystallizes in the monoclinic space group C_2. The asymmetric unit is composed of one Sr^{2+}-ion, two organic linkers, and three water molecules. Different from the hepta-coordination of the smaller Ca^{2+}-ion, Sr^{2+}-ion possess a C.N. of nine and comprises five carboxylate oxygen atoms from four organic ligands, one amino group, one coordinating (O7w), and two bridging water molecules (O5w, O6w). Metal cations are arranged in 1D-polymeric chains via the direct inorganic connections by the carboxylate oxygen atoms (O1, O2), water molecules (O5w, O6w), in addition to the indirect connections via the nitrogen-amino group (N2) (**Figure 5.35b**). Hydrogen bonds are found within the zig-zag chain. The cocrystallized water molecule (O8w) stabilizes the structure by connecting the neighboring 1D polymeric chains via extensive HBN and resulting in the supramolecular structure of **18** (**Figure 5.34b**).

[Ba(*o*ABA)$_2$(H$_2$O)] (**19**): The Ba-based CP crystallizes in the orthorhombic space group Pbcn. The asymmetric unit consists of one Ba^{2+}-ion, two organic linkers, and one water molecule. Different from the hepta-coordinated Ca^{2+}-ions in **17** but like Sr^{2+}-based CP **18**, Ba^{2+}-ion is nine-fold coordinated in **19**. However, the local coordination around metals significantly varies between the two latter complexes. The nine-fold coordination of Ba^{2+}-ion comprises six carboxylate-oxygen atoms, one amino group, and one water molecule (**Figure 5.35c**). Different from the 1D-polymeric chains in **17** and **18**, the polymeric chains in **19** extend to a 2D-network. Ba^{2+}-ions are directly connected via the two carboxylate oxygen atoms (O1,O3) from two organic linkers, the water-oxygen atom (O5w), in addition to the indirect connection by the amino group (N1) to form 1D-polymeric chains. The polymeric chains are bridged via the organic linkers by the binding of the carboxylate oxygen ligand (O2) to the next Ba-ion from the neighboring chain and extend to 2D-polymeric chains. The HBN is limited to the 2D-polymeric chains. Layers of the 2D-polymeric chains form the final crystal structure of **19** (**Figure 5.34c**).

5.5.3 Local Coordination and Influence of Cation Sizes

The variation in the coordination environment, number of crystal water, and reaction mode of *o*ABA^{2-} in the structures of **17** (Ca-CP), **18** (Sr-CP), and **19** (Ba-CP) are determined by the metal cation sizes. The heavier Sr^{2+}- and Ba^{2+}-ions exhibit higher coordination numbers

(CN = 9) compared to the smaller Ca-ions (CN = 7). Here, the large radii allow Sr^{2+}- and Ba^{2+}-ions to possess higher CNs, and to extend the local coordination to the nitrogen-amino groups (**Figure 5.35b-c**). Moreover, the metal-bound water molecules act as bridging ligands (in Sr- and Ba-CPs) rather than capping-ligands (Ca-CP) (**Figure 5.35a**).

The coordination modes of the organic linker in the crystal structures of **17**, **18**, and **19** are depicted in **Figure 5.35**. One type of *o*ABA^{2-} anion is identified in the crystal structure of **17**. Each of the two carboxylate oxygen ligands (O1,O2) acts as a monodentate. Each of two neighboring CaO_7 polyhedra forms an eight-membered ring ($Ca_2O_4C_2$). The nitrogen-amino atom is not directly coordinated to Ca-atom. Nevertheless, the amino group is involved via hydrogen bonding interactions with the carboxylate-oxygen atoms and water molecules. Two types of oABA^{2-} anions that vary in their reaction modes are found in the crystal structure of **18**. *o*ABA^{2-} (I) chelates one Sr-ion via the two carboxylate oxygen atoms (O1,O2) and bridges the chelated metal to another two Sr^{2+}-ions. The bridging mode of the carboxylate group allows the amino group in *o*ABA^{2-} (I) to coordinate with the nearby bridged Sr^{2+}-ion. Sr-N(amino) bond length is 3.069(2) Å. On the other hand, oABA^{2-} (II) acts as a monodentate ligand via one carboxylate-oxygen atom (O3). The metal-bound nitrogen-amino atom and the aromatic carbon atom comprises a longer bond distance of 1.437(2) Å for C-N bond compared to the shorter bond distance of 1.396(1) Å for the C-N bond where the nitrogen-amino atom is free of coordination. In the crystal structure of **19**, two types of oABA^{2-} ligands are also found (**Figure 5.35c**). In the *o*ABA^{2-} (I), one carboxylate oxygen atom (O1) acts as a bidentate and bridges two Ba-ion within the 1D chains and with a coordinating amino group (N1) to the nearby Ba^{2+}-ion. *o*ABA^{2-} (I) ions also bridge the 1D-inorganic chains via the other oxygen atoms (O2) and extend the connection into 2D-polymeric chains (**Figure 5.34c**). *o*ABA^{2-} (II) chelates one Ba^{2+}-ion via the carboxylate group (O3,O4) and bridge another one via O3. The average M^{II}-O(carboxyl) distance become longer as the size of metal cation become larger from Ca^{2+}-, Sr^{2+}-, to Ba^{2+}-ions and from 2.34, 2.61, to 2.79 Å, respectively.

The role of crystal water molecules varies along with the diversity in cation sizes. The smaller Ca-ion (CP **17**) comprises three metal-bound water molecules that are not further involved in the bridging system. Sr^{2+}-ion (CP **18**) is also surrounded by three crystal water molecules. However, the three water molecules in **18** play different roles. One water molecule is Sr-bound in terminus, two bridging water molecules connect the Sr^{2+}-ions within

the 1D-polymeric chains, and a cocrystallized water molecule increases the dimensionality of **18** by bridging the neighboring 1D-polymeric chains via building HBN. In the crystal structure of **19**, the single water molecule bridges Ba-ions within the 1D polymeric chain. The M^{II}-O(water) distances are longer than M^{II}-O(carboxyl) bonds of the same crystal structure. Moreover, the M-O bonds tend to have longer distances as the cation sizes increase. The average M^{II}-O(water) bond lengths are 2.46, 2.66, and 2.86 Å in crystal structures **17**, **18**, and **19**, respectively.

Based on the influence of cation size on the reaction modes of the organic linker and the role of crystal water, the structures of **17**, **18**, and **19** exhibit different inorganic-organic connectivity. Compound **1** exhibits pure organic connectivity of I^0O^1 where the CaO_7 polyhedra are separated by the bridging carboxylate groups (**Figure 5.35a**). Each neighboring SrO_8N or BaO_8N polyhedra within the 1D-polymeric chains in **18** or **19**, separately, exhibit inorganic connectivity via two carboxylate-oxygen anions and one water-oxygen atom (**Figure 5.35b**). In the structure of **19**, the polymeric chains are further bridged via the organic linkers and form 2D-chains (**Figure 5.35c**). For that, the polyhedra connectivity in **18** and **19** are described as I^1O^0 and I^1O^1, correspondingly.

The influence of cation size on the C.N., organic-inorganic connectivity, and dimensionality were also studied elsewhere. For example, in the study by Falcão *et al.*, the CN, M-O-M inorganic connectivity, and dimensionality of resulting Mg-, Ca-, Sr-, and Ba-based CPs increase upon progressing in cation sizes. Concerning the order from Mg, Ca, Sr, to Ba, CNs increase from 6, 7, 8, to 10. Inorganic connectivity increases from 0, 1, 2, to 3 and dimensionality increases from 0, 1, 1, to 2 in the CPs based on Mg, Ca, Sr, and Ba, respectively.[75] Huang *et al.* reported crystal structures that exhibit an increase in dimensionality from 0 (Mg-CP), 2D (Ca- and Sr-CPs), to undulated 2D (Ba-CP).[70]

The local coordination environments around Ca^{2+}- and Sr^{2+}-ions in the refined crystal structures of **17** and **18**, respectively, were investigated by the EXAFS measurements. The simulated data and the measured spectra exhibit a good consistency between the first coordination sphere around the respective metal and the refined structures (**Figure A.14**).

5.5.4. Thermal Properties

The formation of the hydrated compounds of **17**, **18**, and **19** are confirmed by the results of the elemental analysis (**Table A.2**) and thermal analysis (**Figure A.15**). The thermoanalytical

investigation indicates the liberation of three water molecules in the samples of CPs **17** and **18** and one water molecules in compound **19**. The release of the crystal water is complete at 175 °C for **17** (measured: -14.5%, calc. 14.7% for $3H_2O$ molecules), at 150 °C for **18** (measured: -12.8%, calc. 13% for $3H_2O$ molecules), and at 245 °C for **19** (measured: -4.1%, calc. 4.2% for one equivalent H_2O molecule). The water-free frameworks of three compounds are stable up to 280-300 °C. The PXRD patterns of the hydrated and the thermally treated samples at 200 °C of compounds **17**-**19** are compared in **Figure 5.36** and indicate the formation of new phases upon the dehydration processes. The PXRD pattern of the dehydrated sample **19** shows residues of the hydrated phase as indicated by the reflections that match the PXRD pattern of the hydrated sample (not all are visible in the depicted figure). The reflections at 6.1° and 12.3° correspond to the formation of a new phase. The separation between the two phases was difficult due to the high degree of overlap in the diffraction data.

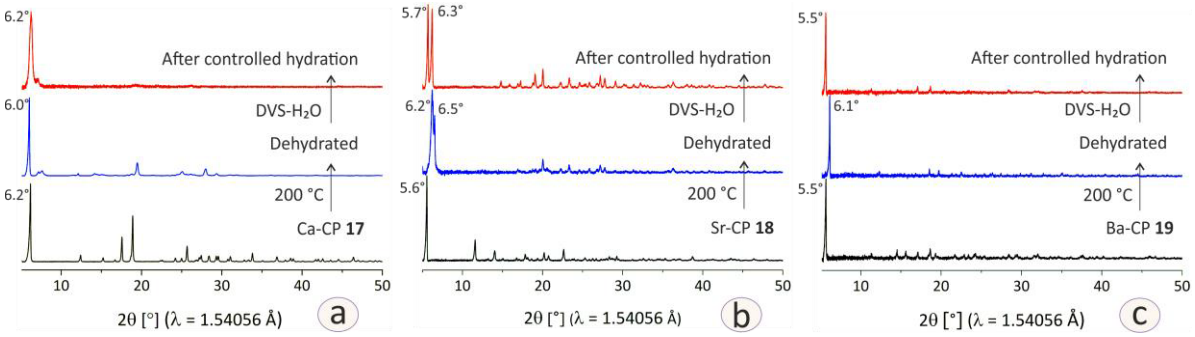

Figure 5.36: PXRD patterns of CPs as-synthesized (black PXRD pattern), dehydrated (200°C) (blue PXRD pattern), and the dehydrated samples after controlled rehydration (red PXRD pattern). (a) Ca-CP **17**, (b) Sr-CP **18**, (c) Ba-CP **19**.

5.5.5. MAS NMR and IR Spectra

The measured MAS NMR spectra are consistent with the determined crystal structures of **17**, **18**, and **19**. (**Figure 5.37a**) shows the typical ^{1}H MAS NMR spectra of compounds **17**, **18**, and **19** with protons located at benzene rings and amino groups, showing superimposed resonances. Milling removes the strong hydrogen bridged network of *o*ABAH, visible with the proton signal of the acid at about 18 ppm. Due to the superposition of the individual signals, the overall ^{1}H MAS NMR spectra are broad and hard to resolve.

The $^{1}H \rightarrow ^{13}C$ CP MAS NMR spectrum of **17** depicts one signal corresponding to one type of carboxylate carbon atom at δ = 173 ppm which is consistent with the refined crystal structure. The depicted signals at δ = 149 and 122 ppm are assigned to the aromatic carbon atoms bound to carboxyl and amino groups, correspondingly. The other four carbon (C-H) types known from the crystal structure are allocated at δ = 134, 132, 117, and 116 ppm. The variation in the intensity of signals is due to that some of the aromatic C-H bonds are involved in the intra- and intermolecular hydrogen bonds between carboxylate-oxygen, water-oxygen, and nitrogen atoms. The narrow and well-defined signals are an indication for the good crystallinity of the Ca-containing sample. In the $^{1}H \rightarrow ^{13}C$ CP MAS NMR spectrum of **18**, the two carboxylate carbon atoms from the two types of organic linkers are depicted at 176 and 174 ppm. The two contributions at 123 and 121 ppm are assigned to the two carbon atoms bound to nitrogen-amino atoms (C-NH_2). The signal at δ = 149 ppm corresponds to the aromatic carbon atoms connected to carboxyl groups and are free of protons (C(ring)-COO).

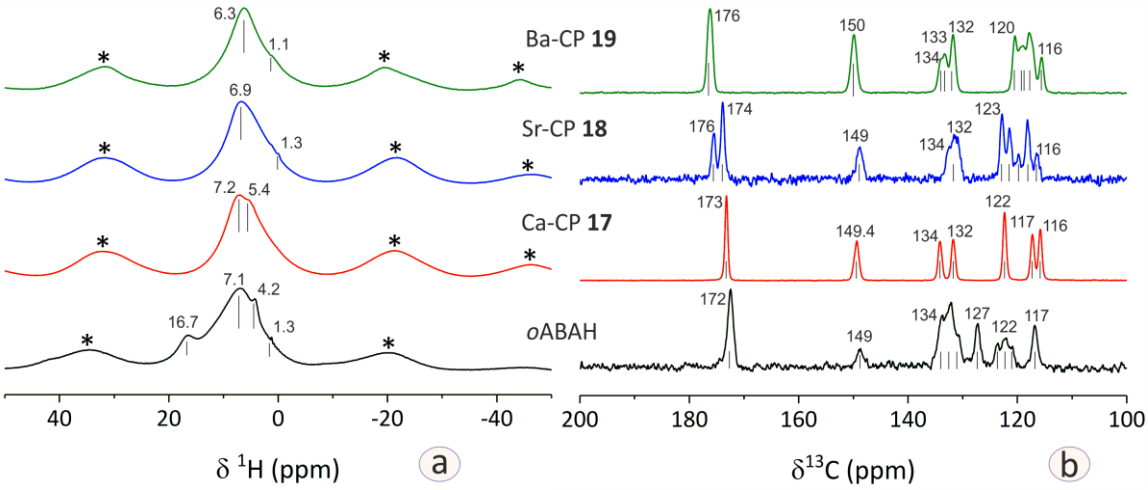

Figure 5.37: ^{1}H MAS NMR Spectra (a) and $^{1}H \rightarrow ^{13}C$ CP MAS NMR spectra (b) of the organic ligand *o*ABAH (black spectra), [Ca(*o*ABA)$_2$(H_2O)$_3$] (**17**) (red spectra), [{Sr(*o*ABA)2(H_2O)$_2$}·H_2O] (**18**) (blue spectra), and [Ba(oABA)$_2$(H_2O)] (**19**) (green spectra).

The signals corresponding to the aromatic carbon atoms C-H are depicted at δ = 132, 120, 118, 116 ppm. The other C-H signals known from the crystal structure are covered within the broad signal at 134 ppm. The intensities of signals are reduced by applying longer contact time of 10 ms (red spectrum) which is typical for the magnetization transfer over a longer distance.

The $^{1}H \rightarrow ^{13}C$ CP MAS NMR spectrum of **19** depicts one signal corresponds to carboxylate carbon atoms. The two carboxylate carbon atoms from the two types of organic linkers are not identified by applying shorter longer contact time due to that both carbon types are quite similar in their reaction modes (Each carboxyl group bound to three barium atoms using one monodentate and one bidentate-oxygen). The proton-free carbon atoms bound to carboxyl group is assigned at 150 ppm. The two carbon types of C-NH_2 known from crystal structures are covered by a broad signal at δ = 119 ppm when a shorter contact time is applied (1 ms, black spectrum). By applying a longer contact time (10 ms), the two types are resolved at δ = 120 and 119 ppm. The C-H positions in the aromatic rings are assigned at δ = 133 (broad signal with a shoulder at δ = 134 ppm), 132, 118, and 116 ppm.

The vibrational bands belong to the stretching vibration of the amine groups (**Figure 5.38**, black spectrum) are masked by the strong vibrational bands above 3000 cm^{-1} in the red, blue, and green spectra. The latter vibrational bands are attributed to the presence of different types of water molecules, and the formation of HBNs along the crystal structures of compounds **17**-**19**.[148]

Several contributions are assigned to the presence of water within the crystal structures of **17**-**19**. The bands assigned to water bending appear at 1643 cm^{-1} (red spectrum), 1662 cm^{-1} (blue spectrum), and 1700 cm^{-1} (green spectrum).

The broad contribution around 300 – 3400 cm^{-1} are assigned to the presence of hydrogen-bonds. The OH stretching of water is assigned at 3418 cm^{-1} (CPs **17** and **18**) and 3440 cm^{-1} (CP **19**). The OH-stretching at υ = 3693 and 3612 cm^{-1} indicate the presence of cocrystallized water in **18**. The bands assigned to the carboxylate stretching appear at 1530 cm^{-1} for asymmetric stretching (υ_{as}) and 1393 cm^{-1} for symmetric stretching (υ_{s}) in CPs **17** and **18**. In CP **19**, the carboxylate stretching appears at 1512 cm^{-1}(υ_{as}) and

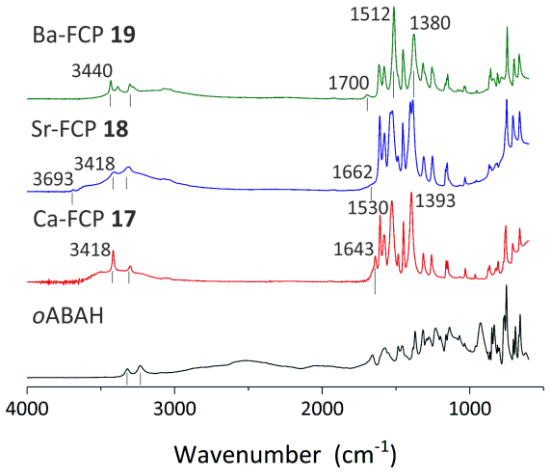

Figure 5.38: The ATR-IR spectra of anthranilic acid (black spectrum), Ca-CP **17** (red spectrum), Sr-CP **18** (blue spectrum), and Ba-CP **19** (green spectrum).

1380 cm^{-1}(υ_s). The separation (Δ_{a-s}) between asymmetric and symmetric stretching of carboxylate groups are about 137 cm^{-1} (CPs **17** and **18**) and 132 cm^{-1} (CP **19**) which are attributed to the multi-dentate mode of carboxylate groups in the crystal structures.[73,203]

5.5.6. Sorption Properties and Morphology

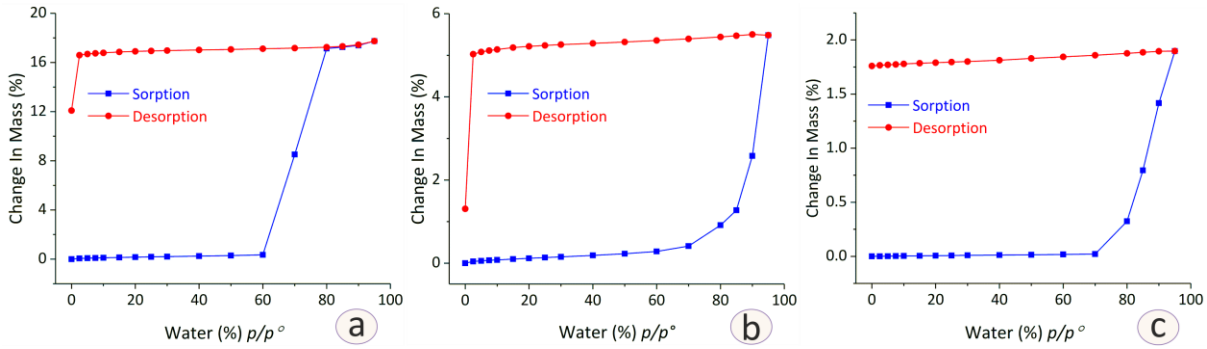

Figure 5.39: (a) Isotherm curves for the dynamic vapor sorption of water on thermally treated samples (200°C) of compounds **17** (a), **18** (b), and **19** (c). The adsorption curves (blue) and desorption (red).

The hydrated samples of **17**, **18**, and **19** exhibit very small surface areas of 7.2, 2.9, and 3.2 m^2/g, respectively. The surface areas become even smaller for the dehydrated samples. The controlled hydration of the dehydrated samples **17**, **18**, and **19** indicates chemical sorption for all samples (**Figure 5.39**) and the formation of new hydrated phase (**Figure 5.36**). For Ba-CP **19**, the dehydrated-hydrated phase transition is reversible as indicated by the PXRD patterns (**Figure 5.36c**). The SEM images (**Figure 5.40**) depict similar morphologies for the three compounds that can be described as plate-like structures.

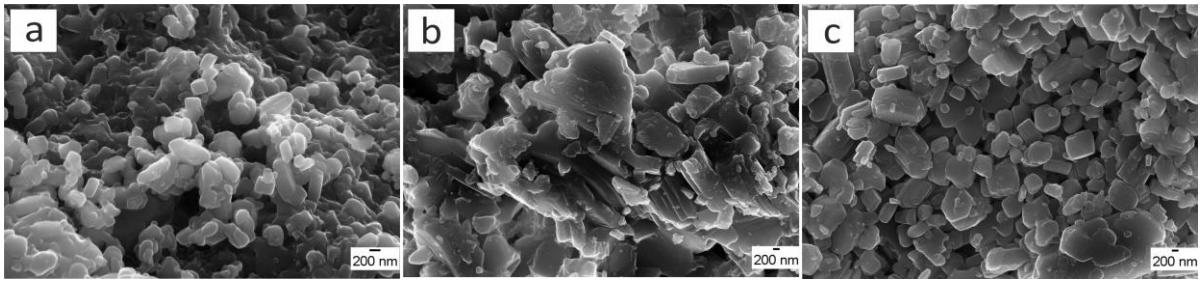

Figure 5.40: SEM images of (a) [Ca(*o*ABA)$_2$(H$_2$O)$_3$] (**17**), (b) [{Sr(*o*ABA)$_2$(H$_2$O)$_2$}·1H$_2$O] (**18**), and (c) [Ba(*o*ABA)$_2$(H$_2$O)] (**19**).

5.5.7. Comparison and Conclusion

In summary, the mechanochemical synthesis and structural diversity of CPs based on alkaline earth metals and anthranilic acid are described. Compounds **17**, **18**, and **19** were synthesized by milling Ca-, Sr-, or Ba-hydroxides and anthranilic acid, respectively. The best results are achieved by adding a small amount of water to Ca(OH)$_2$ to compensate for the absence of water required for building the trihydrate CP **17**. The octahydrate metal hydroxides Sr(OH)$_2$·8H$_2$O and Ba(OH)$_2$·8H$_2$O were used as inorganic precursors for synthesizing Sr-, and Ba-based CPs, respectively. Here, the best results were achieved using internal water source (crystal water from the crystal structure of octahydrate metal hydroxides) rather adding a small amount of water to Sr(OH)$_2$ Ba(OH)$_2$ samples. C.N., connectivity of polyhedra, and the dimensionality of crystal structures are determined by cation sizes. As the cation size becomes larger as C.N. increases from seven (in Ca-CP) to nine (Sr- and Ba-CP) and with connections of I^0O^1, I^1O^0, to I^1O^1, respectively. Crystal water in CPs based on the heavier metals (Sr and Ba) is involved in the bridging systems rather than only capping ligands (Ca-CP). These compounds are thermally stable and exhibit small surface areas. Compounds **17**-**19** transform into new dehydrated phases upon thermal post-treatment which can be a reversible phase transition process (Ba-CP).

Table 5.5: Coordination environments, crystal data, and refined parameters derived from the crystal structures of compounds **17**, **18**, **and 19**.

	$[Ca(oABA)_2(H_2O)_3]$ (**17**)	$[\{Sr(oABA)_2(H_2O)_2\}\cdot 1H_2O]$ (**18**)	$[Ba(oABA)_2(H_2O)]$ (**19**)
C.N.	7	9	9
M-O (carboxyl)	4 (O1, O1', O2, O2') from 4 ligands	5 (O1, O1', O2, O2', O3) from 4 ligands	6 (O1, O1', O2, O2', O3, O4) from 5 ligands
M-N (amino)	-	1 (N2)	1 (N1)
Coordinating H_2O molecules	3 (O3w, O4w, O4w')	1 terminal (O7w) + 2 bridging (O5w, O6w)	2 bridging (O5w, O5w')
Crystal water	-	1 (O6w)	-
Coordination mode (Ligand)	2Ca (bidentate carboxyl group)	Lignad1: 3Sr (O1, O2, N2) Ligand 2: 1Sr (O3)	Lignad1: 3Ba (O1, O2, N1) Ligand 2: 2Ba (O3,O4)
C—O (carboxylate) (Å)	1.260(4) - 1.261(5)	1.236(1) - 1.264(1)	1.264(1) - 1.281(1)
C—N (amino) (Å)	1.399	1.396(1) - 1.437(2)	1.375(1) - 1.411(1)
M^{II}—O (carboxylate) (Å)	2.331(5) - 2.378(5)	2.491(1) - 2.929(1)	2.721(1) - 3.013(1)
M^{II}—N (amino) (Å)	-	3.069(2)	3.051(1)
M^{II}—O (water) (Å)	2.413(1) -2.489(5)	2.625(2) - 2.711(2)	2.890(1) - 2.914(1)
O—M^{II}—O angle (°)	73.680(9) - 163.863(2)	46.289(4) – 148.222(3)	44.754(1) – 148.664(1)
M^{II}—(chain)—M^{II} (Å)	1D: Ca-(Ligand)-Ca = 4.706(1)	1D Sr-(O5w,O1,O1')-Sr = 3.913(4) 1D Sr-(O6w,O2,O2')-Sr = 3.917(4)	1D: Ba-(O5w,O1,O3)-Ba = 4.329(1) 2D: Ba-(Ligand)-Ba = 6.084(1)
M^{II}—M^{II}—M^{II} angle (°) (1D-chain)	114.721(1)	122.945(9)	129.222(1)
$M^{II}\cdots$(interlayer)$\cdots M^{II}$ (Å)	14.2	7.832(9)	14.369(4)
Dimensionality	1D (I^0O^1)	1D (I^1O^0)	2D (I^1O^1)
Cell parameters			
Empirical formula	$C_{14}H_{18}CaN_2O_7$	$C_{14}H_{18}SrN_2O_7$	$C_{14}H_{14}BaN_2O_5$
Cell mass (g/mol)	366.38	413.92	427.6
Crystal system	Orthorhombic	Monoclinic	Orthorhombic
Space group	Pbcn (60)	C_2 (5)	Pbcn (60)
Cell volume ($Å^3$)	1652.17(5)	1701.62(7)	2952.23(2)
a (Å)	28.433(6)	32.085(9),	31.021(1)
b (Å)	7.332(1)	7.832(1),	12.167(4

	[Ca(oABA)$_2$(H$_2$O)$_3$] (**17**)	[{Sr(oABA)$_2$(H$_2$O)$_2$}·1H$_2$O] (**18**)	[Ba(oABA)$_2$(H$_2$O)] (**19**)
c (Å)	7.926(1)	6.879(2)	7.822(2)
α, β, γ (°)	α = β = γ = 90	α = γ = 90, β = 100.157	α = β = γ = 90
Cell ratio			
a/b	3.878	4.09	2.551
b/c	0.925	1.1386	1.555
c/a	0.279	0.2144	0.252
Z	4	4	8
Density (calc.) g/cm^3	1.47	1.62	1.92
Refinement parameters			
R_{wp}	2.69	3.19	4.65
R_p	1.82	2.15	3.28
R_{Bragg}	2.213	1.166	1.863
GOF	2.31	4.30	2.95
PXRD measurements			
Instrument/ BeamLine	D8 Discover		STOE Stadi MP
Calibration	Si standard powder		
λ (Å)	1.54056 (Cu-$K_{\alpha1}$)		0.709300 (Mo-$K_{\alpha1}$)
2θ range (°)	5 – 65		1 – 50
step size	0.009°		0.015°
Collection time	35 h		17 h

6. Conclusion

In this work, a series of fluorine-containing coordination polymers (FCPs) were synthesized by milling Ca-, Sr-, and Ba-hydroxides and tetrafluorobenzene-dicarboxylic acids ($H_2BDC\text{-}F_4$). The obtained FCPs are compared to their synthesized fluorine-free counterparts (CPs) under the same conditions and using benzene-dicarboxylic acids (H_2BDC) as organic linkers (**Table 6.1**). Here, the replacement of hydrogens of an aromatic ring by fluorine atoms plays a vital role in the variation of structural properties and thermal stabilities of the resulting FCPs. Moreover, the difference in geometries within the perfluorinated and fluorine-free organic isomers influences the coordination environments of both FCPs and CPs.

Water plays a dual role at milling. During the milling process, water helps to achieve the required crystallinities of final products (so-called a liquid-assisted grinding). A certain crystallinity is required because the products are polycrystalline powders and their crystal structures are solved from powder diffraction data. Water also stabilizes the crystal structures of the FCPs as well as CPs and acts as a metal-bound ligand in capping or bridging modes. Water might also be present as a free ligand in the crystal structures and form hydrogen bridges.

The variation in the water content of the inorganic precursors does not influence the number of coordinating water molecules in the final FCPs. However, the water content of the reactants affects at least the crystallinity of the newly formed FCPs, which increases by adding a small fraction of water to $Ca(OH)_2$ or by using strontium and barium hydroxide octahydrates as inorganic sources. The latter outcome contrasts with the mechanochemical synthesis of the fluorine-free CPs wherein the water content of inorganic samples mainly influence the number of coordinating water molecules of the final products. Along with these findings, the water content of the reactants has a strong influence on the necessary milling time. The lower the water content, the longer is the required milling time.

The hydrated compounds exhibit small surface areas that could increase after thermal-post treatment. The thermal stabilities of the FCPs are comparable and begin to decompose around 300 °C. The fluorine-free CPs are stable up to 400 °C.

Table 6.1: The compounds obtained by milling Ca-, Sr-, and Ba-hydroxides with a respective organic linker. *The discussed compounds in this work are described with identification numbers. **M^{II} = (Ca and Sr) in the isomorphic structures. Otherwise, the metal cation is named.

	para- systems	*meta*- systems	*ortho*-systems
$H_2BDC\text{-}F_4$	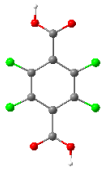 $H_2pBDC\text{-}F_4$	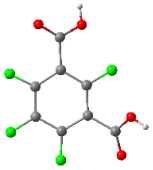 $H_2mBDC\text{-}F_4$	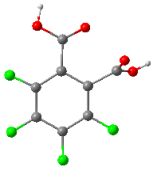 $H_2oBDC\text{-}F_4$
Ca-FCPs	$[M^{II}(pBDC\text{-}F_4)(H_2O)_4]$ (**1,2**) **(2D, I^1O^1)**	$[M^{II}(mBDC\text{-}F_4)(H_2O)_3]$ (**3,4**) **(3D, I^1O^2)**	$[M^{II}(oBDC\text{-}F_4)(H_2O)_2]$ (**5,6**) **(2D, I^2O^0)**
Sr-FCPs			
Ba-FCPs	$[Ba(pBDC\text{-}F_4)(H_2O)_{0.5}]$ (**12**) **(3D, I^2O^1)**	$[Ba(mBDC\text{-}F_4)(H_2O)_{0.5}]$ (**13**)	$[Ba(oBDC\text{-}F_4)(H_2O)_{1.5}]$ (**14**)
H_2BDC	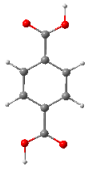 H_2pBDC	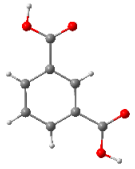 H_2mBDC	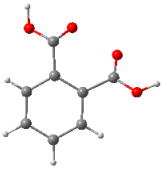 H_2oBDC
Ca-CPs	$[M^{II}(pBDC)(H_2O)_3]$ (**7**) **(1D, I^1O^0)**	$[M^{II}(mBDC)(H_2O)_{3.4}]$ (**8,9**) **(1D, I^1O^0)**	$[Ca(oBDC)(H_2O)_1]$ (**10**) **(2D, I^2O^0)**
Sr-CPs			$[Sr(oBDC)(H_2O)_3]$ (**11**) **(2D, I^2O^0)**
Ba-CPs	$[Ba(pBDC)(H_2O)_{1.5}]$	$[Ba(mBDC)(H_2O)_{0.5}]$ (**15**)	$[Ba(mBDC)(H_2O)_{0.5}]$ (**16**)
$ABAH\text{-}F_4$	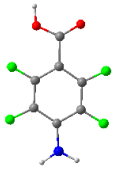 $pABAH\text{-}F_4$	-	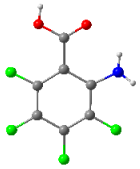 $oABAH\text{-}F_4$
Ca-FCPs	$[Ca(pABA\text{-}F_4)_2(H_2O)_n]$	-	$[Ca(oABA\text{-}F_4)_2(H_2O)_2]$ **(1D, I^0O^1)**
Sr-FCPs	$[Sr(pABA\text{-}F_4)_2(H_2O)_2]$	-	$[Sr(oABA\text{-}F_4)_2(H_2O)_2]$
Ba-FCPs	$[Ba(pABA\text{-}F_4)_2(H_2O)_2]$	-	$[Ba(oABA\text{-}F_4)_2(H_2O)_2]$
ABAH	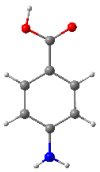 *p*ABAH	 *m*ABAH	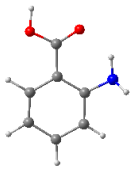 *o*ABAH
Mg-CP			$[Mg(oABA)_2]$
Ca-CPs	$[Ca(pABA)_2(H_2O)_2]$	$[Ca(mABA)_2(H_2O)_2]$ **(1D, I^1O^0)**	$[Ca(oABA)_2(H_2O)_3]$ (**17**) **(1D, I^0O^1)**
Sr-CPs	$[Sr(pABA)_2(H_2O)_2]$ **(1D, I^1O^0)**	$[Sr(mABA)_2(H_2O)_3]$ **(1D, I^1O^0)**	$[Sr(oABA)_2(H_2O)_3]$ (**18**) **(1D, I^1O^0)**
Ba-CPs	$[Ba(pABA)_2(H_2O)_{2.45}]$ **(1D, I^1O^0)**	$[Ba(mABA)_2(H_2O)_4]$ **(1D, I^1O^0)**	$[Ba(oABA)_2(H_2O)]$ (**18**) **(2D, I^1O^1)**

Conclusion

Ca- and Sr-based FCPs and CPs crystallize isomorphously in their coordination to a respective perfluorinated or nonfluorinated benzene-dicarboxylate system (**Table 6.1**). An exception is recorded for Ca- and Sr-phthalates.

Topologies and geometries of the perfluorinated organic precursors ($H_2BDC\text{-}F_4$), as well as the nonfluorinated ligands (H_2BDC), influence the coordination environment and the dimensionality of the obtained compounds (**Figure 5.3**, **Figure 5.13**, and **Figure 5.24**).

In the Ca- and Sr-FCPs based on *para*- and *meta*-isomers, the organic linkers bridge the inorganic chains and propagate the coordination systems to 2D and 3D-structures, respectively (**Figure 5.1a-b**). In contrast, terephthalate- and isophthalate-based CPs are formed of 1D-inorganic chains (**Figure 5.9** and **Figure 5.10**). Both fluorinated and fluorine-free CPs based on *ortho*-Linkers are 2D-structures (**Figure 5.1c, Figure 5.11,** and **Figure 5.12**).

The higher dimensionality of FCPs is mainly caused by the twisting of carboxylate groups out the planar plane of the benzene ring which is attributable to the electrostatic repulsion between the highly electronegative fluorine atoms and the lone-pair electrons of carboxylate-oxygen atoms.

In the anthranilate-based CPs, the variation in the cation size between Ca^{2+}-, Sr^{2+}-, and Ba^{2+}-ions influences both local coordination and dimensionality of structures (**Figure 5.34**). The coordination number increases from seven (in Ca-CP) to nine (in Sr- and Ba-CPs) and with inorganic-organic connections of I^0O^1, I^1O^0, to I^1O^1, respectively. Water ligands play roles for bridging the metal chains in Sr- and Ba-based CPs rather than only the capping ligand in Ca-CP.

The work on the other nitrogen-containing FCPs and CPs is in progress (**Table 6.1**).

References

(1) Cheetham, A. K.; Rao, C. N. R.; Feller, R. K. Structural diversity and chemical trends in hybrid inorganic–organic framework materials. *Chem. Commun.* **2006**, *0* (46), 4780-4795.

(2) Boldyreva, E. Mechanochemistry of inorganic and organic systems: what is similar, what is different? *Chem. Soc. Rev.* **2013**, *42* (18), 7719-7738.

(3) Do, J. L.; Friščić, T. Mechanochemistry: A Force of Synthesis. *ACS Cent. Sci.* **2017**, *3* (1), 13–19.

(4) Boldyrev, V. V.; Tkáčová, K. Mechanochemistry of solids: Past, present, and prospects. *J. Mater. Synth. Process.* **2000**, *8* (3/4), 121–132.

(5) Duwez, A. S.; Cuenot, S.; Jérôme, C.; Gabriel, S.; Jerome, R.; Rapino, S.; Zerbetto, F. Mechanochemistry: Targeted delivery of single molecules. *Nat. Nanotechnol.* **2006**, *1* (2), 122–125.

(6) Wang, G. -W.. Mechanochemical Organic Synthesis. *Chem. Soc. Rev.* **2013**, *42*, 7668-7700.

(7) Grätz, S.; Borchardt, L. Mechanochemical polymerization – controlling a polycondensation reaction between a diamine and a dialdehyde in a ball mill. *RSC Adv.* **2016**, *6* (69), 64799–64802.

(8) Julien, P. A.; Mottillo, C.; Friščić, T. Metal–organic frameworks meet scalable and sustainable synthesis. *Green Chem.* **2017**, *19* (12), 2729–2747.

(9) Zhan, G.; Zeng, H. C. Alternative synthetic approaches for metal–organic frameworks: transformation from solid matters. *Chem. Commun.* **2017**, *53* (1), 72–81.

(10) Baláž, P.; Achimovičová, M.; Baláž, M.; Billik, P.; Cherkezova-Zheleva, Z.; Criado, J. M.; Delogu, F.; Dutková, E.; Gaffet, E.; Gotor, F. J.; et al. Hallmarks of mechanochemistry: from nanoparticles to technology. *Chem. Soc. Rev.* **2013**, *42* (18), 7571.

(11) Hernández, J. G.; Friščić, T. Metal-catalyzed organic reactions using mechanochemistry. *Tetrahedron Lett.* **2015**, *56* (29), 4253–4265.

(12) Stolle, A.; Szuppa, T.; Leonhardt, S. E. S.; Ondruschka, B. Ball milling in organic synthesis: solutions and challenges. *Chem. Soc. Rev.* **2011**, *40* (5), 2317.

(13) Suslick, K. S. Mechanochemistry and sonochemistry: concluding remarks. *Faraday Discuss.* **2014**, *170*, 411–422.

(14) Beyer, M. K.; Clausen-Schaumann, H. Mechanochemistry: The mechanical activation of covalent bonds. *Chem. Rev.* **2005**, *105* (8), 2921–2948.

(15) Tanaka, K. Solvent-Free Organic Synthesis. *Solvent-Free Org. Synth.* **2009**, *100* (3), 1-457.

(16) Matoga, D.; Oszajca, M.; Molenda, M. Ground to conduct: mechanochemical synthesis of a metal–organic framework with high proton conductivity. *Chem. Commun.* **2015**, *51* (36), 7637–7640.

(17) Braga, D.; Grepioni, F.; André, V.; Duarte, M. T. Drug-containing coordination and hydrogen bonding networks obtained mechanochemically. *CrystEngComm* **2009**, *11* (12), 2618.

(18) Braga, D.; Curzi, M.; Johansson, A.; Polito, M.; Rubini, K.; Grepioni, F. Simple and quantitative mechanochemical preparation of a porous crystalline material based on a 1D coordination network for uptake of small molecules. *Angew. Chem. Int. Ed.* **2005**, *45* (1), 142–146.

(19) Xu, C.; De, S.; Balu, A. M.; Ojeda, M.; Luque, R. Mechanochemical synthesis of advanced nanomaterials for catalytic applications. *Chem. Commun.* **2015**, *51* (31), 6698–6713.

(20) Ma, X.; Lim, G. K.; Harris, K. D. M.; Apperley, D. C.; Horton, P. N.; Hursthouse, M. B.; James, S. L. Efficient, Scalable, and Solvent-free Mechanochemical Synthesis of the OLED Material Alq 3 (q = 8‑Hydroxyquinolinate). *Cryst. Growth Des.* **2012**, *12*, 5869-5872.

(21) Bowmaker, G. A. Solvent-assisted mechanochemistry. *Chem. Commun.* **2013**, *49* (4), 334–348.

(22) Friščić, T. New opportunities for materials synthesis using mechanochemistry. *J. Mater. Chem.* **2010**, *20* (36), 7599.

(23) Trask, A. V.; Motherwell, W. D. S.; Jones, W. Solvent-drop grinding: green polymorph control of cocrystallisation. *Chem. Commun.* **2004**, No. 7, 890.

(24) Trask, A. V.; Jones, W. Crystal engineering of organic cocrystals by the solid-state grinding approach. *Top. Curr. Chem.* **2005**, *254*, 41–70.

(25) Friščić, T.; Trask, A. V.; Jones, W.; Motherwell, W. D. S. Screening for inclusion compounds and systematic construction of three-component solids by liquid-assisted grinding. *Angew. Chem. Int. Ed.* **2006**, *45* (45), 7546–7550.

(26) Lien Nguyen, K.; Friščić, T.; Day, G. M.; Gladden, L. F.; Jones, W. Terahertz time-domain spectroscopy and the quantitative monitoring of mechanochemical cocrystal formation. *Nat. Mater.* **2007**, *6* (3), 206–209.

(27) Friščič, T.; Jones, W. Recent advances in understanding the mechanism of cocrystal formation via grinding. *Cryst. Growth Des.* **2009**, *9* (3), 1621–1637.

(28) Kaupp, G. Mechanochemistry: the varied applications of mechanical bond-breaking. *CrystEngComm* **2009**, *11* (3), 388–403.

(29) Hasa, D.; Schneider, G.; Voinovich, D.; Jones, W. Cocrystal Formation through Mechanochemistry: From Neat and Liquid-Assisted Grinding to Polymer-Assisted Grinding. *Angew. Chem. Int. Ed.* **2015**, *54* (25), 7371–7375.

(30) Stock, N.; Biswas, S. Synthesis of metal-organic frameworks (MOFs): Routes to various MOF topologies, morphologies, and composites. *Chem. Rev.* **2012**, *112* (2), 933–969.

(31) Robin, A. Y.; Fromm, K. M. Coordination polymer networks with O- and N-donors: What they are, why and how they are made. *Coord. Chem. Rev.* **2006**, *250* (15–16), 2127–2157.

(32) Batten, S. R.; Champness, N. R.; Chen, X.-M.; Garcia-Martinez, J.; Kitagawa, S.; Öhrström, L.; O'Keeffe, M.; Paik Suh, M.; Reedijk, J. Terminology of metal–organic frameworks and coordination polymers (IUPAC Recommendations 2013). *Pure Appl. Chem.* **2013**, *85* (8), 1715–1724.

(33) Moulton, B.; Zaworotko, M. J. From molecules to crystal engineering: Supramolecular isomerism and polymorphism in network solids. *Chem. Rev.* **2001**, *101* (6), 1629–1658.

(34) Cook, T. R.; Zheng, Y. R.; Stang, P. J. Metal-organic frameworks and self-assembled supramolecular coordination complexes: Comparing and contrasting the design, synthesis, and functionality of metal-organic materials. *Chem. Rev.* **2013**, *113* (1), 734-777.

(35) Tanabe, K. K.; Cohen, S. M. Postsynthetic modification of metal–organic frameworks—a progress report. *Chem. Soc. Rev.* **2011**, *40* (2), 498–519.

(36) Haldar, R.; Maji, T. K. Metal–organic frameworks (MOFs) based on mixed linker systems: structural diversities towards functional materials. *CrystEngComm* **2013**, *15* (45), 9276.

(37) Deria, P.; Mondloch, J. E.; Karagiaridi, O.; Bury, W.; Hupp, J. T.; Farha, O. K.

Beyond post-synthesis modification: evolution of metal–organic frameworks via building block replacement. *Chem. Soc. Rev.* **2014**, *43* (16), 5896–5912.

(38) Janiak, C. Engineering coordination polymers towards applications. *Dalton Trans.* **2003**, No. 14, 2781.

(39) Kitagawa, S.; Kitaura, R.; Noro, S. I. Functional porous coordination polymers. *Angew. Chem. Int. Ed.* **2004**, *43* (18), 2334–2375.

(40) He, Y.; Li, B.; O'Keeffe, M.; Chen, B. Multifunctional metal–organic frameworks constructed from meta-benzenedicarboxylate units. *Chem. Soc. Rev.* **2014**, *43* (16), 5618–5656.

(41) Canivet, J.; Fateeva, A.; Guo, Y.; Coasne, B.; Farrusseng, D. Water adsorption in MOFs: fundamentals and applications. *Chem. Soc. Rev.* **2014**, *43* (16), 5594–5617.

(42) Silva, P.; Vilela, S. M. F.; Tomé, J. P. C.; Almeida Paz, F. A. Multifunctional metal–organic frameworks: from academia to industrial applications. *Chem. Soc. Rev.* **2015**, *44* (19), 6774–6803.

(43) Li, B.; Chrzanowski, M.; Zhang, Y.; Ma, S. Applications of metal-organic frameworks featuring multi-functional sites. *Coord. Chem. Rev.* **2016**, *307*, 106–129.

(44) Furukawa, H.; Cordova, K. E.; O'Keeffe, M.; Yaghi, O. M. The chemistry and applications of metal-organic frameworks. *Science* **2013**, *341* (6149), 1230444.

(45) *The Chemistry of Metal-Organic Frameworks: Synthesis, Characterization, and Applications*, 2nd ed.; Kaskel, S., Ed.; WILEY-VCH: Weinheim, 2016.

(46) Du, S.; Zhang, H. *Metal-Organic Frameworks for Photonics Applications*; Chen, B., Qian, G., Eds.; Structure and Bonding; Springer Berlin Heidelberg: Berlin Heidelberg, 2014; Vol. 157.

(47) Yaghi, O. M.; O'Keeffe, M.; Ockwig, N. W.; Chae, H. K.; Eddaoudi, M.; Kim, J. Reticular synthesis and the design of new materials. *Nature* **2003**, *423* (6941), 705–714.

(48) Hulvey, Z.; Ayala, E.; Furman, J. D.; Forster, P. M.; Cheetham, A. K. Structural diversity in coordination polymers composed of divalent transition metals, 2,2'-bipyridine, and perfluorinated dicarboxylates. *Cryst. Growth Des.* **2009**, *9* (11), 4759–4765.

(49) Kasai, K.; Aoyagi, M.; Fujita, M. Flexible coordination networks with fluorinated backbones. Remarkable ability for induced-fit enclathration of organic molecules. *J. Am. Chem. Soc.* **2000**, *122* (9), 2140–2141.

(50) Pachfule, P.; Chen, Y.; Jiang, J.; Banerjee, R. Fluorinated metal-organic frameworks: Advantageous for higher H 2 and CO 2 adsorption or not? *Chem. - A Eur. J.* **2012**, *18* (2), 688–694.

(51) Almeida Paz, F. A.; Klinowski, J.; Vilela, S. M. F.; Tomé, J. P. C.; Cavaleiro, J. A. S.; Rocha, J. Ligand design for functional metal–organic frameworks. *Chem. Soc. Rev.* **2012**, *41* (3), 1088–1110.

(52) Uneyama, K. *Organofluorine Chemistry*; Blackwell Publishing Ltd.: Oxford, 2007.

(53) Peikert, K.; Hoffmann, F.; Fröba, M. Fluorine magic: one new organofluorine linker leads to three new metal–organic frameworks. *CrystEngComm* **2015**, *17* (2), 353–360.

(54) Tan, K.; Nijem, N.; Gao, Y.; Zuluaga, S.; Li, J.; Thonhauser, T.; Chabal, Y. J. Water interactions in metal organic frameworks. *CrystEngComm* **2015**, *17* (2), 247–260.

(55) Serre, C. Superhydrophobicity in highly fluorinated porous metal-organic frameworks. *Angew. Chem. Int. Ed.* **2012**, *51* (25), 6048–6050.

(56) Howarth, A. J.; Liu, Y.; Li, P.; Li, Z.; Wang, T. C.; Hupp, J. T.; Farha, O. K. Chemical, thermal and mechanical stabilities of metal-organic frameworks. *Nat. Rev. Mater.* **2016**, *1* (3), 15018.

(57) Rao, C. N. R.; Natarajan, S.; Vaidhyanathan, R. Metal carboxylates with open architectures. *Angew. Chem. Int. Ed.* **2004**, *43* (12), 1466–1496.

(58) Fromm, K. M. Coordination polymer networks with s-block metal ions. *Coord. Chem. Rev.* **2008**, *252* (8–9), 856–885.

(59) Banerjee, D.; Parise, J. B. Recent advances in s-block metal carboxylate networks. *Cryst. Growth Des.* **2011**, *11* (10), 4704–4720.

(60) Arlin, J. B.; Florence, A. J.; Johnston, A.; Kennedy, A. R.; Miller, G. J.; Patterson, K. Systematic data set for structure-property investigations: Solubility and solid-state structure of alkaline earth metal salts of benzoates. *Cryst. Growth Des.* **2011**, *11* (4), 1318–1327.

(61) Wang, J. H.; Tang, G. M.; Qin, T. X.; Yan, S. C.; Wang, Y. T.; Cui, Y. Z.; Weng Ng, S. A set of alkali and alkaline-earth coordination polymers based on the ligand 2-(1H-benzotriazol-1-yl) acetic acid: Effects the radius of metal ions on structures and properties. *J. Solid State Chem.* **2014**, *219*, 55–66.

(62) Wu, G.; Feng, J. H.; Wang, X. F. Synthesis, crystal structure, and physical properties of

a barium(II) benzene-1, 2, 3-tricarboxylic acid complex. *Z. Anorg. Allg. Chem.* **2012**, *638* (6), 1047–1052.

(63) O'Keeffe, M.; Eddaoudi, M.; Li, H.; Reineke, T.; Yaghi, O. M. Frameworks for extended solids: Geometrical design principles. *J. Solid State Chem.* **2000**, *152* (1), 3–20.

(64) Duan, X.; Lin, J.; Li, Y.; Zhu, C.; Meng, Q. Syntheses, structures and properties of a series of organic–inorganic complexes based on methylenediisophthalic acid (H4MDIP). *CrystEngComm* **2008**, *10* (2), 207.

(65) Noro, S. I.; Mizutani, J.; Hijikata, Y.; Matsuda, R.; Sato, H.; Kitagawa, S.; Sugimoto, K.; Inubushi, Y.; Kubo, K.; Nakamura, T. Porous coordination polymers with ubiquitous and biocompatible metals and a neutral bridging ligand. *Nat. Commun.* **2015**, *6*, 1–9.

(66) Banerjee, D.; Zhang, Z.; Plonka, A. M.; Li, J.; Parise, J. B. A calcium coordination framework having permanent porosity and high CO2/N2 selectivity. *Cryst. Growth Des.* **2012**, *12* (5), 2162–2165.

(67) Han, L.; Qin, L.; Xu, L.; Zhou, Y.; Sun, J.; Zou, X. A novel photochromic calcium-based metal–organic framework derived from a naphthalene diimide chromophore. *Chem. Commun.* **2013**, *49* (4), 406–408.

(68) Caskey, S. R.; Wong-Foy, A. G.; Matzger, A. J. Dramatic tuning of carbon dioxide uptake via metal substitution in a coordination polymer with cylindrical pores. *J. Am. Chem. Soc.* **2008**, *130* (33), 10870–10871.

(69) Foo, M. L.; Horike, S.; Inubushi, Y.; Kitagawa, S. An Alkaline Earth I3O0 Porous Coordination Polymer: [Ba_2TMA(NO_3)(DMF)]. *Angew. Chem. Int. Ed.* **2012**, *51* (25), 6107–6111.

(70) Huang, Y. Q.; Cheng, H. Di; Guo, B. L.; Wan, Y.; Chen, H. Y.; Li, Y. K.; Zhao, Y. Four alkaline earth metal complexes with structural diversities induced by cation size. *Inorganica Chim. Acta* **2014**, *421*, 318–325.

(71) Douvali, A.; Papaefstathiou, G. S.; Gullo, M. P.; Barbieri, A.; Tsipis, A. C.; Malliakas, C. D.; Kanatzidis, M. G.; Papadas, I.; Armatas, G. S.; Hatzidimitriou, A. G.; et al. Alkaline Earth Metal Ion/Dihydroxy-Terephthalate MOFs: Structural Diversity and Unusual Luminescent Properties. *Inorg. Chem.* **2015**, *54* (12), 5813–5826.

(72) Shustova, N. B.; Cozzolino, A. F.; Reineke, S.; Baldo, M.; Dincă, M. Selective turn-on ammonia sensing enabled by high-temperature fluorescence in metal-organic

frameworks with open metal sites. *J. Am. Chem. Soc.* **2013**, *135* (36), 13326–13329.

(73) Murugavel, R.; Banerjee, S. First alkaline earth metal 3-aminobenzoate (3-aba) complex: 1-D polymeric $[Ca(3\text{-aba})_2(H_2O)_2]$nassembly. *Inorg. Chem. Commun.* **2003**, *6* (7), 810–814.

(74) Murugavel, R.; Anantharaman, G.; Krishnamurthy, D.; Sathiyendiran, M.; Walawalkar, M. G. Extended metal-organic solids based on benzenepolycarboxylic and aminobenzoic acids. *Proc. Indian Acad. Sci. Chem. Sci.* **2000**, *112* (3), 273–290.

(75) Falcão, E. H. L.; Naraso; Feller, R. K.; Wu, G.; Wudl, F.; Cheetham, A. K. Hybrid organic-inorganic framework structures: Influence of cation size on metal-oxygen-metal connectivity in the alkaline earth thiazolothiazoledicarboxylates. *Inorg. Chem.* **2008**, *47* (18), 8336–8342.

(76) Pichon, A.; Lazuen-Garay, A.; James, S. L. Solvent-free synthesis of a microporous metal–organic framework. *CrystEngComm* **2006**, *8* (3), 211.

(77) Friščić, T.; Reid, D. G.; Halasz, I.; Stein, R. S.; Dinnebier, R. E.; Duer, M. J. Ion- and liquid-assisted grinding: Improved mechanochemical synthesis of metal-organic frameworks reveals salt inclusion and anion templating. *Angew. Chem. Int. Ed.* **2010**, *49* (4), 712–715.

(78) Klimakow, M.; Klobes, P.; Thünemann, A. F.; Rademann, K.; Emmerling, F. Mechanochemical synthesis of metal-organic frameworks: A fast and facile approach toward quantitative yields and high specific surface areas. *Chem. Mater.* **2010**, *22* (18), 5216–5221.

(79) Dhankhar, S. S.; Kaur, M.; Nagaraja, C. M. Green Synthesis of a Microporous, Partially Fluorinated ZnII Paddlewheel Metal-Organic Framework: H_2/CO_2 Adsorption Behavior and Solid-State Conversion to a ZnO-C Nanocomposite. *Eur. J. Inorg. Chem.* **2015**, *2015* (34), 5669–5676.

(80) Garay, A. L.; Pichon, A.; James, S. L. Solvent-free synthesis of metal complexes. *Chem. Soc. Rev.* **2007**, *36* (6), 846.

(81) Friščić, T.; Fábián, L. Mechanochemical conversion of a metal oxide into coordination polymers and porous frameworks using liquid-assisted grinding (LAG). *CrystEngComm* **2009**, *11* (5), 743.

(82) Klimakow, M.; Klobes, P.; Rademann, K.; Emmerling, F. Characterization of

mechanochemically synthesized MOFs. *Microporous Mesoporous Mater.* **2012**, *154* (2012), 113–118.

(83) Scholz, G.; Abdulkader, A.; Kemnitz, E. Mechanochemical Synthesis and Characterization of Alkaline Earth Metal Terephthalates: $M(C_8H_4O_4)\cdot nH_2O$ (M = Ca, Sr, Ba). *Z. Anorg. Allg. Chem.* **2014**, *640* (2), 317–324.

(84) Scholz, G.; Emmerling, F.; Dreger, M.; Kemnitz, E. Mechanochemical synthesis and characterization of hydrated and dehydrated crystalline strontium terephtalates. *Z. Anorg. Allg. Chem.* **2013**, *639* (5), 689–693.

(85) James, S. L.; Adams, C. J.; Bolm, C.; Braga, D.; Collier, P.; Friščić, T.; Grepioni, F.; Harris, K. D. M.; Hyett, G.; Jones, W.; et al. Mechanochemistry: opportunities for new and cleaner synthesis. *Chem. Soc. Rev.* **2012**, *41* (1), 413–447.

(86) Friščić, T.; Halasz, I.; Štrukil, V.; Eckert-Maksić, M.; Dinnebier, R. E. Clean and Efficient Synthesis Using Mechanochemistry: Coordination Polymers, Metal-Organic Frameworks and Metallodrugs. *Croat. Chem. Acta* **2012**, *85* (3), 367–378.

(87) Al-Terkawi, A. -A.; Scholz, G.; Emmerling, F.; Kemnitz, E. Mechanochemical Synthesis, Characterization, and Structure Determination of New Alkaline Earth Metal-Tetrafluoroterephthalate Frameworks: $Ca(p\text{BDC-}F_4)\cdot 4H_2O$, $Sr(p\text{BDC-}F_4)\cdot 4H_2O$, and $Ba(p\text{BDC-}F_4)$. *Cryst. Growth Des.* **2016**, *16* (4), 1923–1933.

(88) Al-Terkawi, A.-A.; Scholz, G.; Buzanich, A. G.; Reinsch, S.; Emmerling, F.; Kemnitz, E. Ca- and Sr-tetrafluoroisophthalates: mechanochemical synthesis, characterization, and ab initio structure determination. *Dalton Trans.* **2017**, *46*, 6003–6012.

(89) Tröbs, L.; Emmerling, F. Mechanochemical synthesis and characterisation of cocrystals and metal organic compounds. *Faraday Discuss.* **2014**, *170* (25), 109–119.

(90) Al-Terkawi, A.-A.; Scholz, G.; Emmerling, F.; Kemnitz, E. Strontium-Coordination Polymers based on Tetrafluorophthalic and Phthalic acids: Mechanochemical Synthesis, ab initio Structures Determination, and Spectroscopic Characterization. *Dalton Trans.* **2017**, *46*, 12574–12587.

(91) Wilke, M.; Batzdorf, L.; Fischer, F.; Rademann, K.; Emmerling, F. Cadmium phenylphosphonates: preparation, characterisation and *in situ* investigation. *RSC Adv.* **2016**, *6* (42), 36011–36019.

(92) Mottillo, C.; Friščić, T. Advances in solid-state transformations of coordination bonds:

From the ball mill to the aging chamber. *Molecules* **2017**, *22* (1), 144.

(93) Boldyrev, V. V. Mechanochemistry and mechanical activation of solids. *Solid State Ionics* **1993**, *63–65* (C), 537–543.

(94) Takacs, L. The historical development of mechanochemistry. *Chem. Soc. Rev.* **2013**, *42* (18), 7649.

(95) Takacs, L. The mechanochemical reduction of AgCl with metals: Revisiting an experiment of M. Faraday. *J. Therm. Anal. Calorim.* **2007**, *90* (1), 81–84.

(96) Fox, P. G. Mechanically initiated chemical reactions in solids. *J. Mater. Sci.* **1975**, *10* (2), 340–360.

(97) Takacs, L. M.Carey Lea, the Father of mechanochemistry. *Bull. Hist. Chem.* **2003**, *28* (1), 26–34.

(98) Lea, M. C. IV . Disruption of the silver haloid molecule by mechanical force. *London, Edinburgh, Dublin Philos. Mag. J. Sci.* **2009**, *34* (July 2012), 37–41.

(99) Ostwald, W. *The Fundamental Principles of Chemistry: An Introduction to All Text-Books of Chemistry*; Longmans, Green and Co: New York, 1909.

(100) Tschakarov, C. G. uber den Mechanismus der mechanochemischen anorganischer Verbindungen Synthese Zusammensetzung der Metallkomponente. *J. Solid State Chem.* **1982**, *252*, 244–252.

(101) Linthorst, J. A. An overview: Origins and development of green chemistry. *Found. Chem.* **2010**, *12* (1), 55–68.

(102) Anastas, P. T.; Warner, J. C. *Green chemistry: theory and practice*; Oxford University Press Academic: Oxford, 2000.

(103) Anastas, P.; Eghbali, N. Green Chemistry: Principles and Practice. *Chem. Soc. Rev.* **2010**, *39* (1), 301–312.

(104) Reinsch, H. “Green” Synthesis of Metal-Organic Frameworks. *Eur. J. Inorg. Chem.* **2016**, *2016* (27), 4290–4299.

(105) Constable, D. J. C.; Curzons, A. D.; Cunningham, V. L. Metrics to “green” chemistry—which are the best? *Green Chem.* **2002**, *4* (6), 521–527.

(106) Gomes, W. P.; Dekeyser, W. Factors Influencing the Reactivity of Solids. In *Treatise on Solid State Chemistry*; Hannay, N. B., Ed.; Springer US: Boston, MA, MA, 1976; pp 61-113.

(107) Bridgman, P. W. Recent work in the field of high pressures. *Rev. Mod. Phys.* **1946**, *18* (1), 1–93.

(108) Gilman, J. J. During detonation chemistry may precede heat. *Mater. Sci. Technol.* **2006**, *22* (4), 430–437.

(109) Fink, V. M. A. X.; Hofmann, U. Oxydation von Metallen unter dem Einfluß der Reibung. *Z. Anorg. Allg. Chem.* **1933**, *210*, 100–104.

(110) Harris, K. D. M. Mechanochemical synthesis: How grinding evolves. *Nat. Chem.* **2013**, *5* (1), 12–14.

(111) Friščić, T.; Halasz, I.; Beldon, P. J.; Belenguer, A. M.; Adams, F.; Kimber, S. A. J.; Honkimäki, V.; Dinnebier, R. E. Real-time and in situ monitoring of mechanochemical milling reactions. *Nat. Chem.* **2013**, *5* (1), 66–73.

(112) Batzdorf, L.; Fischer, F.; Wilke, M.; Wenzel, K.-J.; Emmerling, F. Direct In Situ Investigation of Milling Reactions Using Combined X-ray Diffraction and Raman Spectroscopy. *Angew. Chem. Int. Ed.* **2015**, *54* (6), 1799–1802.

(113) Lynch, A. J.; Rowland, C. A. *The History of Grinding*; The Society for Mining, Metallurgy, and Exploration, Inc.: Colorado, 2015.

(114) Takacs, L. Quicksilver from Cinnabar: The first documented mechanochemical reaction? *Jom-Journal Miner. Met. Mater. Soc.* **2000**, *52* (1), 12–13.

(115) Burmeister, C. F.; Kwade, A. Process engineering with planetary ball mills. *Chem. Soc. Rev.* **2013**, *42* (18), 7660.

(116) Do, J. L.; Friščić, T. Chemistry 20: Developing a New, Solvent-Free System of Chemical Synthesis Based on Mechanochemistry. *Synlett* **2017**, *28* (16), 2066–2092.

(117) Watts, A. E.; Maruyoshi, K.; Hughes, C. E.; Brown, S. P.; Harris, K. D. M. Combining the Advantages of Powder X-ray Diffraction and NMR Crystallography in Structure Determination of the Pharmaceutical Material Cimetidine Hydrochloride. *Cryst. Growth Des.* **2016**, *16* (4), 1798–1804.

(118) Van De Streek, J.; Neumann, M. A. Validation of molecular crystal structures from powder diffraction data with dispersion-corrected density functional theory (DFT-D). *Acta Crystallogr. Sect. B Struct. Sci. Cryst. Eng. Mater.* **2014**, *70* (6), 1020–1032.

(119) Bygrave, P. J.; Case, D. H.; Day, G. M. Is the equilibrium composition of mechanochemical reactions predictable using computational chemistry?

Faraday Discuss. **2014**, *170*, 41–57.

(120) Biradha, K.; Ramanan, A.; Vittal, J. J. Coordination polymers versus metal−organic frameworks. *Cryst. Growth Des.* **2009**, *9* (7), 2969–2970.

(121) Rowsell, J. L. C.; Yaghi, O. M. Metal-organic frameworks: A new class of porous materials. *Microporous Mesoporous Mater.* **2004**, *73* (1–2), 3–14.

(122) Férey, G. Hybrid porous solids: past, present, future. *Chem. Soc. Rev.* **2008**, *37* (1), 191-214.

(123) Janiak, C.; Vieth, J. K. MOFs, MILs and more: concepts, properties and applications for porous coordination networks (PCNs). *New J. Chem.* **2010**, *34* (11), 2366.

(124) Howarth, A. J.; Peters, A. W.; Vermeulen, N. A.; Wang, T. C.; Hupp, J. T.; Farha, O. K. Best practices for the synthesis, activation, and characterization of metal−organic frameworks. *Chem. Mater.* **2017**, *29* (1), 26–39.

(125) Horcajada, P.; Gref, R.; Baati, T.; Allan, P. K.; Maurin, G.; Couvreur, P.; Férey, G.; Morris, R. E.; Serre, C. Metal-organic frameworks in biomedicine. *Chem. Rev.* **2012**, *112* (2), 1232–1268.

(126) Keskin, S.; Kizilel, S. Biomedical Applications of Metal Organic Frameworks. *Ind. Eng. Chem. Res.* **2011**, *50* (4), 1799–1812.

(127) Cai, W.; Chu, C. C.; Liu, G.; Wáng, Y. X. J. Metal-Organic Framework-Based Nanomedicine Platforms for Drug Delivery and Molecular Imaging. *Small* **2015**, *11* (37), 4806–4822.

(128) Yang, C.; Wang, X.; Omary, M. A. Fluorous metal-organic frameworks for high-density gas adsorption. *J. Am. Chem. Soc.* **2007**, *129* (50), 15454–15455.

(129) Yang, C.; Wang, X.; Omary, M. A. Crystallographic observation of dynamic Gas adsorption sites and thermal expansion in a breathable fluorous metal-organic framework. *Angew. Chem. Int. Ed.* **2009**, *48* (14), 2500–2505.

(130) Hulvey, Z.; Sava, D. A.; Eckert, J.; Cheetham, A. K. Hydrogen storage in a highly interpenetrated and partially fluorinated metal-organic framework. *Inorg. Chem.* **2011**, *50* (2), 403–405.

(131) Chun, H.; Dybtsev, D. N.; Kim, H.; Kim, K. Synthesis, X-ray crystal structures, and gas sorption properties of pillared square grid nets based on paddle-wheel motifs: Implications for hydrogen storage in porous materials. *Chem. - A Eur. J.* **2005**, *11* (12),

3521–3529.

(132) Jhung, S. H.; Kim, H. K.; Yoon, J. W.; Chang, J. S. Low-temperature adsorption of hydrogen on nanoporous aluminophosphates: Effect of pore size. *J. Phys. Chem. B* **2006**, *110* (19), 9371–9374.

(133) Dincă, M.; Long, J. R. Strong H_2 binding and selective gas adsorption within the microporous coordination solid $Mg_3(O_2C\text{-}C_{10}H_6\text{-}CO_2)_3$. *J. Am. Chem. Soc.* **2005**, *127* (26), 9376–9377.

(134) Jiang, L.; Meng, X. R.; Xiang, H.; Ju, P.; Zhong, D. C.; Lu, T. B. Variations of structures and gas sorption properties of three coordination polymers induced by fluorine atom positions in azamacrocyclic ligands. *Inorg. Chem.* **2012**, *51* (3), 1874–1880.

(135) Hulvey, Z.; Falcao, E. H. L.; Eckert, J.; Cheetham, A. K. Enhanced H_2 adsorption enthalpy in the low-surface area, partially fluorinated coordination polymer Zn_5(triazole)$_6$(tetrafluoroterephthalate)$_2(H_2O)_2 \cdot 4H_2O$. *J. Mater. Chem.* **2009**, *19* (25), 4307.

(136) Hulvey, Z.; Wragg, D. S.; Lin, Z.; Morris, R. E.; Cheetham, A. K. Ionothermal synthesis of inorganic–organic hybrid materials containing perfluorinated aliphatic dicarboxylate ligands. *Dalton Trans.* **2009**, *0* (7), 1131.

(137) Zhang, X.; Huang, Y.-Y.; Lin, Q.-P.; Zhang, J.; Yao, Y.-G. Using alkaline-earth metal ions to tune structural variations of 1,3,5-benzenetricarboxylate coordination polymers. *Dalton Trans.* **2013**, *42* (6), 2294–2301.

(138) Yang, D. L.; Zhang, X.; Yang, J. X.; Yao, Y. G.; Zhang, J. Alkali/alkaline earth metal and solvents-regulated construction of novel heterometallic coordination polymers based on a semirigid ligand and tetranuclear metal clusters. *Inorganica Chim. Acta* **2014**, *423*, 62–71.

(139) Côté, A. P.; Shimizu, G. K. H. Coordination Solids via Assembly of Adaptable Components: Systematic Structural Variation in Alkaline Earth Organosulfonate Networks. *Chem. - A Eur. J.* **2003**, *9* (21), 5361–5370.

(140) Blair, L. H.; Colakel, A.; Vrcelj, R. M.; Sinclair, I.; Coles, S. J. Metal–organic fireworks: MOFs as integrated structural scaffolds for pyrotechnic materials. *Chem. Commun.* **2015**, *51* (61), 12185–12188.

(141) Usman, M.; Lee, C.-H.; Hung, D.-S.; Lee, S.-F.; Wang, C.-C.; Luo, T.-T.; Zhao, L.; Wu, M.-

K.; Lu, K.-L. Intrinsic low dielectric behaviour of a highly thermally stable Sr-based metal–organic framework for interlayer dielectric materials. *J. Mater. Chem. C* **2014**, *2* (19), 3762–3768.

(142) Zhang, Y.; Niu, Y.; Wang, M.-Q.; Yang, J.; Lu, S.; Han, J.; Bao, S.-J.; Xu, M. Exploration of a calcium–organic framework as an anode material for sodium-ion batteries. *Chem. Commun.* **2016**, *52* (64), 9969–9971.

(143) Groom, C. R.; Allen, F. H.; Henderson, S. The Cambridge Structural Database (CSD). *Ref. Modul. Chem. Mol. Sci. Chem. Eng.* **2013**, *B72*, 171–179.

(144) Gupta, M. P.; Sinha, R. P. Ca Phthalate monohydrate (Ref. was entered manually/pdf is not avaliable). *Cryst. Struct. Commun.* **1975**, *4*, 207–210.

(145) Schuckmann, W.; Fuess, H.; Bats, J. W. Refinement of the structure of calcium phthalate monohydrate. *Acta Crystallogr. Sect. B Struct. Crystallogr. Cryst. Chem.* **1978**, *34* (12), 3754–3756.

(146) Zhang, X.; Huang, Y. Y.; Zhang, M. J.; Zhang, J.; Yao, Y. G. A series of Ca(II) or Ba(II) inorganic-organic hybrid frameworks based on aromatic polycarboxylate ligands with the inorganic M-O-M (M = Ca, Ba) connectivity from 1D to 3D. *Cryst. Growth Des.* **2012**, *12* (6), 3231–3238.

(147) Dale, S. H.; Elsegood, M. R. J. $\{[Ca_5(C_8H_4O_4)_5(H_2O)_9]\cdot 8H_2O\}_n$: The first crystallographically characterized non-transition metal salt of isophthalic acid. *Acta Crystallogr. Sect. C Cryst. Struct. Commun.* **2003**, *59* (12), 540–542.

(148) Yu, L. C.; Chen, Z. F.; Liang, H.; Zhou, C. S.; Li, Y. A triple helical calcium-based coordination polymer with strong blue fluorescent emission. *J. Mol. Struct.* **2005**, *750* (1–3), 35–38.

(149) Matsuzaki, T.; Iitaka, Y. The crystal structure of calcium terephthalate trihydrate. *Acta Crystallogr. Sect. B Struct. Crystallogr. Cryst. Chem.* **1972**, *28* (7), 1977–1981.

(150) Groeneman, R. H.; Atwood, J. L. Terephthlate bridged coordination polymers based upon group two metals. *Cryst. Eng.* **1999**, *2* (4), 241–249.

(151) Dale, S. H.; Elsegood, M. R. J. *catena* -Poly[[diaquacalcium(II)]-μ_3-terephthalato-μ_2-aqua] at 150 K. *Acta Crystallogr. Sect. E Struct. Reports Online* **2003**, *59* (8), m586-m587.

(152) Mazaj, M.; Mali, G.; Rangus, M.; Žunkovic, E.; Kaučic, V.; Logar, N. Z. Spectroscopic

studies of structural dynamics induced by heating and hydration: A case of calcium-terephthalate metal-organic framework. *J. Phys. Chem. C* **2013**, *117* (15), 7552–7564.

(153) Blair, L. H.; Colakel, A.; Vrcelj, R. M.; Sinclair, I.; Coles, S. J. Metal–organic fireworks: MOFs as integrated structural scaffolds for pyrotechnic materials. *Chem. Commun.* **2015**, *51* (61), 12185–12188.

(154) Yang, L.; Zhao, D.; Li, G. Poly[μ-aqua-μ4-terephthalato-strontium]. *Acta Crystallogr. Sect. E Struct. Reports Online* **2011**, *67* (2), m282.

(155) Smets, D.; Sobieray, M.; Ruschewitz, U. A new alkaline earth metal tetrafluoroterephthalate: [Ba(tfBDC)(DMF)(EtOH)]. *IUCrData* **2016**, *1* (9), x161409.

(156) Lo, S. M. F.; Chui, S. S. Y.; Williams, I. D. Barium terephthalate, a three-dimensional coordination polymer with 7:7 cation-anion connectivity. *Acta Crystallogr. Sect. C Cryst. Struct. Commun.* **1998**, *54* (12), 1846–1848.

(157) Murugavel, R.; Karambelkar, V. V; Anantharaman, G.; Walawalkar, M. G. Synthesis, Spectral Characterization, and Structural Studies of 2-Aminobenzoate Complexes of Divalent Alkaline Earth Metal Ions: X-ray Crystal Structures of $[Ca(2\text{-aba})_2(OH_2)_3]\infty$, $[\{Sr(2\text{-aba})_2(OH_2)_2\},H_2O]\infty$, and $[Ba(2\text{-aba})_2(OH_2)]\infty$ (2-abaH = 2-$NH_2C_6H_4COOH$). *Inorg. Chem.* **2000**, *39* (7), 1381–1390.

(158) Cheung, E. Y.; Kitchin, S. J.; Harris, K. D. M.; Imai, Y.; Tajima, N.; Kuroda, R. Direct Structure Determination of a Multicomponent Molecular Crystal Prepared by a Solid-State Grinding Procedure. *J. Am. Chem. Soc.* **2003**, *125* (48), 14658–14659.

(159) Rissanen, K. *Advanced X-Ray Crystallography*, 1st ed.; Springer-Verlag Berlin Heidelberg, 2012; Vol. 315.

(160) Yakovenko, A. A.; Reibenspies, J. H.; Bhuvanesh, N.; Zhou, H. C. Generation and applications of structure envelopes for porous metal-organic frameworks. *J. Appl. Crystallogr.* **2013**, *46* (2), 346–353.

(161) Gándara, F.; Bennett, T. D. Crystallography of metal-organic frameworks. *IUCrJ* **2014**, *1*, 563–570.

(162) JCPDS-ICDD, International Centre for Diffraction Data: PDF-2 Database (Sets 1–51 plus 70–89). International Centre for Diffraction Data: PA 19073–3273 USA 2001.

(163) David, W. I. F.; Shankland, K.; van de Streek, J.; Pidcock, E.; Motherwell, W. D. S.; Cole, J. C. *DASH* : a program for crystal structure determination from powder diffraction

data. *J. Appl. Crystallogr.* **2006**, *39* (6), 910–915.

(164) Cheary, R. W.; Coelho, A. A.; Cline, J. P. Fundamental parameters line profile fitting in laboratory diffractometers. *J. Res. Natl. Inst. Stand. Technol.* **2004**, *109* (1), 1.

(165) Boultif, A.; Louër, D. Powder pattern indexing with the dichotomy method. *J. Appl. Crystallogr.* **2004**, *37* (5), 724–731.

(166) Le Bail, A.; Duroy, H.; Fourquet, J. L. Ab-initio structure determination of $LiSbWO_6$ by X-ray powder diffraction. *Mater. Res. Bull.* **1988**, *23* (3), 447–452.

(167) Le Bail, A. Whole powder pattern decomposition methods and applications: A retrospection. *Powder Diffr.* **2005**, *20* (4), 316–326.

(168) Altomare, A.; Corriero, N.; Cuocci, C.; Moliterni, A.; Rizzi, R. The hybrid big bang-big crunch method for solving crystal structure from powder diffraction data. *J. Appl. Crystallogr.* **2013**, *46* (3), 779–787.

(169) Altomare, A.; Corriero, N.; Cuocci, C.; Falcicchio, A.; Moliterni, A.; Rizzi, R. EXPO software for solving crystal structures by powder diffraction data: Methods and application. *Cryst. Res. Technol.* **2015**, *50* (9–10), 737–742.

(170) Langford, J. I.; Louër, D. Powder diffraction. *Rep. Prog. Phys.* **1996**, *59* (2), 131–234.

(171) Cory, D. G.; Ritchey, W. M. Suppression of signals from the probe in bloch decay spectra. *J. Magn. Reson.* **1988**, *80* (1), 128–132.

(172) Massiot, D.; Fayon, F.; Capron, M.; King, I.; Le Calvé, S.; Alonso, B.; Durand, J. O.; Bujoli, B.; Gan, Z.; Hoatson, G. Modelling one- and two-dimensional solid-state NMR spectra. *Magn. Reson. Chem.* **2002**, *40* (1), 70–76.

(173) Brunauer, S.; Emmett, P. H.; Teller, E. Adsorption of Gases in Multimolecular Layers. *J. Am. Chem. Soc.* **1938**, *60* (2), 309–319.

(174) Fagerlund, G. Determination of specific surface by the BET method. *Matériaux Constr.* **1973**, *6* (3), 239–245.

(175) ISO 9277. *Determination of the specific surface area of solids by gas adsorption — BET method*; 2010; Vol. E.

(176) Ravel, B.; Newville, M. ATHENA, ARTEMIS, HEPHAESTUS: Data analysis for X-ray absorption spectroscopy using IFEFFIT. *J. Synchrotron Radiat.* **2005**, *12* (4), 537–541.

(177) Rehr, J. J.; Kas, J. J.; Vila, F. D.; Prange, M. P.; Jorissen, K. Parameter-free calculations of X-ray spectra with FEFF9. *Phys. Chem. Chem. Phys.* **2010**, *12* (21), 5503.

(178) Fawcett, T. G.; Kabekkodu, S. N.; Blanton, J. R.; Blanton, T. N. Chemical analysis by diffraction: The Powder Diffraction File™. *Powder Diffr.* **2017**, *32* (2), 63–71.

(179) Orthaber, A.; Seidel, C.; Belaj, F.; Albering, J. H.; Pietschnig, R.; Ruschewitz, U. Optimized synthesis of tetrafluoroterephthalic acid: A versatile linking ligand for the construction of new coordination polymers and metal-organic frameworks. *Inorg. Chem.* **2010**, *49* (20), 9350–9357.

(180) Wang, Z.; Kravtsov, V. C.; Walsh, R. B.; Zaworotko, M. J. Guest-dependent cavities in two-dimensional metal - Organic frameworks sustained by tetrafluoro-1,3-benzenedicarboxylate. *Cryst. Growth Des.* **2007**, *7* (6), 1154–1162.

(181) D. S. Sake Gowda and Reuben Rudman. Tetrafluorophthalie Acid. *Acta Cryst.* **1983**, *C39* (3), 250–253.

(182) Bailey, M.; Brown, C. J. The crystal structure of terephthalic acid. *Acta Crystallogr.* **1967**, *22* (3), 387–391.

(183) McCormick, L. J.; Morris, S. A.; Slawin, A. M. Z.; Teat, S. J.; Morris, R. E. Coordination polymers of 5-substituted isophthalic acid. *CrystEngComm* **2016**, *18* (7), 1123–1132.

(184) Ermer, O. Ungewöhnliches Strukturmerkmal kristalliner Phthalsäure. *Helv. Chim. Acta* **1981**, *64* (6), 1902–1909.

(185) Liao, X. J.; Guo, W.; Xu, S. H. 2-Amino-3,4,5,6-tetra-fluoro-benzoic acid. *Acta Crystallogr. Sect. E Struct. Reports Online* **2011**, *67* (7), o1732.

(186) Voogd. J, Verzijl. B. H. M, D. A. J. M. m-Aminobenzoie Acid. *Acta Crystallogr. Sect. B* **1980**, *36*, 2805–2806.

(187) Fernández-Bertrán, J.; Castellanos-Serra, L.; Yee-Madeira, H.; Reguera, E. Proton Transfer in Solid State: Mechanochemical Reactions of Imidazole with Metallic Oxides. *J. Solid State Chem.* **1999**, *147* (2), 561–564.

(188) Byrn, S. R.; Xu, W.; Newman, A. W. Chemical reactivity in solid-state pharmaceuticals: Formulation implications. *Adv. Drug Deliv. Rev.* **2001**, *48* (1), 115–136.

(189) Fujii, K.; Garay, A. L.; Hill, J.; Sbircea, E.; Pan, Z.; Xu, M.; Apperley, D. C.; James, S. L.; Harris, K. D. M. Direct structure elucidation by powder X-ray diffraction of a metal–organic framework material prepared by solvent-free grinding. *Chem. Commun.* **2010**, *46* (40), 7572.

(190) Friščić, T.; Halasz, I.; Strobridge, F. C.; Dinnebier, R. E.; Stein, R. S.; Fábián, L.; Curfs, C.

A rational approach to screen for hydrated forms of the pharmaceutical derivative magnesium naproxen using liquid-assisted grinding. *CrystEngComm* **2011**, *13* (9), 3125.

(191) Dreger, M.; Scholz, G.; Kemnitz, E. An easy access to nanocrystalline alkaline earth metal fluorides - Just by shaking. *Solid State Sci.* **2012**, *14* (4), 528–534.

(192) Garroni, S.; Takacs, L.; Leng, H.; Delogu, F. Kinetics of the mechanochemical synthesis of alkaline-earth metal amides. *Chem. Phys. Lett.* **2014**, *608* (May), 80–83.

(193) Wang, X. L.; Liu, Z. Q.; Stevens-Kalceff, M. A.; Riesen, H. Mechanochemical preparation of nanocrystalline BaFCl doped with samarium in the 2+ oxidation state. *Inorg. Chem.* **2014**, *53* (17), 8839–8841.

(194) Irisova, I.; Kiiamov, A.; Korableva, S.; Rodionov, A.; Tayurskii, D.; Yusupov, R. Structure and Metastability of MF2 (M = Ca, Sr, Ba) Fine Powders Mechanochemically Doped with Er3+ Ions. *Appl. Magn. Reson.* **2015**, *2* (46), 515–522.

(195) Toroz, D.; Rosbottom, I.; Turner, T. D.; Corzo, D. M. C.; Hammond, R. B.; Lai, X.; Roberts, K. J. Towards an understanding of the nucleation of alpha-para amino benzoic acid from ethanolic solutions: a multi-scale approach. *Faraday Discuss.* **2015**, *179*, 79–114.

(196) Marković, Z.; Badjuk, D.; Gutman, I. Geometry and conformations of benzenecarboxylic acids. *J. Serbian Chem. Soc.* **2004**, *69* (11), 877–882.

(197) Hulvey, Z.; Furman, J. D.; Turner, S. A.; Tang, M.; Cheetham, A. K. Dimensionality trends in metal-organic frameworks containing perfluorinated or nonfluorinated benzenedicarboxylates. *Cryst. Growth Des.* **2010**, *10* (5), 2041–2043.

(198) Flett, M. S. C. 216. The characteristic infra-red frequencies of the carboxylic acid group. *J. Chem. Soc.* **1951**, No. 62, 962–967.

(199) González-Sánchez, F. Infra-red spectra of the benzene carboxylic acids. *Spectrochim. Acta* **1958**, *12* (1), 17–33.

(200) Al-Terkawi, A.-A.; Scholz, G.; Emmerling, F.; Kemnitz, E. Ca-Tetrafluorophthalate and Sr-Isophthalate: Mechanochemical Synthesis and Characterization in Comparison with other Ca-and Sr-Coordination Polymers. *Dalton Trans.* **2018**, *Accepted*.

(201) Venyaminov, S. Y.; Prendergast, F. G. Water (H2O and D2O) molar absorptivity in the 1000-4000 cm-1range and quantitative infrared spectroscopy of aqueous solutions. *Anal. Biochem.* **1997**, *248* (2), 234–245.

(202) Stosiek, C.; Scholz, G.; Schroeder, S. L. M.; Kemnitz, E. Structure and properties of

noncrystalline aluminum oxide-hydroxide fluorides. *Chem. Mater.* **2010**, *22* (7), 2347-2356.

(203) Deacon, G. B.; Phillips, R. J. Relationships between the carbon-oxygen stretching frequencies of carboxylato complexes and the type of carboxylate coordination. *Coord. Chem. Rev.* **1980**, *33* (3), 227–250.

(204) Al-Terkawi, A.-A.; Scholz, G.; Prinz, C.; Zimathies, A.; Emmerling, F.; Kemnitz, E. Hydrated and Dehydrated Ca-Coordination Polymers based on Benzene-Dicarboxylates: Mechanochemical Synthesis, Structures Refinement, and Spectroscopic Characterization. *CrystEngComm* **2018**, *20*, 946–961.

(205) Deng, Z.-P.; Gao, S.; Huo, L.-H.; Zhao, H. Poly[strontium(II)-μ2-aqua-μ5-4-carboxylatophenoxyacetato]. *Acta Crystallogr. Sect. C Cryst. Struct. Commun.* **2005**, *61* (12), m523–m525.

(206) Al-Terkawi, A.-A.; Scholz, G.; Emmerling, F.; Kemnitz, E. Barium Coordination Polymers based on Fluorinated and Fluorine-free Benzene-Dicarboxylates: Mechanochemical Synthesis and Spectroscopic Characterization. *Solid State Sci.* **2018**, *79*, 99–108.

(207) Smith, R. A. Ammonium Hy drogen Phthalate Hemihydrate. *Acta Cryst.* **1977**, *B33*, 1594–1596.

(208) Cingi, M. B.; Lanfredi, M. A. M.; Tiripicchio, A.; Camellini, M. T. The Crystal and Molecular Structure of Barium Diaquadi(o-phthalato)cuprate(II) Dihydrate. An Example of the Chelating Behaviour of the o-Phthalate Anion. *Acta Cryst.* **1978**, *B34*, 774–778.

(209) Hall, C. D.; Hinde, N. J.; Nyburg, S. C. Di-2-(2-methoxyethoxy)ethyl phthalate as a bi-brachial podand: complex formation with mono- and divalent cations. *J. Organomet. Chem.* **1997**, *531*, 73–79.

(210) Williams, C. A.; Blake, A. J.; Wilson, C.; Hubberstey, P.; Schröder, M. Novel metal-organic frameworks derived from group II metal cations and aryldicarboxylate anionic ligands. *Cryst. Growth Des.* **2008**, *8* (3), 911–922.

(211) Chiari, G. On metal–oxygen coordination. A statistical method to determine coordination number. I. Calcium. *Acta Crystallogr. Sect. B* **1990**, *46* (6), 717–723.

(212) Demadis, K. D.; Sallis, J. D.; Raptis, R. G.; Baran, P. A crystallographically characterized nine-coordinate calcium-Phosphocitrate complex as calcification inhibitor in vivo. *J. Am. Chem. Soc.* **2001**, *123* (41), 10129–10130.

(213) Pan, L.; Frydel, T.; Sander, M. B.; Huang, X.; Li, J. The effect of pH on the dimensionality of coordination polymers. *Inorg. Chem.* **2001**, *40* (6), 1271–1283.

(214) Chen, S.; Shuai, Q.; Gao, S. Two three-dimensional metal-organic frameworks constructed from alkaline earth metal cations (Sr and Ba) and 5-nitroisophthalicacid - Synthesis, charaterization, and thermochemistry. *Z. Anorg. Allg. Chem.* **2008**, *634* (9), 1591–1596.

(215) Werner, C.; Kemnitz, E.; Worzala, H.; Trojanov, S. Synthesis and Structure of $Ba(HSO_4)_2(H_2SO_4)_3$ and $Sr(HSO_4)_2(H_2SO_4)$. *Z. Naturforsch. B* **1996**, *51* (7), 952–958.

A. Appendices

A1. Organic Linkers

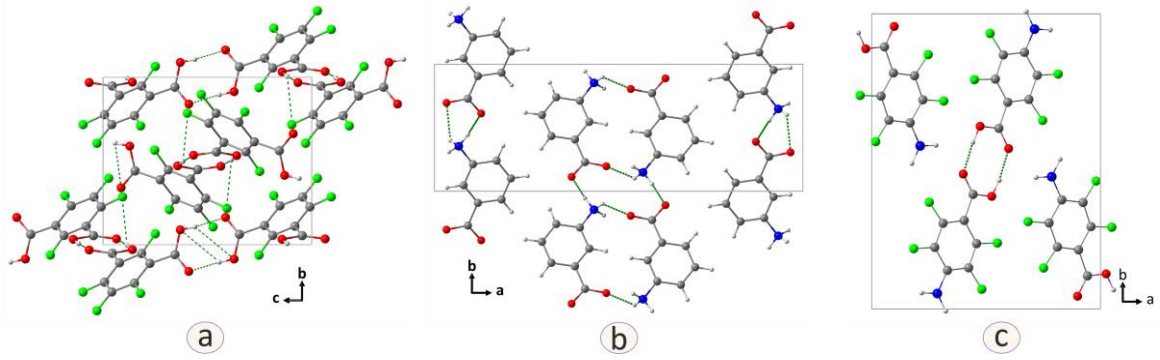

Figure A.1: The refined crystal structures of organic ligands. (a) H_2*m*BDC-F_4. (b) *m*ABAH (polymorph III). The asymmetric unit is composed of one zwitterion. (c) *p*ABAH-F_4. **Color code*: Carbon (grey), fluorine (bright green), oxygen (red), nitrogen (blue), and hydrogen (light grey). The hydrogen bonds are represented as dashed green lines.

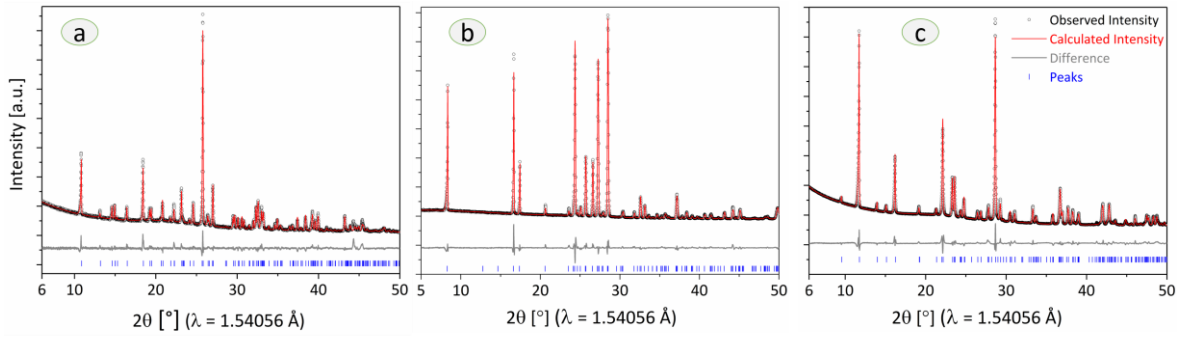

Figure A.2: Rietveld refinements for the crystal structures of H_2*m*BDC-F_4 (a), *m*ABAH (b), *p*ABAH-F_4 (c).

Table A.1: Crystal data derived from the refined crystal structures of the organic linkers.

	H_2*m*BDC-F_4	*m*ABAH (III)	*p*ABAH-F_4
Formula	$C_8H_2F_4O_4$	$C_7H_7O_2N$	$C_7H_3F_4O_2N$
F. weight (g/mol)	238.09	137.14	209.10
S. group	$P2_1/n$ (14)	$P2_1/c$ (14), transforms from ($P2_1/a$)	$P2_1/c$ (14), transforms from ($P2_1/a$)
Asym. unit	monomer	monomer, zwitterion	monomer, non-zwitterion
Cell lengths (Å): a, b, c	9.028(2) 8.580(2) 11.403(4)	21.423(5) 7.320(2) 21.406(2)	11.838(7) 15.029(10) 11.930(8)
Cell Angles (°): α, β, γ	90, 109.647(2), 90	90, 169.845(2), 90	90, 159.463(4), 90
Cell volume ($Å^3$)	831.96(4)	591.83(3)	744.67(8)
Z	4	4	4
Cell mass (g/mol)	952.38	548.54	836.39
R_{wp}, R_p, R_{Bragg}, GOF	7.26, 4.66, 4.847, 2.19	6.63, 4.42, 2.863, 3.55	3.91, 2.49, 1.771, 5.21
D. (g/cm^3)	1.901	1.54(8)	1.86(2)

A2. Results of Elemental Analysis

Table A.2: Results of elemental analysis of the hydrated compounds as-synthesized and after thermal post-treatment.

Compounds	C% found (calc.)	H% found(calc.)	F% found (calc.)	N% found (calc.)
Ca- and Sr-FCPs				
[Ca(*p*BDC-F_4)(H_2O)$_4$] (**1**)	28.4 (27.6)	2.0 (2.3)	17.9 (21.8)	-
[Sr(*p*BDC-F_4)(H_2O)$_4$] (**2**)	24.8 (24.1)	1.7 (2.0)	16.1 (19.2)	-
[{Ca(*m*BDC-F_4)(H_2O)$_2$}·H_2O] (**3**)	28.9 (29.1)	1.8 (1.8)	20.4 (23.0)	-
(**3-H_2O**), 240 °C	33.3 (34.8)	0.5 (0)	25.2 (27.5)	-
[{Sr(*m*BDC-F_4)(H_2O)$_2$}·H_2O] (**4**)	25.3 (25.4)	1.5 (1.6)	17.6 (20.1)	-
(**4-H_2O**), 240 °C	27.6 (29.7)	0.5 (0)	19.4 (23.5)	-
[Ca(*o*BDC-F_4)(H_2O)$_2$] (**5**)	31.1 (30.7)	1.1 (1.3)	24 (24.3)	-
(**5-H_2O**), 300 °C	33.5 (34.8)	0.5 (0)	32.4 (27.5)	-
[Sr(*o*BDC-F_4)(H_2O)$_2$] (**6**)	26.5 (26.7)	0.95 (1.1)	19.4 (21.1)	-
(**6-H_2O**), 300 °C	26.8 (29.7)	0.7 (0)	26.7 (23.5)	-
Ca- and Sr-CPs				
[Ca(*m*BDC)(H_2O)$_{3.4}$] (**8**)	36.9 (35.9)	3.09 (1.96)	-	-
(**8-H_2O**), 240 °C	41.03 (47.01)	3.09 (1.96)	-	-
[{Sr(*m*BDC)(H_2O)$_{3.4}$] (**9**)	30.1 (30.7)	3.3 (3.4)	-	-
(**9-H_2O**), 240 °C	34.7 (38.1)	2.4 (1.6)	-	-
[Ca(*o*BDC)(H_2O)$_1$] (**10**)	43.1 (43.2)	2.7 (2.7)	-	-
[Ca(*o*BDC)] (**10-H_2O**), 290 °C	46.5 (47.01)	2.02 (2.0)	-	-
[{Sr(*o*BDC)(H_2O)$_2$}·H_2O] (**11**)	30.4 (31.4)	3.1 (3.3)	-	-
(**11-H_2O**), 400 °C	37.4 (38.1)	1.5 (1.6)	-	-
Ba-FCPs and Ba-CPs				
[Ba(*p*BDC-F_4)(H_2O)$_{0.5}$] (**12**)	24.5 (25.1)	0.2 (0.26)	13.3 (19.97)	-
[Ba(*m*BDC-F_4)(H_2O)$_{0.5}$] (**13**)	29.5 (25.1)	0.2 (0.26)	15.5 (20.0)	-

Compounds	C% found (calc.)	H% found(calc.)	F% found (calc.)	N% found (calc.)
(**13-H_2O**), 240 °C	24.9 (25.7)	0 (0)	15.9 (20.3)	-
[Ba(*o*BDC-F_4)(H_2O)$_{1.5}$] (**14**)	24.3 (24)	0.7 (0.7)	19.5 (19)	-
(**14-H_2O**), 290 °C	22.8 (25.7)	0.5 (0)	22.2 (20.0)	-
[Ba(*m*BDC)(H_2O)$_{2.5}$] (**15**)	22.8 (27.7)	2.7 (2.6)	-	-
(**15-H_2O**), 240 °C	29.9 (31.8)	1.7 (1.3)	-	-
[Ba(*o*BDC)(H_2O)$_1$] (**16**)	29 (30.05)	31 (31.8)	-	-
(**16-H_2O**), 290 °C	1.6 (1.9)	1.3 (1.3)	-	-
M^{II}-Anthranilates				
[Ca(*o*ABA)$_2$(H_2O)$_3$] (**17**)	46.05 (45.9)	4.9 (4.9)	-	7.6 (7.6)
(**17-H_2O**), 200 °C	53.7 (53.8)	3.8 (3.8)	-	8.9 (8.96)
[{Sr(*o*ABA) $_2$(H_2O)$_2$}·H_2O] (**18**)	36.4 (40.6)	4.3 (4.3)	-	6.1 (6.8)
(**18-H_2O**), 200 °C	46.5 (46.7)	3.2 (3.3)	-	7.7 (7.8)
[Ba(*o*ABA)$_2$(H_2O)$_1$] (**19**)	37.1 (39.3)	3.2 (3.3)	-	6.5 (6.5)
(**19-H_2O**), 200 °C	40.7 (41.01)	2.8 (2.9)	-	6.8 (6.8)
In progress				
[Mg(*o*ABA)$_2$]	56.5 (56.5)	4.05 (4.05)	-	9.4 (9.4)
M^{II}-(4amino-tetrafluorobenzoates)				
[Ca(*p*ABA-F_4)$_2$(H_2O)$_n$]	48.02	1.04		8.2
[{Sr(*p*ABA-F_4) $_2$(H_2O)$_2$]	28.1 (31.12)	1.02 (1.5)	(28.2)	5.2 (5.2)
[Ba(*p*ABA-F_4)$_2$(H_2O)$_2$]	27.5 (28.5)	1.2 (1.4)	(25.8)	4.6 (4.7)
M^{II}-(2amino-tetrafluorobenzoates)				
[Ca(*o*ABA-F_4)$_2$(H_2O)$_2$]	34.1 (34.1)	1.5 (1.6)	18.9 (30.9)	5.8 (5.7)
[Ca(*o*ABA-F_4)$_2$], 200 °C	35.9 (36.8)	1.03 (0.9)	21.4 (33.3)	6.0 (6.1)
[Sr(*o*ABA-F_4)$_2$(H_2O)$_2$]	31.2 (31.1)	1.8 (1.5)	17.5 (28.2)	5.3 (5.2)
[Ba(*o*ABA-F_4)$_2$(H_2O)$_2$]	28.1 (28.5)	1.3 (1.4)	15.6 (25.8)	4.7 (4.7)
M^{II}-(4aminobenzoates)				
[Ca(*p*ABA)$_2$(H_2O)$_n$]	31.9	2.3	-	5.3
[Sr(*p*ABA)$_2$(H_2O)$_2$]	40.2 (42.4)	3.9 (4.04)	-	6.9 (7.1)
[{Ba(*p*ABA)$_2$(H_2O)$_2$} 0.45(H_2O)]	34.4 (37.03)	3.7 (3.7)	-	6.15 (6.17)
M^{II}-(3aminobenzoates)				
[Ca(*m*ABA)$_2$(H_2O)$_2$]	48.4 (48.2)	4.6 (4.6)	-	8.05 (8.04)
[Ca(*m*ABA)$_2$], 200 °C	51.7 (53.8)	4.0 (3.8)	-	8.6 (8.9)
[{Sr(*m*ABA)$_2$(H_2O)$_2$}·H_2O]	41.4 (40.6)	4.3 (4.3)	-	6.9 (6.8)
[Sr(*m*ABA)$_2$], 200 °C	45.4 (46.7)	3.3 (3.3)	-	7.5 (7.9)
[{Ba(*m*ABA)$_2$(H_2O)$_2$} 2(H_2O)]	34.9 (34.9)	3.3 (3.3)	-	5.8 (5.8)
[Ba(*m*ABA)$_2$], 200 °C	40.0 (41.01)	2.9 (2.9)	-	6.6 (6.8)

A3. Ca-and Sr-(Tetrafluorobenzene-Dicarboxylates) (FCPs: 1-6)

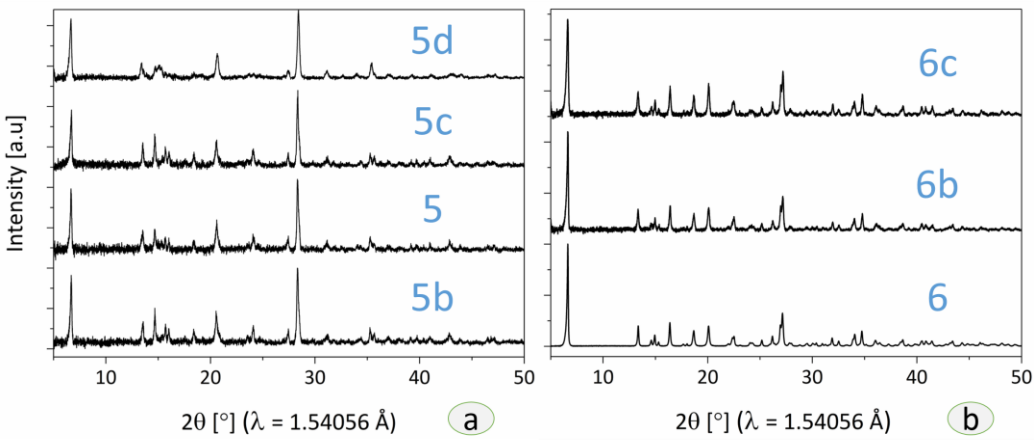

Figure A.3: PXRD patterns of Ca- and Sr-FCPs based on H_2*o*BDC-F_4. (a) [Ca(*o*BDC-F_4)(H_2O)$_2$] (**5**) obtained by milling H_2*o*BDC-F_4 with $Ca(OH)_2$ + 130 µl H_2O for 30 min (5b), 1h (5), 4h (5c), or by H_2*o*BDC-F_4 and $Ca(OH)_2$ for 4h in the absence of water (5d). (b) [Sr(*o*BDC-F_4)(H_2O)$_2$] (**6**) obtained by milling H_2*o*BDC-F_4 with $Sr(OH)_2 \cdot 8H_2O$ for 1h (6), $Sr(OH)_2$ + 130 µl H_2O for 1h (6b), or $Sr(OH)_2$ for 4h (6c). The molar ratio between organic and inorganic samples was maintained as 1:1.

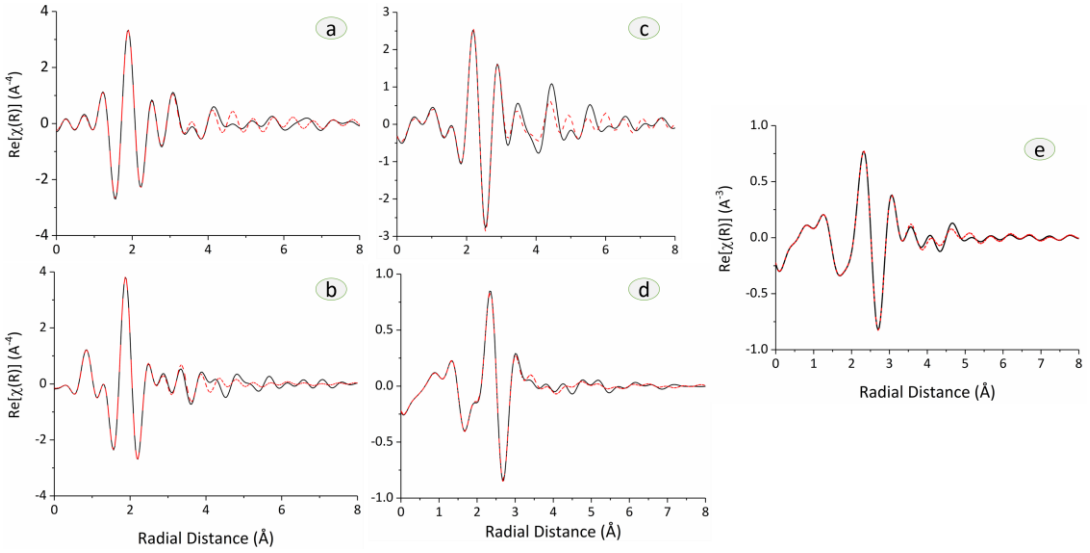

Figure A.4: EXAFS data shown in real space for Ca- and Sr-FCPs (**1**, **2**, **3**, **4**, **6**). The experimental data (black line) are presented along with the best fit model of the FT magnitude (red dotted line). (a) Ca *K*-edge EXAFS spectrum for **1** (R = 0.03). (b) Sr *K*-edge EXAFS spectrum for **2** (R = 0.03). (c) Ca *K*-edge EXAFS spectrum for **3** (R = 0.005). (d) Sr *K*-edge EXAFS spectrum for **4** (R = 0.0008). (e) Sr *K*-edge EXAFS spectrum for **6** (R = 0.007).

Table A.3: crystal lattice parameters and refinement data for [Ca(*o*BDC-F_4)(H_2O)$_2$] (**5**) compared to [Sr(*O*bdc-F_4)(H_2O)$_2$] (**6**).

Lattice parameters	[Ca(*o*BDC-F_4)·2H_2O] (**5**)	[Sr(*o*BDC-F_4)·2H_2O] (**6**)
Crystal system	Monoclinic	Monoclinic
Space group	P 1 2_1 /c 1 (14)	P 1 2_1 /c 1 (14)
Cell volume (Å^3)	1056.9(6)	1089.58(12)
a (Å)	8.008(3)	8.101(5)
b (Å)	26.410(8)	26.399(12)
c (Å)	6.9712(15)	6.989(4)
β (°)	134.209(15)	133.198(1)
λ (Å)	1.54056 (Cu-$K_{\alpha1}$)	1.54056 (Cu-$K_{\alpha1}$)
R_{wp}	3.96	2.99
R_p	2.68	2.08
R_{Bragg}	2.522	1.558
GOF	4.43	3.64

Table A.4: EXAFS fit parameters for the compound **1** (The root mean square error (RMSE) is 0.0156) and **2** (RMSE is 0.0002).

	[Ca(*p*BDC-F_4)(H_2O)$_4$] (**1**)			[Sr(*p*BDC-F_4)(H_2O)$_4$] (**2**)		
Scattering path	R_{model} (Å)	R_{fit} (Å)	R_{diff}^2 (Å)	R_{model} (Å)	R_{fit} (Å)	R_{diff}^2 (Å)
M—O1	2.60	2.46	0.0196	2.62	2.60	0.0004
M—O1’	2.60	2.46	0.0196	2.62	2.60	0.0004
M—O3	2.39	2.27	0.0144	2.41	2.40	0.0001
M—O4	2.57	2.46	0.0121	2.65	2.63	0.0004
M—O4’	2.57	2.46	0.0121	2.65	2.63	0.0004
M—O4’’	2.65	2.53	0.0144	2.73	2.72	0.0001
M—O4’’’	2.65	2.53	0.0144	2.73	2.72	0.0001
M—O5	2.46	2.33	0.0169	2.54	2.53	0.0001
M—O5’	2.52	2.40	0.0144	2.61	2.60	0.0001
Average (Å)	2.56	2.43		2.592	2.60	
RMSE			0.0156			0.0002
R-Factor		0.03			0.03	
Reduced chi-square (X^2)		328.258			5202.83	

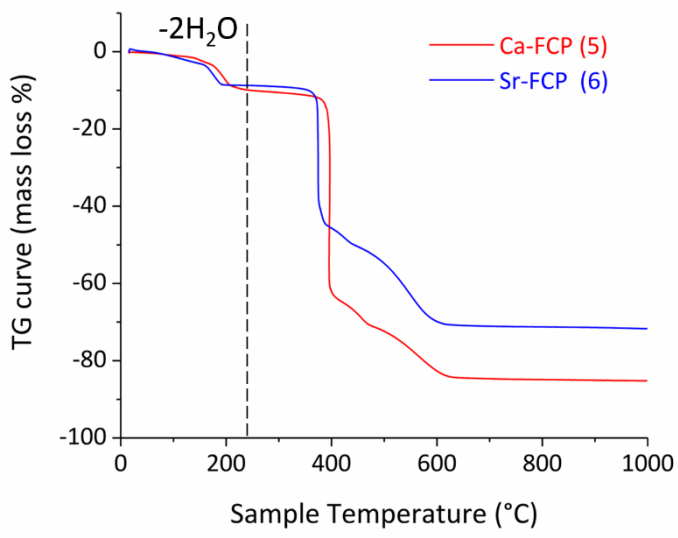

Figure A.5: TG Curves for samples of [Ca(*o*BDC-F_4)(H_2O)$_2$] (**5**) (red curve) and [Sr(*o*BDC-F_4)(H_2O)$_2$] (**6**) (blue curve).

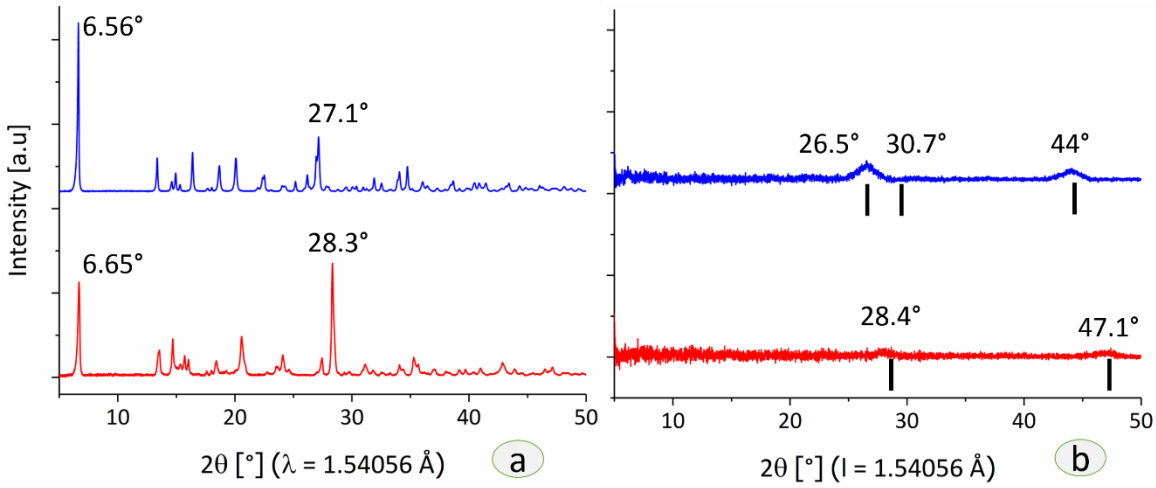

Figure A.6: PXRD patterns of [Ca(*o*BDC-F_4)(H_2O)$_2$] (**5**) (red PXRD pattern) and [Sr(*o*BDC-F_4)(H_2O)$_2$] (**6**) (blue PXRD pattern). (a) Samples as-synthesized. (b) Samples after decompositions compared to the standard X-ray lines for CaF_2 from the 00-075-0097 card and SrF_2 from the 00-001-0644 card (black vertical lines).

A4. Ca- and Sr-(Benzene-Dicarboxylates) (CPs: 7-11)

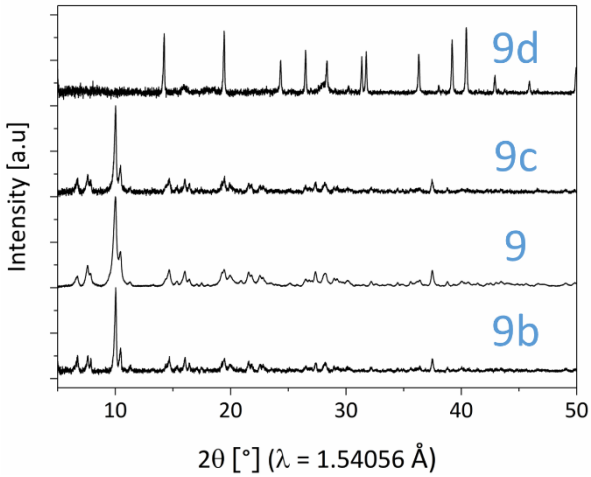

Figure A.7: PXRD patterns of [Sr(*m*BDC)(H_2O)$_{3.4}$] (**9**). The compound was obtained by milling H_2*m*BDC and $Sr(OH)_2 \cdot 8H_2O$ for 15 min (9b), for 1h (9), for 4h (9c). The milling of $Sr(OH)_2$ + 130 µl H_2O for 15 min or 1h led to the formation of a different product (9d). The molar ratio between organic and inorganic samples was 1:1.

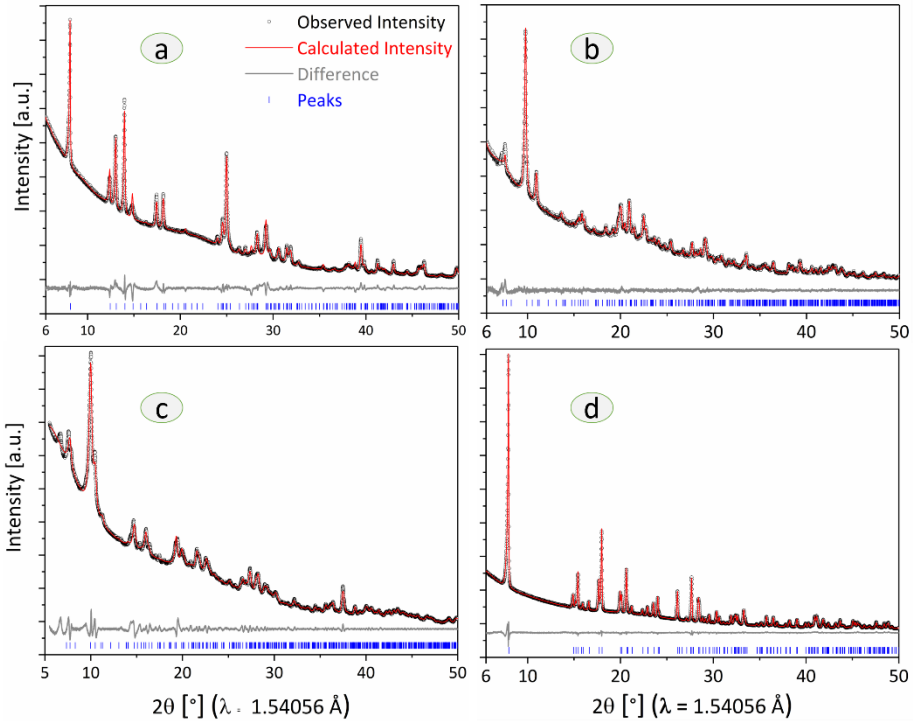

Figure A.8: Rietveld refinements for the crystal structures of Ca-CPs **7** (a), **8** (b), and **10** (c). The LeBail refinement for the PXRD data of Sr-CP **9** (c).

Table A.5: Crystal lattice parameters and refinement data for [Ca(*m*BDC)(H_2O)$_{3.4}$] (**8**) compared to [Sr(*m*BDC)(H_2O)$_{3.4}$] (**9**).

Lattice parameters	[Ca(*m*BDC)(H_2O)$_{3.4}$] (**8**)	[Sr(*m*BDC)(H_2O)$_{3.4}$] (**9**)
Crystal system	Monoclinic	Monoclinic
Space group	C 1 2/c 1 (15)	C 1 2/c 1 (15)
Cell volume (Å^3)	5334.1(5)	5316(5)
a (Å)	15.5899(7)	15.668(8)
b (Å)	21.4477(12)	21.256(14)
c (Å)	17.1872(8)	17.191(7)
β (°)	111.848(3)	111.81(3)
λ (Å)	1.54056 (Cu-K$_{\alpha1}$)	1.54056 (Cu-K$_{\alpha1}$)
R_{wp}	2.13	2.33
R_p	1.60	1.66
R_{Bragg}	0.571	0.081
GOF	1.25	3.92

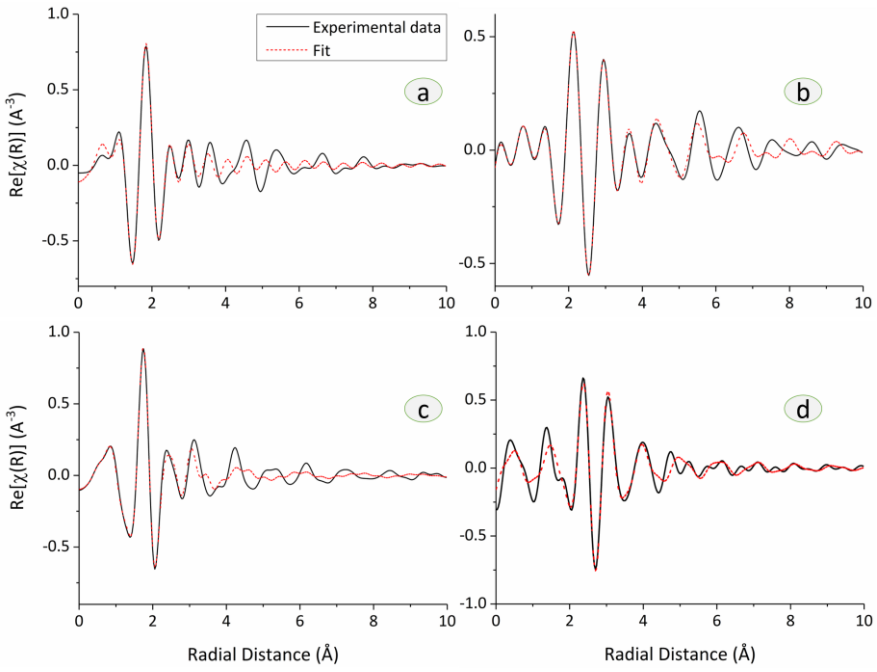

Figure A.9: Ca *K*-edge EXAFS spectra shown in real space. (a) [Ca(*p*BDC)(H_2O)$_3$] (**7**). (b) [Ca(*m*BDC)(H_2O)$_{3.4}$] (**8**). (c) [Ca(*o*BDC)(H_2O)] (**10**).

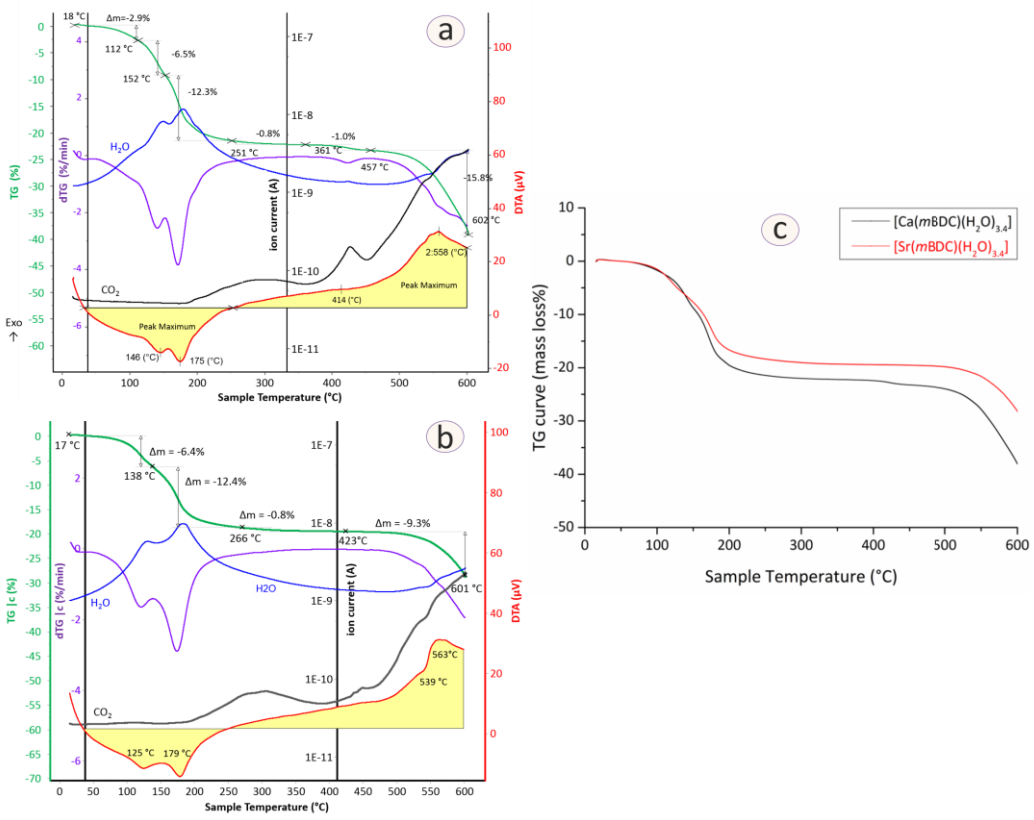

Figure A.10: Thermoanalytical curves of (a) [Ca(*m*BDC)(H_2O)$_{3.4}$] (**8**) and (b) [Sr(*m*BDC)(H_2O)$_{3.4}$] (**9**). (c) TG Curves for **8** (black curve) and **9** (red curve).

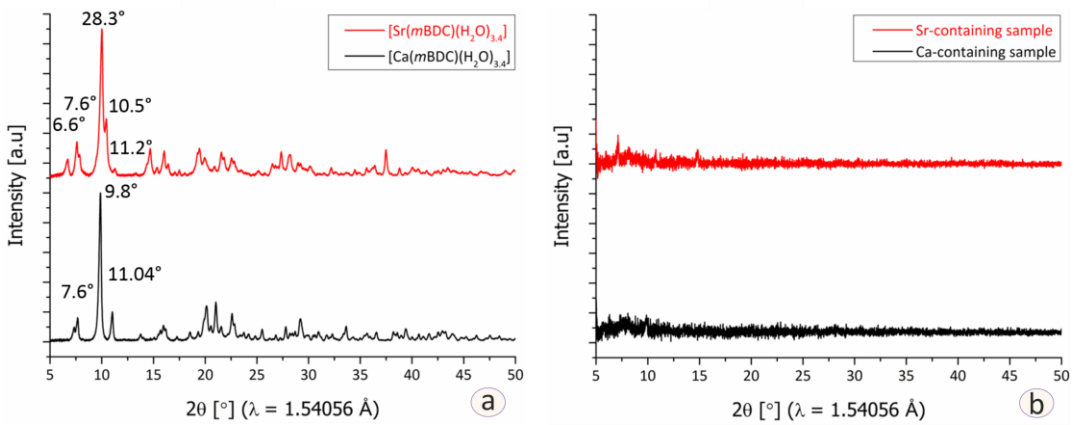

Figure A.11: PXRD patterns of [Ca(*m*BDC)(H_2O)$_{3.4}$] (**8**) (red) and [Sr(*m*BDC)(H_2O)$_{3.4}$] (**9**) (black). (a) Samples as-synthesized. (b) Samples after thermal post-treatments.

A5. Ba-Fluorinated and Fluorine-Free CPs (FCPs and CPs: 12-16)

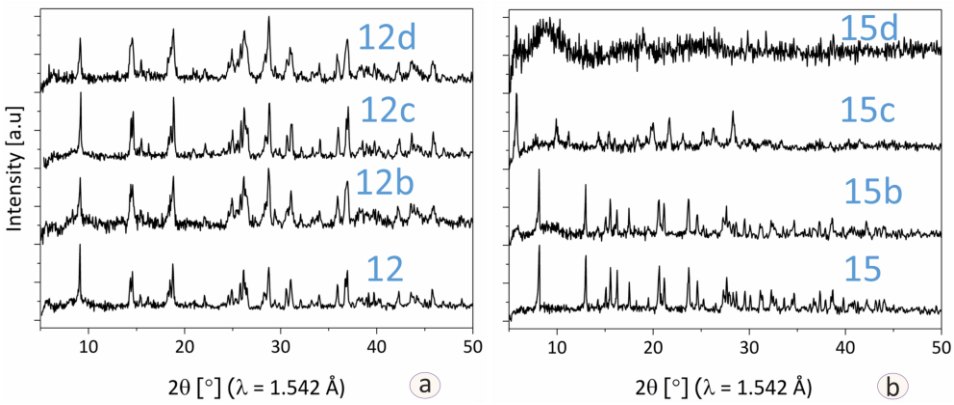

Figure A.12: PXRD patterns of compounds **12** and **15**. (a) [Ba(*p*BDC-F_4)(H_2O)$_{0.5}$] (**12**) obtained by milling H_2*p*BDC-F_4 with $Ba(OH)_2{\cdot}8H_2O$ for 1h (12), $Ba(OH)_2{\cdot}1H_2O$ for 4h (12b), $Ba(OH)_2$ + 130 µl H_2O (12c) for 1h, or $Ba(OH)_2$ for 1h (12d). (b) [Ba(*m*BDC)(H_2O)$_{2.5}$] (**15**) obtained by milling H_2*m*BDC with $Ba(OH)_2{\cdot}8H_2O$ for 1h (PXRD pattern 15) or 2h (15b). A different product was obtained by milling H_2*m*BDC and $Ba(OH)_2$ + 130 µl H_2O for 1h (15c). An inferior crystalline product was formed by milling H_2*m*BDC and $Ba(OH)_2$ in the absence of water (15d). The molar ratio between organic and inorganic samples was maintained as 1:1.

A6. Ca-, Sr-, and Ba-Anthranilates (CPs: 17-19)

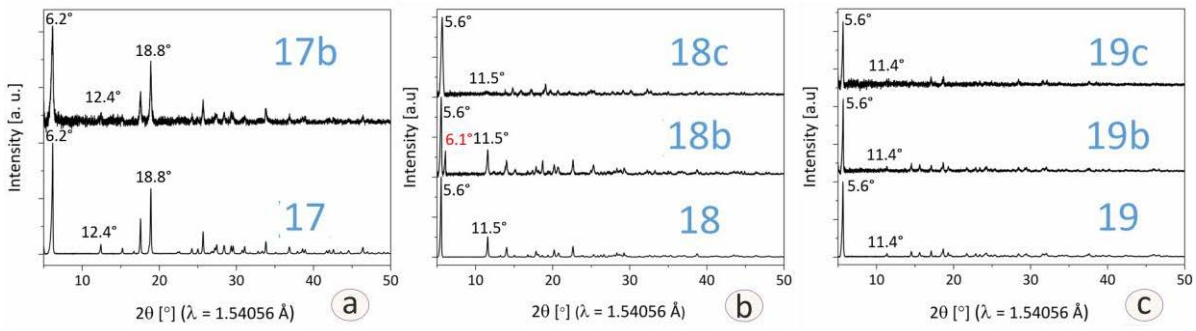

Figure A.13: PXRD patterns of compounds **17**, **18**, and **19**. (a) [Ca(*o*ABA)(H_2O)$_3$] (**17**) obtained by milling *o*ABAH with $Ca(OH)_2$ + 130 µl H_2O for 1h (17) or 4h in the absence of water (17b). (**b**) [{Sr(*o*ABA)$_2$(H_2O)$_2$}·H_2O] (**18**) obtained by milling *o*ABAH with $Sr(OH)_2{\cdot}8H_2O$ for 1h (18), $Sr(OH)_2$ + 130 µl H_2O for 1h (18b), or $Sr(OH)_2$ for 4h (18c). (**c**) [Ba(*o*ABAH)$_2$(H_2O)$_{0.5}$] (**19**) obtained by milling *o*ABAH with $Ba(OH)_2{\cdot}8H_2O$ for 1h (19), $Ba(OH)_2$ + 130 µl H_2O for 1h (19b), or $Ba(OH)_2$ for 1h (19c). The molar ratio between organic and inorganic samples was maintained as 1:2, respectively.

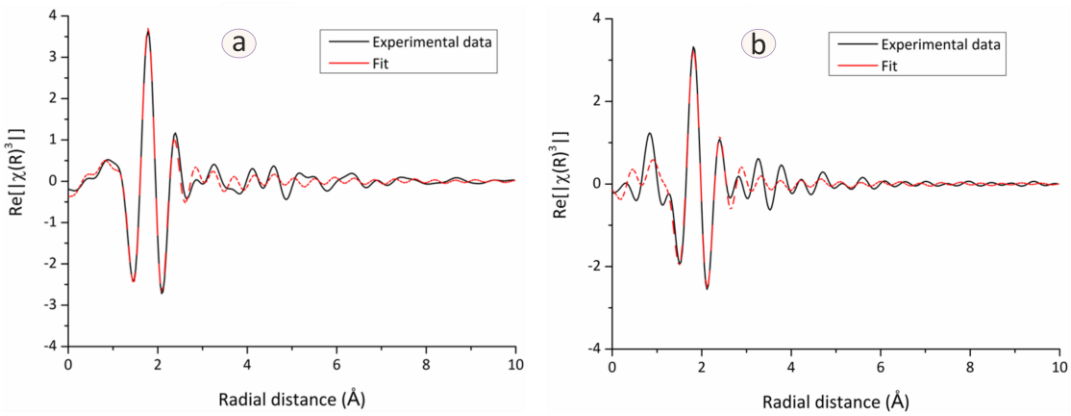

Figure A.14: Ca *K*-edge EXAFS spectrum shown in real space for compounds **17** (a) and Sr- *K*-edge EXAFS spectrum shown in real space for **18** (b). The experimental data (black line) are presented along with the best fit model of the FT magnitude (red dotted line).

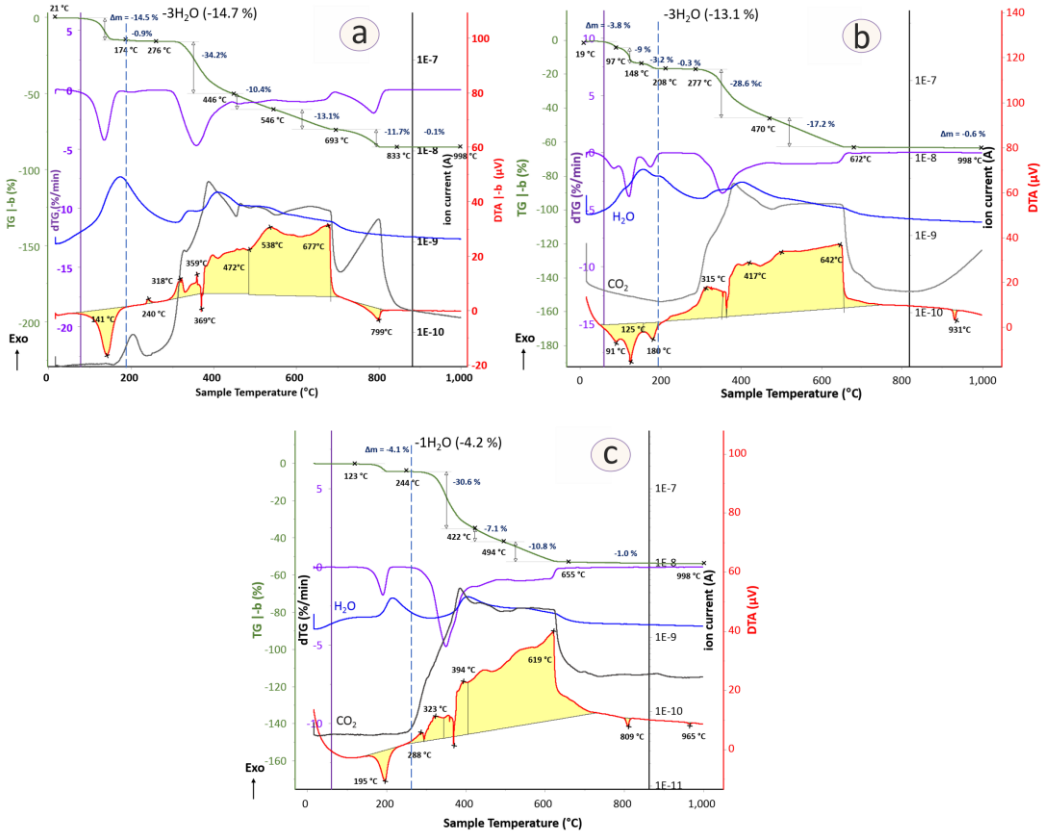

Figure A.15: Thermoanalytical curves of (a) [Ca(*o*ABA)$(H_2O)_3$] (**17**), (**b**) [{Sr(*o*ABA)$_2(H_2O)_2$}·H_2O] (**18**), and (**c**) [Ba(*o*ABAH)$_2(H_2O)_{0.5}$] (**19**).

Acknowledgments

I would like to acknowledge the valuable assistance I have received throughout my doctoral research from all people at the Graduate School of Analytical Sciences Adlershof (SALSA), Humboldt University Berlin (HUB) and Federal Institute for Materials Research and Testing (BAM).

First, I want to express my sincere gratitude to Prof. Erhard Kemnitz, Dr. Franziska Emmerling, and Dr. Gudrun Scholz for their academic supervision, resourceful guidance, and patience throughout my doctoral studies. Their continued support and invaluable expertise have enabled the completion of my thesis and all other exciting findings. I am thankful to Prof. Wolfgang Tremel for his willingness to be the external reviewer of my thesis.

My thanks and appreciation to the colleagues at BAM and HUB for their technical support, and the measurements have been done; Dr. Ana Guilherme Buzanich (EXAFS at BESSY II Berlin), Dr. Stefan Reinsch (DTA-TG), Mrs. Annett Zimathies (gas sorption), Mr. Carsten Prinz (DVS), Mrs. Sigrid Benemann (SEM imaging), Mrs. Anka Kohl (ATR-IR), Dr. Andrea Zehl and Mrs. Jenny Odoj (elemental analysis), Mrs. Sigrid Bäßler (fluorine analysis), Dr. Matthias Karg and Dominik Lubjuhn (PXRD), and Dr. Giannantonio Cibin (B18 Core XAS, Diamond, Oxford).

I am grateful for the funding was received from the Excellence Initiative of the German Research Foundation (DFG project: GSC 1013) and SALSA, in addition to the financial support by BAM and Dr. Emmerling.

My gratitude is extended to my friends and colleagues at Kemnitz research group, Division 1.3 at BAM, and SALSA. Special thanks to Mrs. Katharina Schultens, Manuel Wilke, Anke Kabelitz, and Stefan Mahn.

My thanks are also to the researchers, whom I have cited, the writers of the books I have read and provided me with a third perspective in seeing the beautiful diversity of humanity. ويلٌ لطالبِ العلمِ إن رضي عن نفسه *translation:* Seekers of knowledge are never satisfied. Otherwise, it becomes the end of their voyage.*

Last but not least, my sincerest gratitude is to my family; My Mother, Father, Sisters, and my beloved wife, Manar, for their endless support and unconditional love. This thesis is dedicated to my sister Shaima' -may her beautiful soul rest in peace.

**Thoughtful words of Dr. Taha Hussein (1889-1973). Translation credit: Dr. Ahmed Zewail (1946-2016).*

List of Publications

(1) A. Al-Terkawi, G. Scholz, F. Emmerling, E. Kemnitz. Mechanochemical Synthesis, Characterization, and Structure Determination of New Alkaline Earth Metal-Tetrafluoroterephthalate Frameworks: Ca(*p*BDC-F_4)·4H_2O, Sr(*p*BDC-F_4)·4H_2O, and Ba(*p*BDC-F_4). *Cryst. Growth Des.* **2016**, *16*, 1923–1933. (DOI: 10.1021/acs.cgd.5b01457).

(2) A. Al-Terkawi, G. Scholz, A. G. Buzanich, S. Reinsch, F. Emmerling, E. Kemnitz. Ca- and Sr-Tetrafluoroisophthalates: Mechanochemical Synthesis, Characterization, and *ab initio* Structure Determination. *Dalton Trans.* **2017**, *46*, 6003–6012. (DOI: 10.1039/C7DT00734E).

(3) A. Al-Terkawi, G. Scholz, Emmerling, E. Kemnitz. Strontium-Coordination Polymers based on Tetrafluorophthalic and Phthalic acids: Mechanochemical Synthesis, *ab initio* Structures Determination, and Spectroscopic Characterization. *Dalton Trans.* **2017**, *46*, 12574–12587. (DOI: 10.1039/C7DT02564E),

(4) A. Al-Terkawi, G. Scholz, C. Prinz, A. Zimathies, F. Emmerling, E. Kemnitz. Hydrated and Dehydrated Ca-Coordination Polymers based on Benzene-Dicarboxylates: Mechanochemical Synthesis, Structures Refinement, and Spectroscopic Characterization. *CrystEngComm*. **2018**, *20*, 946-961. (DOI: 10.1039/C7CE01906H).

(5) A. Al-Terkawi, G. Scholz, F. Emmerling, E. Kemnitz. Barium Coordination Polymers based on Fluorinated and Fluorine-free Benzene-Dicarboxylates: Mechanochemical Synthesis and Spectroscopic Characterization. *Solid State Sci.* **2018**, *79*, 99-108. (DOI: 10.1016/j.solidstatesciences.2018.03.013).

(6) A. Al-Terkawi, G. Scholz, F. Emmerling, E. Kemnitz. Ca-Tetrafluorophthalate and Sr-Isophthalate: Mechanochemical Synthesis and Characterization in Comparison with other Ca-and Sr-Coordination Polymers. *Dalton Trans.,* **2018**. (DOI: 10.1039/C8DT00488A).

(7) A. Al-Terkawi, G. Scholz, C. Prinz, F. Emmerling, E. Kemnitz. Ca-, Sr-, and Ba-Coordination Polymers based on Anthranilic acid via Mechanochemistry. (*In preparation*).

Curriculum Vitae

Für die elektronische Publikation entfernt.

Selbstständigkeitserklärung

Ich erkläre, dass ich die Dissertation selbstständig und nur unter Verwendung der von mir gemäß § 7 Abs. 3 der Promotionsordnung der Mathematisch-Naturwissenschaftlichen Fakultät, veröffentlicht im Amtlichen Mittelungsblatt der Humboldt-Universität zu Berlin Nr. 126/2014 am 18.11.2014 angegebenen Hilfsmittel angefertigt habe.

Abdal-Azim Al-Terkawi

Berlin, den /04/2018